UNIVERSITY OF TRENTO

Doctoral School in Civil, Environmental and Mechanical Engineering

Curriculum 1. Civil and Environmental Engineering

Ilaria Cunico

Nonlinear dynamics of River biogeomorphic feedbacks

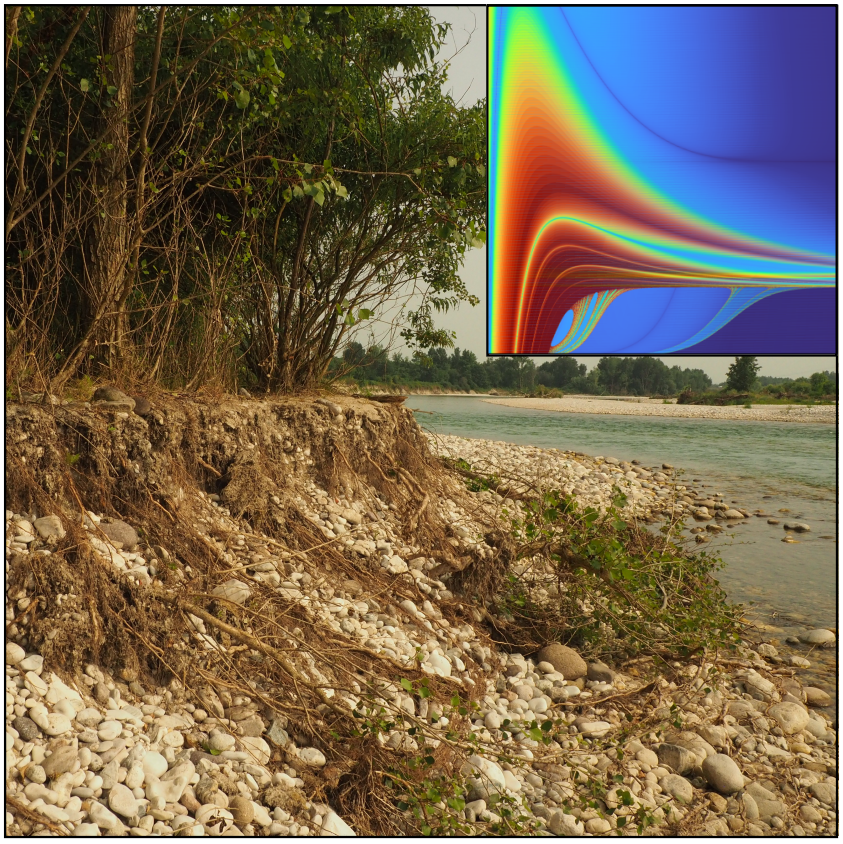

2024 - Doctoral thesis

UNIVERSITY OF TRENTO - Italy
Department of Civil, Environmental
and Mechanical Engineering

Doctoral School in Civil, Environmental and Mechanical Engineering
Topic 1. Civil and Environmental Engineering - XXXVI cycle 2020/2024

Doctoral Thesis - February 2024

Ilaria Cunico

Nonlinear dynamics of River biogeomorphic feedbacks

Supervisors
Annunziato Siviglia, University of Trento
Walter Bertoldi, University of Trento

University of Trento
Doctoral School in Civil, Environmental and Mechanical Engineering
http://web.unitn.it/en/dricam
Via Mesiano 77, I-38123 Trento
Tel. +39 0461 282670 / 2611 - *dicamphd@unitn.it*

“We would all be better off if more people realised that simple nonlinear systems do not necessarily possess simple dynamical properties.”

–Robert May, 1976-

”I think the next [21st] century will be the century of complexity. We have already discovered the basic laws that govern matter and understand all the normal situations. We don’t know how the laws fit together, and what happens under extreme conditions. But I expect we will find a complete unified theory sometime this century. There is no limit to the complexity that we can build using those basic laws.”

-Stephen Hawking, 2000-

”Bisogna avere un caos dentro di sé per generare una stella danzante.”

-Nietzsche, 1883–

Abstract

Rivers are amongst the most dynamic ecosystems on earth. River ecosystems are highly disturbed environments, where riparian vegetation, water and sediments, are interconnected by positive and negative feedbacks, driven by a set of interactions. In the last two decades, it has been widely recognized that these eco-morphodynamic feedbacks play a crucial role in governing the equilibrium and dynamics of river ecosystem.
However, the incomplete understanding and quantification of these feedbacks limit the comprehension of river behavior and the development of efficient predictive models.
Thus, in this research, fundamental intrinsic feedbacks between riparian vegetation and hydro-morphodynamic disturbance are modeled, where the disturbance is generated by the vegetation itself. The aim is to investigate how these intrinsic feedbacks govern the equilibrium and dynamics of a simplified river ecosystem.
To this end, numerical simulations were conducted using both a 0D model (non-spatial) and a 1D model (spatial) coupling hydro-morphodynamics with vegetation dynamics. The case study is a straight channel where vegetation can grow only in the central patch, while upstream and downstream there are bare soil regions. The system is perturbed periodically by a succession of floods of constant amplitude. Vegetation growth occurs in between of two consecutive floods, during low flood periods. Vegetation consists of two components, the above-ground biomass (canopy) and below-ground biomass (root depth). In both models, the canopy increases the roughness, reducing flow velocity. Variations in the flow field and the reduction of bottom shear stress modify sediment transport, leading to a greater imbalance between the vegetated and bare areas and thus, inducing erosion. Erosion increases the probability of vegetation uprooting, and when scour reaches root depth, uprooting occurs. The overall feedback loop is negative: higher vegetation biomass causes greater sediment flux imbalance and more erosion, ultimately resulting in less vegetation. However, root growth may inhibit the negative feedback loop, promoting positive feedbacks. Indeed, this interplay between hydro-morphodynamic disturbance (erosion) and the vegetation resistance (root depth), governs the predominance of either a positive or a negative feedback overall balance.
Model results demonstrate that when the positive feedback overall balance prevails, the system always reaches a stable configuration. Furthermore, the system can exhibit hysteresis, meaning that, depending on the initial condition, it can achieve a stable configuration in two alternative states, the fully vegetated condition or bare soil. In the presence of the vegetated patch, the system can also exhibit a more complex multi-stable behavior, with infinite equilibria between the two alternative states. This also implies that spatial interactions smooth out critical transitions and tipping points, by facilitating smoother shifts that occur gradually through multiple smaller intermediate steps. Indeed, the resilience

of the system, which is the ability of the system to still maintain its fundamental structure and functions after being subject to the ecological disturbance, increases due to spatial interactions.
In contrast, when the negative feedback overall balance prevails, the system never reaches a steady state but exhibits dynamic oscillations. The oscillations can be either (i) periodic or (ii) aperiodic, strongly dependent on initial conditions, and with a positive Maximum Lyapunov Exponent, indicating chaotic behavior. The study also reveals that the route to chaos is a period-doubling bifurcation, and the calculation of time scale of predictability shows that the system is predictable only for a few growth-flood cycles.
These results suggest that altering the ratio between hydro-morphodynamic disturbance and vegetation resistance, such as through anthropogenic pressure and climate change, may shift the system from a positive to a negative feedback overall balance. This shift could lead from a stable state to periodic oscillations or unpredictable chaotic behavior, limiting long-term predictions of river trajectories. Additionally, understanding how positive and negative eco-morphodynamic feedbacks govern river dynamics can contribute to develop efficient predictive models. Models are essential tools for implementing efficient river management and facilitate effective communication with stakeholders.

Acknowledgements

In primo luogo, ringrazio i miei supervisor, Nunzio e Walter. Durante la vostra supervisione costante e puntuale di questi tre anni ho avuto modo di affinare il mio pensiero critico, grazie al confronto incessante e la condivisione di idee e punti di vista spesso diversi. Il dubitare incessante di ogni verità e certezza è estenuante ma credo, alla fine, l'unico vero metodo per fare buona ricerca.
Il confronto con il vostro sapere e la vostra esperienza è stato fondamentale per tenere il filo anche nei periodi di perdizione e per confermare la strada giusta quando era giusta. Essenziale è stato anche il vostro aiuto attivo nella ricerca, nel risolvere problemi e nello sviluppare i metodi usati per le analisi.
Come ho imparato, 3 è il numero minimo per osservare dinamiche caotiche e credo che noi 3 siamo stati un buon esempio di sistema complesso in zona caotica, con alta energia, dinamicità e output a volte imprevedibili.

Ringrazio poi Francesco, il tuo lavoro è stato un trampolino di lancio fondamentale per tutta la mia ricerca. Grazie per avermi sempre aiutata e incoraggiata, condividendomi apertamente saperi e opinioni intelligenti sulle quali riflettere.

Ringrazio anche i miei compagni (amici!) di viaggio, Chiara, Erica, Pascal, Gaetano, Marco, Angelica, Mattia, Nicola. Grazie per avere condiviso con me questo percorso, tutte le sue gioie e i suoi dolori. Senza le nostre pausette, i pranzi in terrazza, le camminate dei weekend (che in realtà io non ho mai fatto "perché ero sempre a Vicenza") questo percorso non sarebbe stato decisamente lo stesso.
Grazie per apprezzare l'ironia e per esserci stati anche nei momenti di grande sconforto, per esservi lamentati assieme e per avermi supportata nei piccoli successi. Siete delle belle persone e mi avete fatto crescere e divertire molto. Spero guariremo tutti dalla sindrome dell'impostore, perché ce lo meritiamo. Vi auguro un grande successo per il vostro percorso lavorativo, è stato bello farne un pezzo assieme! Grazie in particolare ad Angelica per avermi dato un tetto, a Erica per essere gentile, a Chiara per essere stata la nostra rappresentante, a Marco per il black humor, a Gaetano per essere un bravo bambino (e la pizza), a Mattia per le belle chiacchierate e a Pascal per essere stato compagno d'avventura e di discussioni (spesso, proficue!) sin dall'inizio.

Grazie anche a Samuele, Ale, Ju, Cele, Ada, Ali, Luciana per aver fatto (vostro malgrado) parte di questo mondo e per esservi sorbiti discorsi noiosissimi su barre fluviali, carrellini instabili, caos, nature based-solutions e progetti socio-agricoli. Grazie per le serate passate in compagnia e per averci riportati alla realtà della vita, ovvero fuori

dall'accademia. I weekend e le serate con voi ci hanno probabilmente salvati dalla follia. Grazie a Ju anche per il drama, i mille addi e per avermi dato la possibilità di sfoggiare il mio "portoghese brillante".

Grazie Erri e a Marta, soprattutto per esserci sempre stati nel momento del bisogno (come a Natale dell'anno covid, quando ero sola a Trento isolata dalla mia famiglia). Grazie Erri anche per aver condiviso con me la prima importante conferenza internazionale.
Grazie Livia, la tua onestà e positività sono una gioia per il mio cuore.
Grazie Susi per le chiacchierate fino alle 3 di mattina, ma soprattutto per essere un'amica special da una vita.
Grazie Azadeh, per avermi dimostrato che l'intelligenza e il sarcasmo uniscono due persone di culture anche molto diverse.
Grazie anche a tutti gli altri post-doc, dottorandi e professori che hanno condiviso con me qualche momento o pensiero. Siete persone interessanti e super competenti, vi auguro successo con le vostre ricerche e con il vostro percorso di vita. Grazie per aver condiviso con me opinioni, punti di vista, serate e bei momenti. È bello vedere come molte persone cercano di migliorare il mondo, all'infuori di sé e ricerchino profondamente la verità.

Grazie alle mie coinquiline di casa Lorengo, Giulia, Vic, Ali. Grazie per avermi fatto divertire nelle serate di reclusione quarantena e per i grandi spezzi e situazioni assurde. È stato bello (e assolutamente delirante) vivere con voi.

Grazie a tutta la mia numerosa famiglia, genitori, fratelli, cugini, nonni, zie e zii, siete da sempre una parte fondamentale della mia vita.
Grazie in particolare alla nostra capostipite, la nonna, a tutti i tuoi "pacchi del Nord", per aver sempre pensato a me e al fatto che potessi morire di fame tra le montagne. Hai ragione nonna, senza di te sarei morta di fame. Grazie soprattutto per essere così dannatamente sveglia e ironica. Sei da sempre il pilastro e il collante fondamentale della nostra famiglia.
Grazie ai miei cani, ho amato tornate da voi nel weekend, farmi coccolare quando tutto andava male, siete amore puro.

Grazie a tutti gli amici che ho collezionato durante le diverse esperienze di vita in giro per il mondo e alla rete fitta di amicizie di Vicenza. Mi ricaricate di energia positiva e siete l'altra parte fondamentale della mia famiglia. Tra voi c'è chi c'è da sempre, c'è chi è stato raccolto durante il cammino, in situazioni assurde o appena adesso. La cosa fondamentale e che vi accomuna è che una volta caduti dentro la rete difficilemente riuscite a tinarvene fuori. Sembra più una minaccia ma a parte gli scherzi, grazie per esserci, spero continuerete ad esserci per sempre. D'altronde sapete che non sarà facile liberarsi di me.

Grazie Michele, un battito d'ali di farfalla mi ha portato a quella festa tra fisici. Il tuo aiuto è stato fondamentale per capire come calcolare quel dannatissimo Maximum Lyapunov Exponent. Grazie per aver condiviso con me il tuo sapere e per avermi aiutata.

Grazie Henk, per aver partecipato attivamente ai meeting settimanali e per averci condiviso il tuo sapere e infine anche per avermi suggerito di andare ad Utrecht per la fase finale di questo percorso.
Grazie Max, per la tua onestà, gentilezza e capacità comunicativa. Grazie per avermi fatta

sentire immediatamente parte integrata del gruppo di ricerca ad Utrecht.

Grazie Costanza ed Andrea per avermi fatta sentire ”a casa” quando mi sono sentita sola e lontana in un paese straniero (ma soprattutto per le serate da vite al limite e di cazzeggio estremo).
Grazie Shri e Marianne per essere stati la mia famiglia ad Utrecht e per i discorsi contro il nazismo e il colonialismo da sbronzi.
Grazie Raquel, Marina e Claudia per aver portato un po' di spirito latino (e la tortilla) al Nord.
Grazie Annanta, per essere cosi smart but dumb. Perdonami se ti ho persa tra i canali di Utrecht, ma è stato tanto divertente.
Grazie Pablo per essere cosi uguale a me, a Francesca per avere la mia stessa struttura mentale (veneta) e a Giulia per l'onestà tagliente dutch. Grazie anche per le partite a calcetto durante le VERE pause pranzo al Copernicus.
Grazie Swarnendu, per tutti i discorsi profondi, per avermi avvicinata alla cultura indiana e per la tua apertura di pensiero.
Grazie a tutti gli altri colleghi e amici di Utrecht, sono stati dei bei mesi e mi avete dato molto umanamente e professionalmente.

Infine ringrazio la mia testardaggine, un difetto grave ma che a volte può portare anche a dei bei risultati.

Contents

Chapter 1

Introduction

1.1 River Ecosystem

Rivers are amongst the most dynamic and highly productive ecosystems on earth (**e.g., Van Oorschot et al., 2017**). In the past, they played a central role in human society, serving as the cradle and hub of some of the most important civilizations **(Smith, 2020)**. Even nowadays, they provide essential services to society and they support economic and recreational activities. They are highly disturbed environments, which are characterized by complex, temporally dynamic spatial distributions associated with a shifting mosaic of habitat patches **(Gurnell, 2014)**. In such environments, living organisms, such as riparian vegetation, interact with abiotic components of the surrounding environment, sediments, and water, through nonlinear complex feedbacks **(Odum, 1959)**.
Over the last two decades the importance has been widely recognized of these two-way interactions between riparian vegetation and hydro-morphodynamic processes in controlling river ecosystem equilibrium and dynamics **(Corenblit et al., 2007)**. The importance has been highlighted by laboratory experiments (**e.g., Tal and Paola, 2010; Le Bouteiller and Venditti, 2015**), field studies (**e.g., Pasquale et al., 2014**), and numerical models (**e.g., Perona et al., 2009; Bertagni et al., 2018**).
The main eco-morphodynamic feedbacks are illustrated in the Figure 1.1 and are briefly described in the following paragraphs.

1.1.1 Effects of riparian vegetation on hydro-morphodynamics

Riparian vegetation has been recognized as one of the fundamental components of river systems, controlling river evolution at different spatial and temporal scales **(Gurnell, 2014)**. The flow field encounters the canopy and undergoes a change in turbulence **(Nepf, 2012)**, direction and intensity due to an increase in drag force and roughness. These changes occur at both the scale of individual plants and vegetation patches **(Zong and Nepf, 2010)**. The additional drag force is due to the physical obstruction of the canopy and varies significantly with biomechanical properties, such as stem density, flexibility, submerged and emergent conditions **(Västilä and Järvelä, 2014)**. The increase in roughness is a consequence of energy and momentum loss caused by friction with vegetation and the ground. In hydraulic models, the overall feedback between canopy and flow is commonly

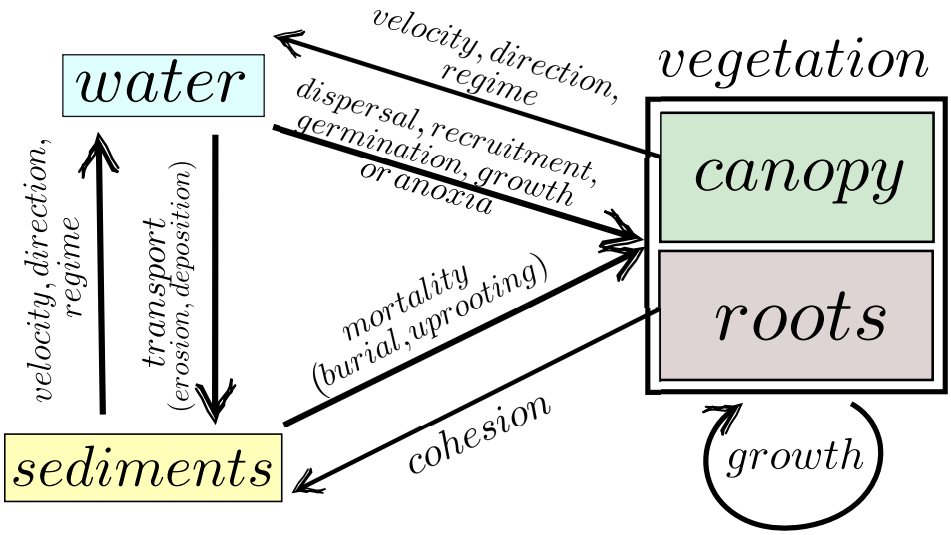

Figure 1.1: Key eco-morphodynamic feedbacks in the river ecosystem

modeled by increasing the roughness value **(Politti et al., 2018)**.
Variations in the flow field have also profound effects on sediment transport, indeed bottom shear stress is reduced due to the presence of vegetation. In fact, the vegetation slows down the flow velocity and increases local deposition, stabilizing channel geometry **(Li and Millar, 2011)**. Reduction in bottom shear stress within vegetated patches induces reach-scale riverbed changes, with a higher reduction observed in areas with denser vegetation and larger plant frontal areas **(Vargas-Luna et al., 2015; Le Bouteiller and Venditti, 2015)**. Ultimately, the canopy is also capable of trapping sediments **(Corenblit et al., 2014)**. The root system also plays a significant role in the morphodynamic evolution of river ecosystems. In fact, roots increase sediment cohesion **(Pasquale et al., 2014)** and affect the hydraulic and mechanical properties of the substrate, reducing erosion and increasing bank stability **(Gurnell, 2014; Politti et al., 2018)**. Additionally, they can alter the moisture content of the riverbed, as highlighted by **Tron et al.** (**2014**).
Roots often display a complex structure **(Gregory, 2007)** and can be phreatophytic, namely they extend into the riverbed to reach the groundwater level position. Among riparian plants, there are many examples of phreatophytic plants, such as *Quercus lobata* **(Rohde et al., 2021)** and *Populus nigra* **(Holloway et al., 2017)**, while this characteristic is less common in aquatic plants.

1.1.2 Effects of hydro-morphodynamics on riparian vegetation

Fluvial hydro-morphodynamic processes play a significant role in all plant life stages, that is, dispersal, colonization, recruitment, growth, succession and mortality **(Solari et al., 2016)**. Water flow is essential for the transportation and dispersal of seeds and propagules. After the dispersion, plant recruitment success depends mainly on water flow fluctuations **(Caponi et al., 2019)**, and on a minimum disturbance-free period (defined as "Windows of Opportunity" by **Balke and Nilsson 2019**). Additionally, groundwater level fluctu-

ations affect root system growth, distribution and maximum depth **(Tron et al., 2014)**. During vegetation succession, besides the flow and flood regime, other crucial elements include channel geometry, soil type, and species distribution and competition. To ensure their survival, riparian plants often adopt strategies during different life stages, such as developing high dispersal rates, vegetative reproduction **(Camporeale et al., 2013)** and resistant roots.
Prolonged periods of flooding can reduce the oxygen in the riverbed, causing plant mortality by anoxia. Moreover, hydro-morphodynamic processes can expose vegetation to mortality by burial and uprooting. Burial occurs during the final phase of floods, when water velocity decreases and sediments are deposited, covering totally (or even partially) the canopy **(Holloway et al., 2017)**. In contrast, uprooting occurs during floods when hydro-morphodynamic disturbance weaken the roots mechanical anchoring.
Edmaier et al. (**2011**) classified the uprooting into two types: the type I mechanism occurs when the flow has enough force to pull out the plant instantaneously; the second type II mechanism occurs when a gradual erosion exposes roots to the flow, reducing the plant's roots anchoring force. Thus, uprooting type II occurs only when a significant proportion of roots has been exposed due to erosion. Several studies suggest that the type II mechanism is the main cause of vegetation mortality in gravel bed rivers **(Pasquale et al., 2012; Crouzy et al., 2013; Edmaier et al., 2015; Bywater-Reyes et al., 2015)**.

1.1.3 Biogeomorphic succession: disturbance and resistance

Riparian vegetation can significantly control geomorphic processes and landform dynamics. Therefore, plants are "ecosystem engineers", and they use available resources to maintain, to modify or create their own habitat **(Jones et al., 1994)**. River size and stream power determine the species acting as ecosystem engineers. In low dynamic streams, aquatic plants prevail, while in larger rivers, pioneer riparian trees dominate because they must withstand higher stream power **(Gurnell, 2014)**. Plants play an active role and promote positive feedbacks, such as resisting against the flow, trapping and stabilizing sediments, and increasing bank stability **(Gurnell, 2014)**, to adapt the environment and create a niche favorable for biogeomorphic succession.
The biogeomorphic succession of vegetation is a self-organized, space- and time-oriented process. Indeed, it involves a gradual transition from bare soil to seedlings, then to pioneer shrublands, followed by post-pioneer forests or a biomorphological phase, ultimately reaching a stable state, the ecological phase, as shown in Figure 1.2 **(Corenblit et al., 2009)**. The biogeomorphic succession can regress due to the destructive flood force, which erodes sediments and uproots vegetation. Large floods, having low frequency and high intensity, may shift the system from any stage to bare soil. Therefore, the interplay between vegetation resistance force and the destructive flood force governs the spatial and temporal progression (landform aggradation) or regression (erosion and uprooting) in the biogeomorphic succession, generating cyclic dynamics.
Riparian trees can rapidly grow into mature plants within a few years under favorable hydro-morphological conditions **(Corenblit et al., 2014)**. Also root resistance develops quickly, with phreatophytic plant roots easily reaching depths greater than $> 1\ m$ within 1-2 years **(Mahoney and Rood, 1998)**. In larger gravel-bed rivers, the return interval of floods that can significantly affect vegetation has been reported to vary from 1-2 years

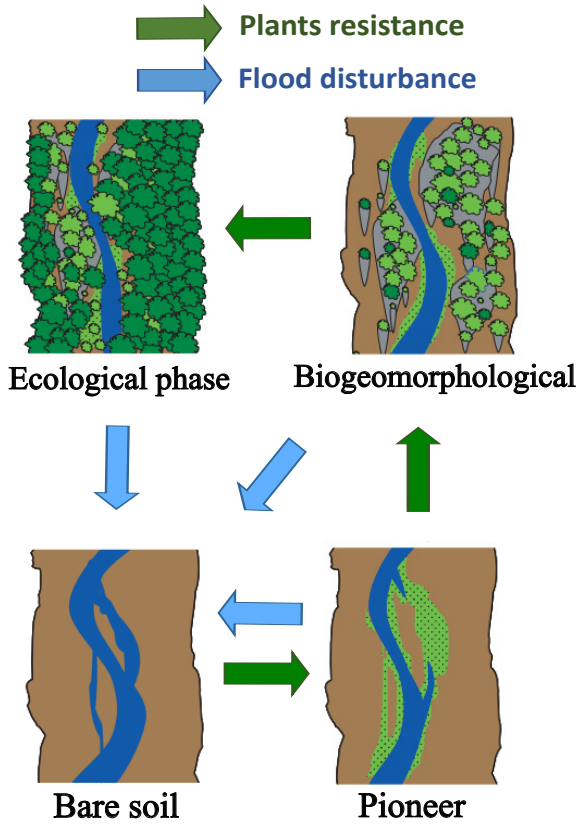

Figure 1.2: The interplay between the two antagonistic forces of vegetation resistance (green arrow) and flood disturbance (blue arrow) creates dynamic cycles in the biogeomorphic succession. Adapted from Corenblit et al., (2009).

for partial vegetation removal on highly dynamic braided rivers **(Surian et al., 2015)**, to several decades for major vegetation renewal **(Belletti et al., 2014)**.

1.2 River ecosystem as a complex system

From a mathematical perspective ecosystems, and thus also the river ecosystem, are complex systems **(Limburg et al., 2002)**. Complex systems consist of interconnected and interdependent elements that exhibit particular properties, including emergence, self-organization, and adaptation (as explained in the next paragraphs).
This perspective allows for understanding and predicting nonlinear phenomena, such as hysteresis cycles and abrupt shifts, which have been observed in river ecosystems, yet lacking a systematic interpretation. In fact, complex systems can be studied through the discipline of system dynamics, which explains complex behaviors such as hysteresis, but also oscillations, and chaos.

1.2.1 Positive and negative feedbacks loop

The ecosystem is, by definition, a physical system composed of biotic and abiotic elements interconnected by each other and the surrounding environment **(Odum, 1959)**. These interactions can be schematized by negative or positive feedbacks **(DeAngelis et al., 2012)**. Positive feedback amplifies the effect by reinforcing the other element in the same direction while negative feedback occurs when one element influences the other in the opposite direction. The ecosystem is typically composed of numerous interconnected elements in a network generating positive or negative feedback "loops" among all its components. Depending on the environmental condition and external disturbance, negative or positive feedback loops may prevail.
Positive feedback loops push the ecosystem in one direction, in an exponential growth or decay, towards the alternative stable states outside the normal operating parameters. Positive feedbacks stimulate changes and they are responsible of a rapid change within the ecosystem or shifts towards alternative stable states. An example of a positive feedback loop is the root-riverbed cohesion relation (see Figure 1.3A): roots increase riverbed cohesion (+), reducing sediment mobility and erosion, and enhancing soil strengthening, which in turn induces sediment accretion and root development (+) **(Van de Vijsel et al., 2023)**. Multiplying the positive effects results in a positive total loop that pushes the system toward landform aggradation and vegetated islands **(Corenblit et al., 2014)**.

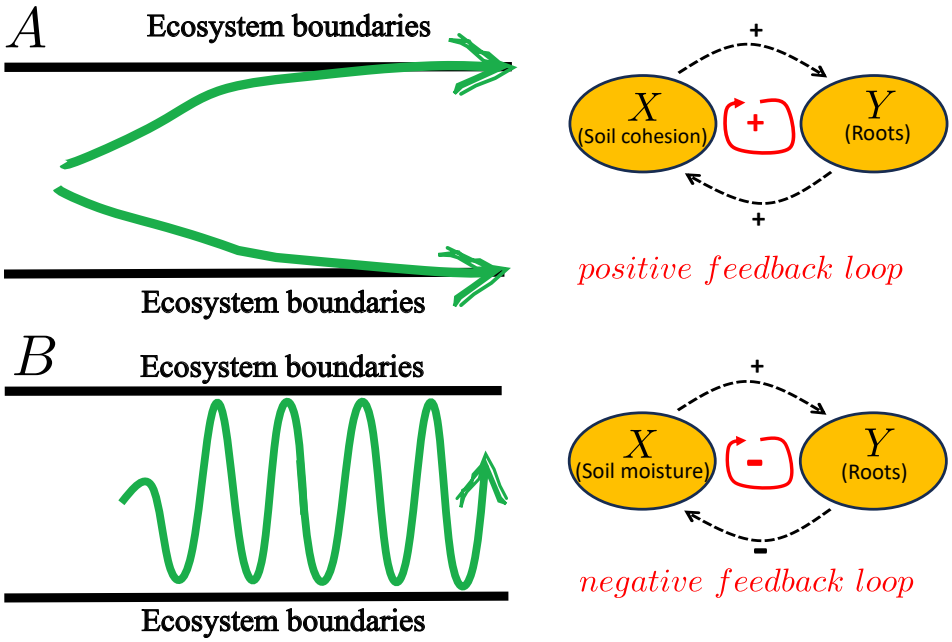

Figure 1.3: The nonlinear interactions among abiotic and biotic elements of an ecosystem can generate to either positive or negative feedback loops. (A) Positive feedback loops drive the ecosystem towards exponential growth or decay, pushing it towards alternative stable states —such as the roots-soil cohesion relation. (B) Conversely, negative feedback loops regulate the ecosystem's internal balance — such as the roots-soil moisture relation.

Instead, negative feedback loops regulate the entire ecosystem, keeping it within natural boundaries and regulating its internal balance. Several studies demonstrate how the internal balance can be both static and dynamic, meaning that some systems, to function properly, do not reach a steady state but keep on oscillating within the natural boundaries **(Siteur et al., 2016; Lloyd et al., 2001; Ruoff and Nishiyama, 2020)**. Negative feedback loops generate oscillations, which can be periodic or chaotic. For instance, a negative feedback loop is observed in the roots-riverbed moisture relation (see Figure 1.3B): riverbed moisture promotes root development (+), roots absorb water, reducing riverbed moisture (-). Multiplying the negative effect by the positive effect results in a negative total loop. In this way, both roots and riverbed moisture are constrained within natural boundaries, in a state of oscillatory equilibrium.

1.2.2 Properties of a complex system

Among the various biotic and abiotic components, synergy may emerge. This implies that these elements can collaborate through feedback loops, enhancing effects with a more significant impact than if they were isolated. This synergy may give rise to the property of emergence **(Corning, 2012)**, meaning the sum of the parts does not give the whole, but new properties and principles can emerge among their interactions.
The ecosystem is also subject to an external ecological disturbance, which is a physical force, agent, or process causing a perturbation within it **(Rykiel Jr, 1985)**. Typically, the ecological disturbance acts quickly and with a significant effect, resulting in the removal of a large amount of biomass. This can be observed in several ecosystems, for instance, by the devastation of forests due to fires and avalanches, as well as the impact of floods on riparian plants. These events can disrupt the balance of positive and negative feedbacks within the ecosystem, causing a shift away from equilibrium, as discussed by **Morgan Ernest and Brown (2001)**.
The ecosystem's capacity to withstand disturbance is referred to as the force of 'resistance' **(Lake, 2013)**. As mentioned in the previous section, in the river ecosystem, ecological disturbance is caused by floods, and the resistance force is provided by riparian vegetation. Additionally, the ecosystem has an important property called "resilience", defined as "a measure of the ability of the system to absorb changes of state variables, driving variables, and parameters, and still persist" **(Holling, 1973)**.
When the ecosystem is perturbed by the ecological disturbance, it naturally self-organizes into spatial patterns. Examples of self-organization in ecosystems are coral structures **(Van der Kaaden et al., 2020)**, flocking behavior in birds **(Cavagna et al., 2010)** and vegetation patters in arid zones **(Meron, 2015)**. Elements within the system collaborate by organizing and dividing tasks, forming self-organized cells, and working cooperatively **(Odum, 1959)** to establish efficient networks and patterns. This self-organization emerges from dynamic interactions among individual components; thus, the system is autonomous and lacks centralized control **(Levin, 1998)**. The self-organization and emergence of patterns represent adaptive processes **(Isaeva, 2012)** within the ecosystem. The adaptability property enables the ecosystem to continuously adjust itself to evolving needs, ensuring equilibrium and evolution, but making its predictions challenging.
In the river ecosystem, an example of self-organization is provided by morphological bars. Morphological bars represent mesoscale patterns characterized by sediment waves

with wavelengths proportional to the channel width. They form in both fine and coarse sediments **(Seminara and Tubino, 2001; Seminara, 2010)** due to hydro-morphodynamic interactions (see Figure 1.4).

Figure 1.4: Morphological bars are examples of self-organization in the river ecosystem. In the figure are shown the Tagliamento River (left) and Reno River (right). Adapted from Google Earth.

1.2.3 Behavior of a complex system

Predicting ecosystem behavior is also challenging because the ecosystem can remain in equilibrium for a long period and then undergo sudden shifts of abrupt changes. The state change can be gradual, following a linear or quasi-linear trend as external perturbations vary. Alternatively, it may cross a critical threshold, following a nonlinear complex trend and critical shifts **(Scheffer et al., 2001)**. In other cases, the ecosystem can also exhibit hysteresis **(Phillips, 2003)**. In the hysteresis cycle, two possible states, known as alternative stable states, exist for a given set of conditions. Thus, the return from the post-disturbance state to the pre-disturbance state may not encounter the same initial conditions due to a shift in the ecosystem's equilibrium. When the system is disturbed beyond a critical threshold, it may abruptly switch from one state to another. Several studies also show how ecosystems can exhibit multiple equilibria and states of coexistence (**e.g., Rietkerk et al., 2021; Bastiaansen et al., 2022**). Furthermore, numerous studies suggest that the ecosystem may not always reach a stable equilibrium but it may persist in periodic or chaotic oscillations (**e.g., Rinaldi and Scheffer, 2000; Reluga, 2004; Siteur et al., 2014; Grimaudo et al., 2022**).

From a mathematical perspective, complex systems can be analyzed using dynamical systems theory **(Newman, 2011)**. Among the various possible approaches, this theory also includes developing numerical models to explore the relationships among the system components and investigating their behavior over time.

Dynamical systems theory focuses on both the statics and dynamics of the system. Statics involves studying the system when there are no variations over time (e.g., equilibrium and hysteresis); dynamics examines the system's behavior over time and focuses on how the system variables change in response to disturbances (e.g., bifurcations, oscillations, chaos).

1.3 Research gap and motivations

In the river ecosystem, the interplay between hydro-morphodynamic disturbance and the vegetation resistance governs the predominance of either positive or negative eco-morphodynamic feedbacks, controlling river statics and dynamics **(Corenblit et al., 2014)**. Even though many eco-morphodynamic feedbacks are already known, the understanding of how these mechanisms interact with each other and govern river processes remains limited (**e.g, Wohl et al. 2015, Van Oorschot et al. 2017**). Recent studies show how such eco-morphodynamic interactions can make dynamics very complex and challenging to understand, including critical shifts and hysteresis (**e.g., Bertagni et al., 2018; Bau' et al., 2021**). Other studies demonstrate how the river system can exhibit oscillations and chaotic behavior, considering water-sediment interactions **(Salter et al., 2020; Stecca and Hicks, 2022)**.
Approaching the river ecosystem from the perspective of a complex system can help systematically understand these intricate nonlinear dynamics.
Therefore, this research aims to understand how the main positive and negative eco-morphodynamic feedbacks govern the complex equilibrium and dynamics of a simplified river ecosystem. To this end, simplified numerical models are developed to couple hydro-morphodynamics with vegetation dynamics.
This research can contribute to developing predictive models for a better understanding of river dynamics and for an improvement of river management.
In fact, critical shifts and hysteresis can challenge predictions of evolutionary trajectories due to rapid and potentially irreversible changes **(Bertoldi et al., 2014; Bertagni et al., 2018)**. Moreover, the chaotic behavior inherently limits the long-term predictability of system trajectories, modifying the approach to predictive eco-morphodynamic models, their development, and the interpretation of their results, as suggested for other geomorphic systems **(Phillips, 2003; Salter et al., 2020)**. Predictive models are vital for understanding river responses to environmental changes and guiding river management for risk mitigation and ecosystem restoration **(Wohl et al., 2015)**.
This becomes even more crucial with climate change, where the effects are observed in the variation of flood disturbance, whether in its frequency, magnitude, or timing **(Blöschl et al., 2017)**. Delays or advancements in flood disturbance timing can introduce an imbalance in the ecosystem functioning, for example, by altering the plant growing season.
Thus, understanding system equilibrium and dynamics is also crucial for predicting climate change effects and preserving the functionality and intrinsic value of ecological processes in river ecosystems.

1.4 Research objectives

The main objective of this PhD research is:

-**Understanding, through numerical models, the fundamental positive and negative feedbacks among vegetation, water, and sediments to investigate how they influence both the (i) static and (ii) dynamic behavior of a simplified river ecosystem.**

More specifically:

-Investigate the presence of hysteresis behavior and how spatial interactions may influence the system's equilibrium (static).

-Investigate the presence of chaotic behavior, define its properties and driving parameters and quantify the time scale of predictability (dynamic).

To this end, simplified numerical models are developed, including a 0D model (non-spatial) and a 1D model (spatial), coupling hydro-morphodynamics with vegetation dynamics. Both models include only the key eco-morphodynamic feedbacks and processes. These models are used to explore both the statics and dynamics of the river ecosystem by applying the theory of dynamical systems.

1.5 Thesis Outline: Next Chapters

In Chapter 2, eco-morphodynamic numerical models are described. From the traditional eco-morphodynamic problem, assumptions are made to derive the 1D model (spatial), with further simplifications for the 0D model (non-spatial), necessary to reduce the computational simulation time.
In Chapter 3, both models are used to investigate the statics of the system. The static behavior of the 0D model, that is when the overall balance of positive feedbacks prevail, is investigated. Subsequently, the effect of spatial interactions (1D model) on stability is examined.
In Chapter 4, both models are used to investigate the dynamic of the system, that is when the overall balance of negative feedbacks prevail. Periodic and aperiodic oscillations are investigated in both the non-spatial and spatial models.
In Chapter 5, the main results obtained will be summarized and discussed based on the conducted analysis and the established research objectives.

Chapter 2

Eco-morphodynamic models

2.1 Introduction

In recent years, several models have been developed to describe the dynamics between vegetation and hydro-morphodynamic processes **(Solari et al., 2016)**. Analytical models, despite their simplicity, have played a crucial role in isolating and understanding several ecological processes **(Camporeale and Ridolfi, 2006; Tron et al., 2014; Bertagni et al., 2018; Perona and Crouzy, 2018)**. For instance, **Camporeale and Ridolfi** (**2006**) investigate the effect of river hydrology on the distribution of vegetation along the riparian transect transverse to the river, while **Tron et al.** (**2014**) introduce an analytical model with stochastic components, which describes the interaction between root growth and groundwater oscillations. Moreover, **Perona and Crouzy** (**2018**) introduce a physically based stochastic model for the uprooting mechanism.
One of the earliest numerical models with on-line eco-morphodynamic feedbacks is the cellular automata one by **Murray and Paola** (**2003**), used to investigate the effect of sediment stabilization by roots on the channel pattern. Cellular rule-based models allow for simulating ecological processes with short computational times and with a relatively easy set-up but they have limitations in representing morphodynamic processes at the reach scale **(Coulthard et al., 2007)**. The development of physics-based numerical models has allowed to overcome this limitation. For instance, **Crosato and Saleh** (**2011**) solve the hydro-morphodynamic problem including vegetation, as a static element, which modifies the flow field and sediment transport. **Bertoldi et al.** (**2014**) additionally include vegetation dynamics, both growth and death, which actively influence hydro-morphodynamics. One of the most recent sophisticated model by **Van Oorschot et al.** (**2017**) incorporates also several ecological processes such as colonization, seedling establishment, and species interactions.

Although there are now several advanced models that include numerous ecological processes, for this analysis, simplified deterministic models are developed: a 0D model (non-spatial) and a 1D model (spatial). These models consider only the main fundamental feedbacks between vegetation and hydro-morphodynamics to (i) reduce the complexity of the analysis, to (ii) have greater control over the ongoing processes, and (iii) reduce the computational time required for simulations. Indeed, the study of dynamical systems

(i.e., bi-stability, bifurcation, chaos) requires complex analyses that can be more easily understood and untangled by simplified models. Moreover, the development of the non-spatial model enables conducting analytical analyses and gaining a deeper understanding of the system properties and dynamics. Finally, by modeling only the main feedbacks, they can be isolated and there is greater control over their interactions. The fundamental processes implemented in the models are shown in Figure 2.1. Vegetation consists of two components, the canopy and the root depth. The canopy increases fluid flow resistance by increasing local roughness, modifying flow patterns **(Nepf, 2012)** and reducing the bottom shear stress **(Le Bouteiller and Venditti, 2015)**. Moreover, the uprooting type II is implemented, since it's the most relevant plant death mechanism for most fluvial environments **(Edmaier et al., 2011; Bywater-Reyes et al., 2015)**. In addition, vegetation and root growth are implemented, where the maximum root depth is limited and controlled by the position of the groundwater level **(Fan et al., 2017)**.
In both models, the canopy modifies the flow field and reduces the bottom shear stress, inducing erosion at the downstream boundary between the vegetated and the bare areas due to an imbalance between the bedload fluxes entering and exiting the control volume. This process generates an intrinsic feedback whereby the presence and growth of vegetation increases the disturbance **(Bouma et al., 2007; Le Bouteiller and Venditti, 2015)** and thus potentially induces vegetation uprooting. This intrinsic process is common in many fluvial environments where scour occurs in close proximity to individual plants or vegetation patches. Depending on the configuration, erosion may occur upstream or laterally of small vegetated patches **(Zong and Nepf, 2012; Kim et al., 2015)** or downstream of larger patches covering the entire channel width **(Le Bouteiller and Venditti, 2015; Diehl et al., 2017)**.
In this analysis, simplified models are used to isolate this intrinsic mechanism which directly links the presence of vegetation to the magnitude of disturbance, investigating how it affects river equilibrium and dynamics. Numerical models can be useful tools for understanding river responses to environmental changes and guiding river management for risk mitigation and ecosystem restoration **(Wohl et al., 2015; Palmer and Ruhi, 2019)**.

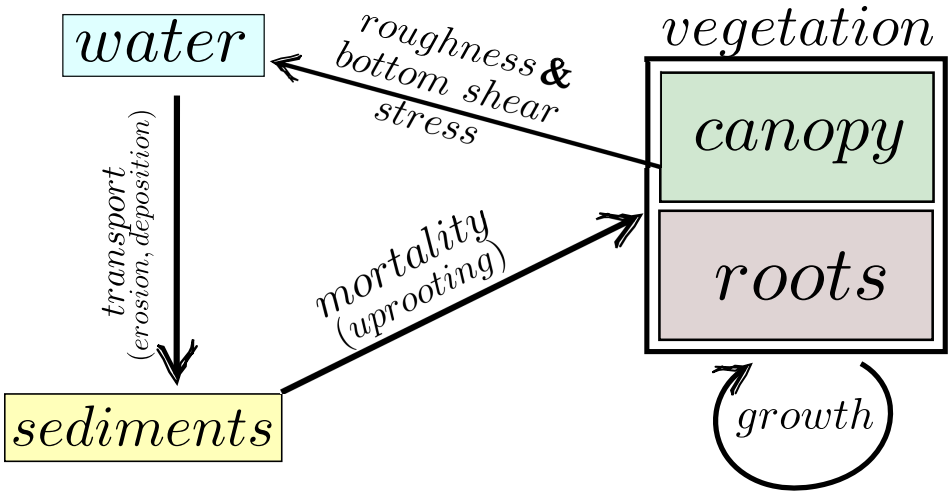

Figure 2.1: Key eco-morphodynamic processes implemented in the models.

2.2 Hydro-morphodynamic problem

For this analysis, the starting point is the traditional 1D model of the hydro-morphodynamic problem, as given by the Saint-Venant-Exner model.

$$\begin{cases} \dfrac{\partial h}{\partial t} + \dfrac{\partial q_x}{\partial x} = 0 \,, & \text{(a)} \\ \dfrac{\partial q_x}{\partial t} + \dfrac{\partial}{\partial x}\left(\dfrac{q_x^2}{h}\right) + gh(\dfrac{\partial h}{\partial x} + \dfrac{\partial z_B}{\partial x}) = -gh(S_{fx}) \,, & \text{(b)} \\ (1-p)\dfrac{\partial z_B}{\partial t} + \dfrac{\partial q_{Bx}}{\partial x} = 0 \,, & \text{(c)} \end{cases} \tag{2.1}$$

where the equation (2.1a) is the Continuity equation, the equation (2.1b) is the Momentum equation and the equation (2.1c) is the sediment continuity equation, namely the Exner equation. h is the water depth, x is the stream–wise coordinate, t is time, q_x is water discharge per unit width, g is is the gravitational acceleration, S_{fx} is the friction term, z_B is the riverbed level, q_{Bx} is the sediment discharge per unit width and p is the sediment porosity (refer to Figure 2.2). The equation (2.1a) indicates that, to ensure the conservation of water mass, temporal variations in the water level must be balanced by corresponding variations in the water discharge inflow and outflow along the x-axis. The equation (2.1b) delineates a force equilibrium within the x-axis: the two initial terms denote the inertia forces of the flow, accounting for temporal variations in water discharge and spatial flow variance. The subsequent two terms represent the gravitational pull on the water mass along the x-axis, while the final term represents head losses due to friction. The equation (2.1c) indicates that, to ensure the conservation of sediment mass, temporal variations in the riverbed level must be balanced by corresponding variations in the inflow and outflow sediment discharge along the x-axis.

An additional assumption is made, namely, that the riverbed evolves, and the flow field adapts instantaneously to the riverbed (i.e., steady flow condition is assumed $\frac{\partial h}{\partial t} \approx 0$, $\frac{\partial q_x}{\partial t} \approx 0$). Considering this assumption during subsequent morphodynamic steps, the Exner equation (2.1c) can be integrated with a larger time step, significantly reducing computational time **(Parker, 2004)**. Several simulations are conducted, both with and without this simplification, to prove that it did not significantly impact the analysis and results regarding the dynamic behavior of the system (the simulations are omitted here). This assumption leads to these further simplified equations:

$$\begin{cases} q_x = const \,, & \text{(a)} \\ \dfrac{dh}{dx} = \dfrac{S - S_{fx}}{1 - F_R^2} \,, & \text{(b)} \\ (1-p)\dfrac{\partial z_B}{\partial t} + \dfrac{\partial q_{Bx}}{\partial x} = 0 \,, & \text{(c)} \end{cases} \tag{2.2}$$

where S is the riverbed slope ($\approx \frac{\partial z_B}{\partial x}$) and F_R is the Froude number. The equation (2.2b) is the Gradually Varied Flow Equation.

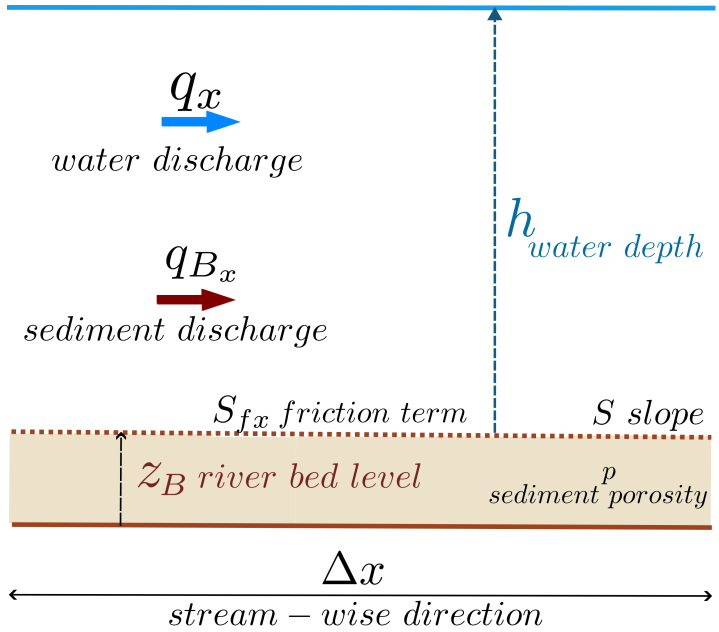

Figure 2.2: Sketch of the variables and parameters in the one-dimensional hydro-morphodynamic problem.

2.3 1D model (spatial) and feedback loop

2.3.1 Hydro-morphodynamic processes

Starting from the traditional hydro-morphodynamic problem, a 1D eco-morphodynamic model (spatial) is developed to capture the main feedbacks between vegetation and hydro-morphodynamic processes. A river reach with a rectangular cross-section, a central vegetated patch, and a riverbed composed of cohesionless, uniform sediment is considered. Starting from the system of equations (2.2), the hydrodynamic problem is solved by numerically integrating the Gradually Varied Flow Equation (2.2b) and using the Manning-Strickler method to evaluate the overall flow resistance, where the total shear stress is calculated as:

$$\tau = \frac{\rho g u|u|}{k_s^2 h^{1/3}}\,, \tag{2.3}$$

where ρ is the water density, g is the gravitational acceleration, u is the vertically averaged flow velocity, h is the water depth, and k_s is the Strickler coefficient (the inverse of the Manning coefficient n). The friction term S_{fx} is given by:

$$S_{fx} = \frac{|u^2|}{k_s^2 h^{4/3}}\,. \tag{2.4}$$

While the discharge may vary over time, it remains constant over the entire river reach during a single time step. The Exner equation (2.2c) is adopted to obtain the evolution

of the bottom elevation z_B of a riverbed composed of a uniform sediment. The q_{Bx} is determined through the standard Meyer-Peter Müller equation **(Meyer-Peter et al., 1948)**, which requires that the dimensionless Shields shear stresses θ exceeds a threshold value ($\theta_{cr} = 0.047$) for the onset of sediment transport:

$$\frac{q_{Bx}}{\sqrt{(s-1)g{d_s}^3}} = 8\,(\theta - \theta_{\mathrm{cr}})^{\frac{3}{2}} \tag{2.5}$$

where s is the sediment relative density and d_s is the sediment diameter.
The dimensionless Shields stress is given by:

$$\theta = \frac{|\tau|}{(\rho_s - \rho)g d_s} \ , \tag{2.6}$$

where ρ_s is the sediment density.
The Exner equation (2.2c) is solved by using a Godunov method **(Toro, 2001)**, and the water surface profile is obtained by solving the Gradually Varied Flow Equation using a standard solver for ordinary differential equations. The numerical domain is discretized in 200 uniform cells ($M = 200$). The total channel length is $L = 1500\ m$, the upstream coordinate of the vegetated patch is $x_{up} = 600\ m$, meanwhile the one downstream is $x_{dw} = 900\ m$. Uniform conditions are set at both the inlet and outlet of the numerical domain as initial conditions, and a fixed-bed simulation is conducted until steady state is reached. Then, morphodynamic simulations are performed, maintaining z_B fixed at both the inlet and the outlet.

2.3.2 Vegetation growth

In this model, the vegetation B is dimensionless and grows over time (t) following a logistic function **(Bertagni et al., 2018; Caponi and Siviglia, 2018)**, which can be integrated to obtain the following equation:

$$B(t) = \frac{B_0 K e^{\sigma t}}{B_0(e^{\sigma t} - 1) + K} \ . \tag{2.7}$$

where B is the vegetation biomass, B_0 is the biomass at the onset of the growth period, t is time, K is the maximum biomass value (carrying capacity, set to 1 in this model) and σ is the vegetation growth rate, which is constant. Vegetation only grows within the central vegetated patch, with biomass initialized at a small positive value B_{min} to ensure growth from bare soil.
The model considers root depth, denoted as ζ_{upr}, to grow over time (t) following an exponential function as:

$$\frac{d\zeta_{upr}}{dt} = \sigma_r \zeta_{upr} \ , \tag{2.8}$$

$$\zeta_{upr} = \min(\mathrm{offset}, \zeta_{upr}) \ , \tag{2.9}$$

where σ_r is the root growth rate and is constant. The root depth ζ_{upr} can reach a maximum value called "offset", which represents the distance between the riverbed z_B and the groundwater table level. It is considered that roots cannot grow below such a

level because they would die due to anoxia **(Tron et al., 2014)**. We also assume that the groundwater level is always parallel to and at a constant distance from the riverbed z_B. Moreover, in this model, there are two distinct time scales: the flood time scale (T_F) and the growth time scale (T_v), namely period of low flow. During flood periods, when the dimensionless shear stresses θ exceeds the threshold value θ_{cr} and solid transport occurs, vegetation may be partially or totally uprooted due to the erosion mechanism (uprooting type II).

2.3.3 Biogeomorphic feedbacks

The model considers that in every cell of the vegetated patch, vegetation increases the global flow resistance on the bed surface by increasing the roughness. Thus, it is assumed that the Strickler coefficient k_s decreases linearly, as described in **(Bertoldi et al., 2014; Caponi and Siviglia, 2018)**:

$$k_s = k_{s,g} + (k_{s,v} - k_{s,g})\frac{B(t)}{K}\,, \tag{2.10}$$

where $k_{s,g}$ refers to the value attributed to the bare soil while $k_{s,v}$ is the roughness of a fully vegetated bed and $k_{s,v} < k_s$. As roughness increases, flow velocity decreases nonlinearly, modifying the Shields stress θ and thus reducing sediment transport. This leads to an imbalance in transport capacity between the vegetated and bare areas in the downstream part of the vegetated patch, consequently leading to erosion.
The vegetation B also reduces the bottom shear stress, affecting sediment transport **(Yager and Schmeeckle, 2013; Le Bouteiller and Venditti, 2015)**. Since direct quantification of the bottom shear stress is extremely difficult in the presence of vegetation, the reduction of bottom shear stress is modeled by multiplying the total shear stress τ by a factor $\gamma < 1$ **(Le Bouteiller and Venditti, 2015; Caponi and Siviglia, 2018)** and compute the sediment flux using the reduced Shields stress, $\gamma\theta$. The parameter γ ranges between 0 and 1 and it is chosen as:

$$\gamma = \left(\frac{k_s(t)}{k_{s,g}}\right)^2. \tag{2.11}$$

During flood periods, the type II uprooting mechanism occurs **(Edmaier et al., 2011; Pasquale et al., 2012; Bywater-Reyes et al., 2015)**. Although experimental evidence suggests type II uprooting typically occurs before complete root biomass excavation **(Edmaier et al., 2015)**, it is assumed that uprooting occurs when flow-induced erosion fully excavates to root depth ζ_{upr}. This assumption is made to avoid the introduction of an additional threshold parameter. Thus, two cases are possible: if $\Delta z_B \geq \zeta_{upr}$ uprooting occurs and vegetation in the specific cell is completely removed; if $\Delta z_B < \zeta_{upr}$, uprooting does not occur.

2.3.4 Model workflow

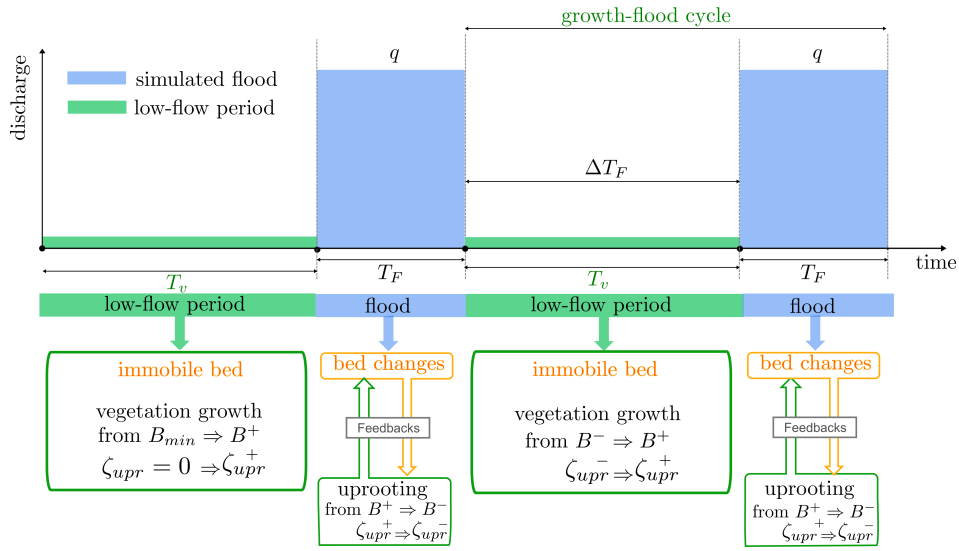

Figure 2.3: Sketch of the eco-morphodynamic model functioning. An alternating sequence of constant floods (T_F) and low flow periods (T_v) is considered. The time interval between two successive floods is ΔT_F. Since T_F (hours, days) $\ll T_v$ (months, years), the duration of the flood (T_F) and the growing period (T_v) are not to scale. Vegetation and root depth grow starting from B_{min} and $\zeta_{upr} = 0$, reaching the value B^+ and ζ_{upr}^+ by the end of the growing season. Subsequently, during the initial flood period, the uprooting reduces the values of vegetation and root depth to B^- and ζ_{upr}^-. The surviving vegetation and the remaining root depth resulting from the initial flood (average values B^- and ζ_{upr}^-, respectively) are used as the starting conditions for the subsequent growth period and so forth.

The workflow used is a simplified version of **Caponi et al. (2020)**, and its schematic representation is illustrated in Figure 2.3. This case study is chosen to specifically reproduce an erosion process forced only by the presence of vegetation **(Le Bouteiller and Venditti, 2014; Caponi and Siviglia, 2018)** similarly to the experimental conditions used by **Le Bouteiller and Venditti (2014)** and **Diehl et al.(2017)**. This choice allows to isolate the feedback mechanism between vegetation and erosion and thus capture its effects on system dynamics. Although erosion occurs at the downstream boundary in this configuration, it's important to note that the configuration remains applicable regardless of the erosion's location, be it upstream, downstream, or next to small vegetated patches. This setup broadly represents the dynamics at the boundary between vegetated and bare areas, where the presence of biomass intensifies erosion. The main advantage of the chosen configuration is that it provides complete control over the erosion process.

A sequence of growth-flood cycles is considered, alternating constant floods q and low flow periods. Vegetation grows and develops root depth ζ_{upr} only during low flood periods, when there are no morphological changes (immobile bed). Feedbacks between vegetation and hydro-morphodynamic processes (the correction of the bed shear stress, the correction of the flow resistance and the uprooting) take place only during floods,

when sediment transport, and consequently erosion, occurs.

The flood time scale T_F (hours, days) is much faster than the growth time scale T_v (months, years). Therefore, within the model, flood disturbances are considered as impulses, and it is assumed that vegetation and root depth growth during flood events are negligible **(Bertagni et al., 2018)**. It is also assumed that floods repeat deterministically with a fixed period ΔT_F. The assumption that the flow repeats deterministically is a strong simplification, but it allows for better isolation and control of the effects of internal mechanisms without the influence of external stochastic oscillations.
During low flow periods, vegetation grows logistically towards its equilibrium value (carrying capacity K). If the growth rate σ is equal to 1 (refer to Figure 2.4), the vegetation B reaches 99.9% of its maximum growth (i.e., $\frac{B}{K} = 0.999$) at time $t = T_v$. If σ is equal to 0.1, the vegetation B reaches 99.9% of its maximum growth at time $t = 10T_v$. The time scale t^* is dimensionless and it is equal to $t^* = \frac{t}{T_V}$. σ represents physically the velocity of vegetation growth; thus, by modifying this parameter, different vegetation types can be modeled.

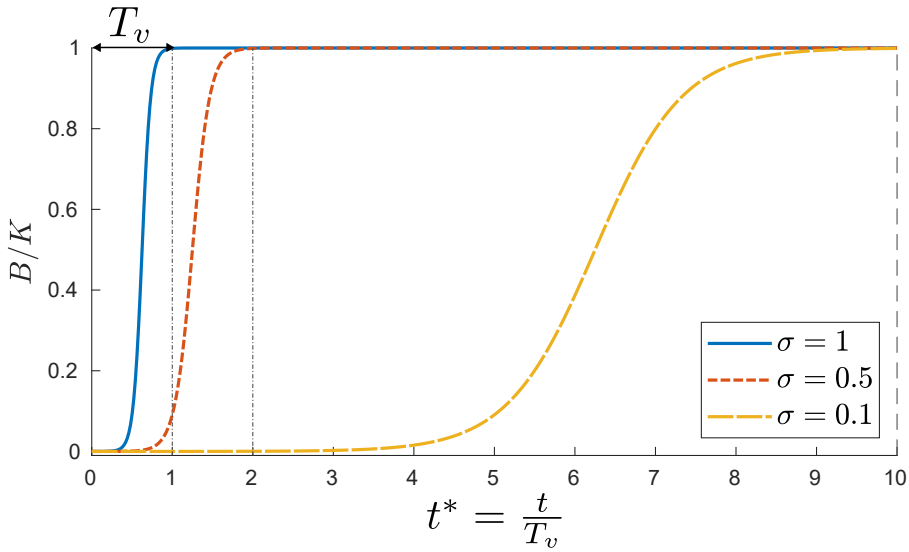

Figure 2.4: Logistic growth of vegetation types with different growth rates σ. If the growth rate σ is equal to 1, the vegetation B reaches 99.9% of its maximum growth (i.e., $\frac{B}{K} = 0.999$) at time $t = T_v$. If σ is equal to 0.1, the vegetation B reaches 99.9% of its maximum growth at time $t = 10T_v$ and so forth. The time scale t^* is dimensionless, and it is equal to $t^* = \frac{t}{T_V}$.

During the initial low flood period, vegetation and root depth grow starting from a uniform distribution, i.e., in every cell $B = B_{min}$ and $\zeta_{upr} = 0$, reaching the average value in the patch B^+ and ζ^+_{upr} by the end of the growing season. Subsequently, during the first flood period, feedbacks between vegetation and hydro-morphodynamic processes are activated, potentially leading to uprooting and reducing vegetation and the root depth to the average value in the patch B^- and ζ^-_{upr}. The surviving vegetation from the initial flood (average values B^- and ζ^-_{upr}) is used as the starting condition for the subsequent growth

period and so forth.
The case study is a straight channel with a wide, rectangular cross-section, with an initial slope S, where vegetation can grow only in the central patch, while upstream and downstream there are bare soil regions composed of cohesionless, uniform sediment (refer to Figure 2.5A), **(Caponi and Siviglia, 2018)**.
At the initial condition (at $t = 0$), the slope S and vegetation distribution are uniform across the entire domain. Due to the presence of vegetation in the central patch, spatial differences arise in the physical parameters involved in the processes. During flood periods, the presence of vegetation reduces the flow velocity and increases the water depth h in the central patch, resulting in a greater imbalance in transport capacity between the vegetated patch and the bare soil regions. The imbalance in transport capacity induces erosion over time (t) in the downstream interface (between the vegetated patch and the bare soil region) and deposition in the upstream interface, increasing the slope within the vegetated patch (refer to Figure 2.5B). When the erosion Δz_B completely exceeds the root depth ζ_{upr}, the vegetation in the specific cell is uprooted and the riverbed adjusts to the new conditions. If the erosion Δz_B does not excavate completely the root depth ζ_{upr}, the vegetation in the specific cell resists to the hydro-morphodynamic disturbance and remains anchored in the patch (refer to Figure 2.5C). The average value of the remaining vegetation is B^-.
After the flood, during the growth period, vegetation and root depth show distinct growth due to different initial conditions in the uprooted and non-uprooted zones. Thus, at the end of the growth period, a spatially heterogeneous configuration is observed within the vegetated patch as well (refer to Figure 2.5D), and the average value of the vegetation is defined as B^+. This configuration is used as the starting condition for the subsequent flood period and so forth.

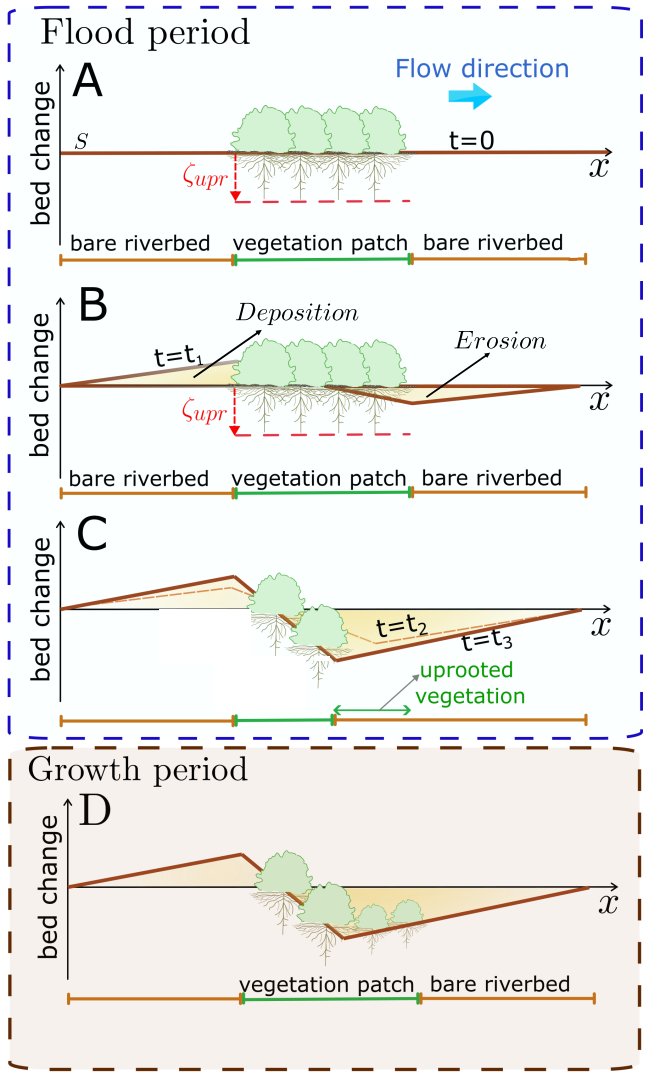

Figure 2.5: Case study configuration of the spatial model. (A) the case study is a straight channel where vegetation can grow only in the central patch, while upstream and downstream, there are bare soil regions. At the initial condition (at $t = 0$), the slope S and vegetation distribution are uniform across the entire domain. (B) During floods, (time $t = t_1$), bed level changes occur due to biogeomorphic feedbacks, inducing erosion at the downstream end of the patch and inducing deposition at the upstream end. (C) When erosion Δz_B reaches the root depth ζ_{upr} in time ($t = t_2$ and $t = t_3$), the vegetation in the specific cell is uprooted, and the riverbed adjusts to the new condition. (D) After the flood, during the growth period, vegetation and root depth grow slowly in the uprooted zone and faster in the not-uprooted zone due to different initial conditions. This final configuration is used as the starting condition for the subsequent flood period and so forth.

2.3.5 Negative feedback loop

The implemented feedbacks between vegetation and hydro-morphodynamic processes generate a total negative feedback loop (Figure 2.6): more vegetation increases the roughness, reduces the flow velocity and increases water depth h (effect in same direction +) within the vegetated area. An increased water depth results in a reduction of sediment transport, leading to a greater imbalance in transport capacity between vegetated and bare areas. Thus, higher water depth h leads to more erosion in the downstream part of the vegetated patch (effect in same direction +). More erosion leads to vegetation uprooting (effect in opposite direction -). Multiplying the negative effect by the positive effects results in a total negative loop.

However, the strength of the negative feedback loop is governed by the ratio between

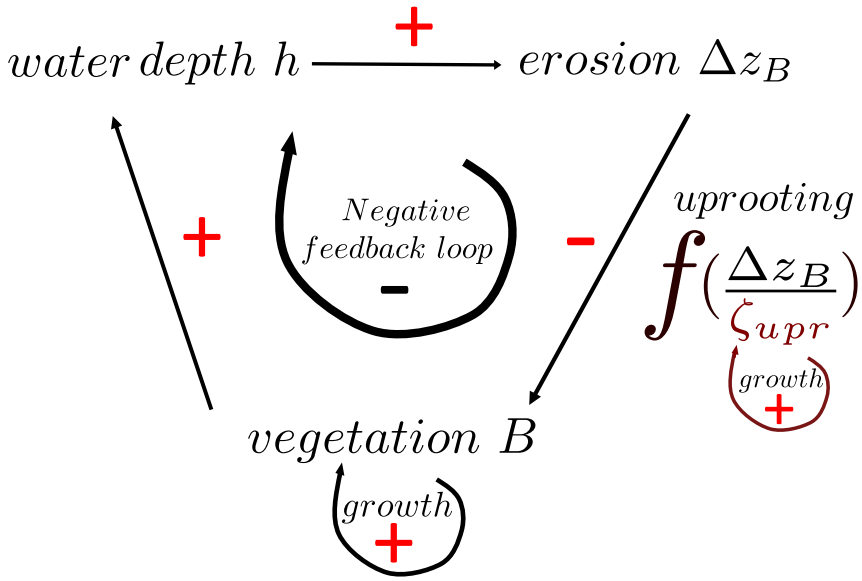

Figure 2.6: The feedback interactions among vegetation, flow field, and sediment transport generate a total negative feedback loop: more vegetation leads to higher water depth h (effect in same direction +). Higher water depth h leads to more erosion Δz_B (effect in same direction +). More erosion leads to a higher probability of vegetation uprooting (effect in opposite direction -). Vegetation and root depth can grow during low flood periods (positive effect). If all the positive/negative effects are multiplied, a total negative feedback loop is obtained, which is in sum a counterbalanced feedback. However, the strength of the negative feedback loop is governed by the ratio between erosion and root depth and can also be completely inhibited, resulting in a net positive feedback.

the hydro-morphodynamic disturbance (erosion) and root resistance (root depth) and can also be completely inhibited by root growth (positive effect). When root growth inhibits the negative effect of uprooting, the entire negative feedback loop is inhibited, resulting in a net positive feedback. The inhibition of the negative feedback loop suppresses the oscillations, and the system is driven towards steady state. The inhibition occurs when (i) roots grow quickly or deeply into the riverbed (high value of σ_r or $offset$), surviving

the uprooting and reaching over time the vegetated state; when (ii) roots grow slowly or shallowly into the riverbed (low value of σ_r or $offset$), being uprooted and pushed over time toward bare soil. In this second case, roots grow minimally during low flow periods; nevertheless, this effect is so small that it can be considered negligible (and the solution can be considered stable as bare soil).

2.4 0D Model (non-spatial) and feedback loop

2.4.1 Hydro-morphodynamic processes

A zero-dimensional (0D) discrete-time model is developed **(May, 1974; Reluga, 2004)** (non-spatial) aiming to derive the simplest model that represents the fundamental physics occurring at the boundary between vegetated and bare areas **(Paola and Leeder, 2011)**. In this conceptual model (see Figure 2.7), a control volume of length L_v is being considered to represent a vegetated patch within a river composed of cohesionless, uniform sediment. The main assumptions of the model are uniform flow conditions for the water depth h_{unif}, a constant slope S over time and a rectangular cross section. The hydrodynamic problem is solved by using the Manning-Strickler method for evaluating the global flow resistance, where the total shear stress is calculated as shown in equation (2.3).
Riverbed erosion (Δz_B) results from the imbalance between unit-width bedload flux entering (q_B^{IN}) and leaving (q_B^{OUT}) the control volume and is obtained by applying the sediment continuity equation in discrete form (over a time interval Δt):

$$\Delta z_B = \frac{q_B^{IN} - q_B^{OUT}}{L_v} \Delta t \ . \tag{2.12}$$

It is considered that vegetation B increases the global flow resistance by modifying the Stricker coefficient k_s, resulting in changes in the bedload flux q_B^{IN} entering the control volume over time. The bedload flux leaving the control volume is assumed to be constant and calculated setting $k_s = k_{s,g}$. This assumption is made because the 0D model aims to replicate the erosion mechanism of the 1D model. Indeed, the imbalance between q_B^{IN} and q_B^{OUT} induces erosion, similarly to what happens downstream of the patch in the 1D model.
The q_B is determined through the standard Meyer-Peter Müller equation **(Meyer-Peter et al., 1948)**, which requires that the dimensionless shear stresses θ exceeds a threshold value ($\theta_{cr} = 0.047$) for the onset of sediment transport.
Under the previous mentioned assumptions, the Shields stress is given by:

$$\theta = \left(\frac{q}{k_s} \right)^{\frac{3}{5}} \frac{S^{\frac{7}{10}}}{(s-1)d_s} \ , \tag{2.13}$$

where q is the flood discharge and s is the sediment relative density (set to 2.65).

2.4.2 Vegetation growth

In this model, vegetation B and root depth ζ_{upr} grow following the equations (2.7, 2.8, 2.9) described in the 1D model (refer to Subsection 2.3.2).

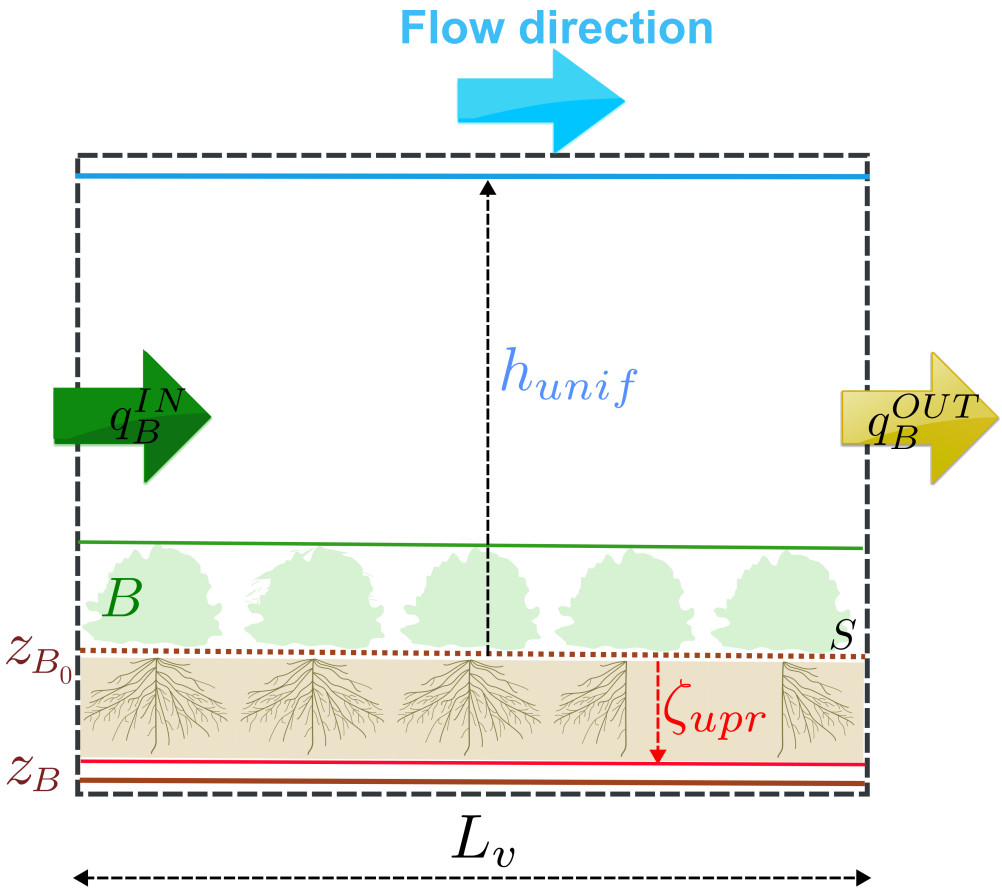

Figure 2.7: Sketch of the 0D model. L_v is the length of the control volume and represents the vegetated patch within a river. Uniform flow conditions are assumed for the water depth h_{unif}, with a constant slope S over time, and a rectangular cross-section. Vegetation B modifies the global flow resistance and generates an imbalance between the bedload fluxes entering (q_B^{IN}) and exiting (q_B^{OUT}) the control volume, consequently leading to riverbed erosion. Riverbed erosion Δz_B is the difference between the final riverbed z_B and the initial riverbed z_{B_0}. ζ_{upr} is the root depth.

2.4.3 Biogeomorphic feedbacks

It is considered that vegetation B increases the global flow resistance and reduces the shear stresses on the bed surface as described in the equations (2.10, 2.11) of the 1D model (refer to Subsection 2.3.3).
During flood periods, the uprooting occurs when flow-induced erosion excavates the root depth ζ_{upr} and reduces the anchoring resistance of the vegetation, leading to the partial or complete removal of it. In the 0D model, uprooting is modeled differently from the 1D model, as shown in Figure 2.8. Indeed, the uprooting of the 0D model aims to represent the average uprooting of the 1D patch, as explained in the Appendix (A).

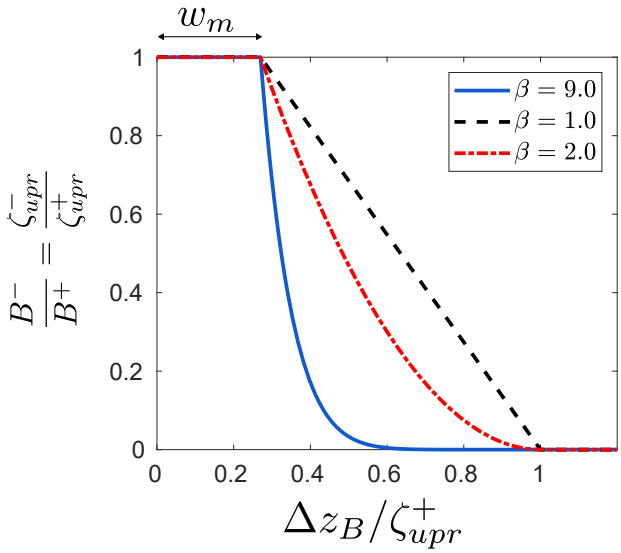

Figure 2.8: Uprooting mechanism occurring during flood periods (T_F) described by equations (2.14) and (2.15). B^+ and ζ^+_{upr} respectively represent the vegetation and the root depth before the uprooting, and B^- and ζ^-_{upr} represent the vegetation and the root depth after the uprooting, while Δz_B is the riverbed erosion. β is a nonlinear shape parameter, and the constant w_m represents the minimum fraction of ζ_{upr} required for uprooting mechanism to occur (in this graph equal to 0.27).

B^+ and ζ^+_{upr} respectively represent the vegetation and the root depth before the uprooting, and B^- and ζ^-_{upr} represent the vegetation and the root depth after the uprooting, while Δz_B is the riverbed erosion. β is a shape parameter, where if $\beta = 1$, the function is linear; if $\beta > 1$ the rate of vegetation decrease, accelerates. The constant w_m represents the minimum fraction (range from 0 to 1) of ζ_{upr} required for uprooting mechanism to occur. Therefore, three possible cases emerge: if erosion remains below the fraction w_m of ζ_{upr}, uprooting does not occur and B^-= B^+, ζ^-_{upr}=ζ^+_{upr}; if erosion excavates the entire ζ_{upr} length, the vegetation is completely removed and both vegetation B and root depth ζ_{upr} are reset to their initial values ($\zeta_{upr} = 0$ and $B = B_{min}$). If ζ_{upr} is in between these two extreme cases, only a portion of the vegetation and root depth is removed.

Therefore, the uprooting is modeled with the following equations:

$$B^- = \begin{cases} B^+ & \text{if} \quad 0 \leq \Delta z_B < w_m \zeta^+_{upr} \,, & \text{(a)} \\ \left(1 - \frac{\frac{\Delta z_B}{\zeta^+_{upr}} - w_m}{1 - w_m}\right)^{\beta} B^+ & \text{if} \quad w_m \zeta^+_{upr} \leq \Delta z_B < \zeta^+_{upr} \,, & \text{(b)} \\ B_{min} & \text{if} \quad \Delta z_B \geq \zeta^+_{upr} \,. & \text{(c)} \end{cases} \tag{2.14}$$

$$\zeta^-_{upr} = \begin{cases} \zeta^+_{upr} & \text{if} \quad 0 \leq \Delta z_B < w_m \zeta^+_{upr} \,, & \text{(a)} \\ \left(1 - \frac{\frac{\Delta z_B}{\zeta^+_{upr}} - w_m}{1 - w_m}\right)^{\beta} \zeta^+_{upr} & \text{if} \quad w_m \zeta^+_{upr} \leq \Delta z_B < \zeta^+_{upr} \,, & \text{(b)} \\ 0 & \text{if} \quad \Delta z_B \geq \zeta^+_{upr} \,, & \text{(c)} \end{cases} \tag{2.15}$$

where for equations (2.14a) and (2.15a) uprooting does not occur, for equations (2.14c and 2.15c) vegetation and root depth are completely removed and for equations (2.14b and 2.15b) only a portion of the vegetation and root depth is removed.

2.4.4 Model workflow

The 0D model workflow is equal to the one described in the 1D model (refer to Subsection 2.3.4).

2.4.5 Negative feedback loop

As in the spatial model, also in the non-spatial model, the feedbacks interaction between vegetation and hydro-morphodynamic processes generate a total negative feedback loop (refer to Subsection 2.3.3 and Figure 2.6). However, in the extreme cases of the systems (2.14) and (2.15), i.e., equations (2.14a) and (2.14c) and equations (2.15a) and (2.15c), it is observed that the uprooting negative effect is inhibited, consequently leading to the inhibition of the total negative feedback loop. This can be physically explained by root depth dynamics. If roots grow quickly or deeply into the riverbed (high value of σ_r or $offset$), they are more likely to survive the uprooting and reach the vegetated state over time. On the contrary, if roots grow slowly or shallowly into the riverbed (low value of σ_r or $offset$), they are more likely to be uprooted and to be pushed by the disturbance toward bare soil. In this second case, roots grow minimally during low flow periods; nevertheless, this effect is so small that it can be considered negligible (and the solution can be considered stable as bare soil).

2.5 Limitations of the models

It's evident that both the 0D and 1D models used in this analysis are highly simplified, and strong assumptions have been made, as listed in the previous sections. The low-dimensional nature of the analyzed problems and the simplicity of the equations distance the research from application in a real river.
The vegetation modeling is also highly simplified as the biomass B is treated as a single variable for both below-ground biomass and above-ground biomass. In addition, root depth grows independently of both biomass B and riverbed.
Furthermore, many important biogeomorphic feedbacks have not been considered, such as soil cohesion caused by roots or the burial mechanism for mortality.
The external flood disturbance is considered deterministic and constant, and the stochastic variability has not been taken into account.

However, all these simplifications (and also others described subsequently) were made deliberately, and the model was streamlined by isolating only the essential elements to understand the main mechanisms governing the dynamics of the system and the seed of oscillations and chaos.
The aim of this research is not to describe a real river, but merely to understand the functioning of some key ecomorphodynamic relations, which, although simple, can already exhibit very complex dynamics.

Static equilibrium

Chapter 3

Bi-stability and multi-stability

3.1 Introduction

In ecosystems, biotic elements interact with each other and with the abiotic components of the surrounding environment through nonlinear interactions, which lead to positive and negative feedbacks. For the same external environmental condition, the ecosystem can show multiple equilibrium states, defined as alternative stable states **(Scheffer et al., 2001)**. Therefore, positive feedback loops push the ecosystem outside its equilibrium towards alternative stable states. **May** (**1977**) was the first author to theoretically demonstrate the existence of alternative stable states in several ecosystems.
Moreover, ecosystems face constant exposure to external disturbances that modify the external conditions altering their equilibrium **(Morgan Ernest and Brown, 2001)**. Ecosystems respond to external disturbances by exerting a force of resistance. They also demonstrate a force of resilience by absorbing changes and self-organizing, persisting against disturbances **(Holling, 1973)**. In the river ecosystem, plants act as ecosystem engineers **(Gurnell, 2014)** and resist flood disturbances while modifying the environment and pushing the system towards the ecological phase of biogeomorphic succession **(Corenblit et al., 2014)**. In particular, roots exert an anchoring force to the riverbed, preventing plants removal by the hydro-morphodynamic disturbance **(Edmaier et al., 2011)**.
External disturbances can induce abrupt changes and critical transitions as observed in a variety of ecosystem models including lakes, coral reefs, salt marshes, oceans, forests, and arid lands **(Scheffer et al., 2001; Marani et al., 2010; Van der Kaaden et al., 2020)**. For certain values of the external disturbance, the response of ecosystems may be smooth and continuous. However, for some values of the external disturbance the response could be non-trivial and the system can shift in alternative stable states (hysteresis).
To better explain this concept, ecosystems can be visualized as a marble **(Scheffer et al., 2001)** where the unstable equilibrium corresponds to the summit of a hill (Figure 3.1 and Figure 3.2). A minor perturbation can induce the ecosystem to transition into one of the downhill, or basins of attraction (the two alternative states). The interplay between hydro-morphodynamic disturbance and vegetation resistance governs river dynamics **(Corenblit et al., 2014)**. Therefore, if the hydro-morphodynamic disturbance prevails, the system is pushed towards a single stable state, bare soil; if the vegetation resistance prevails, it is pushed towards the ecological phase. However, for some external environmental

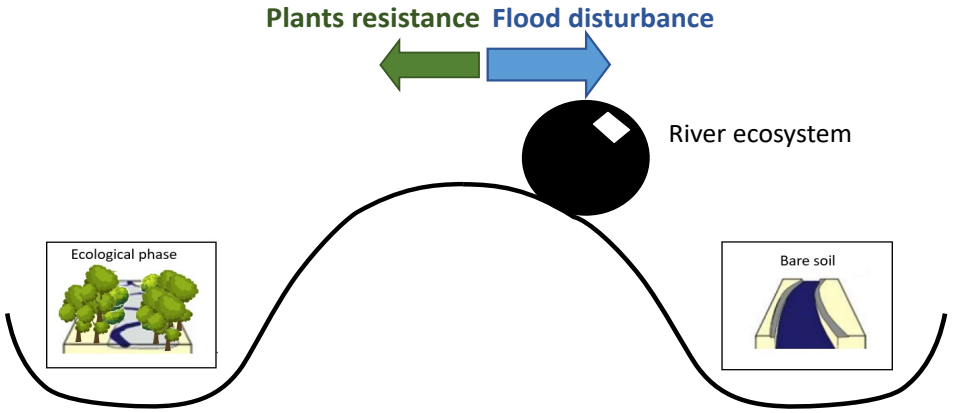

Figure 3.1: Ecosystems can be conceptualized as a marble. The unstable equilibrium corresponds to the summit of a hill. A minor perturbation can induce the ecosystem to transition into one of the downhill (the two alternative states). In the river ecosystem plants resist against flood disturbance to conducive to the ecological phase, instead the flood disturbance usually acts quickly and with a big effect removing a large amount of biomass and pushing the ecosystem to bare soil (as shown in the graph).

conditions, the system can show hysteresis. Due to the hysteresis behavior (Figure 3.2), if the disturbance is increased from the upper branch and the transition to the other branch of equilibrium (tipping point F2) occurs, when then the disturbance is reduced again, the ecosystem does not return to its previous state. Instead, a significant reduction in the disturbance (up to F1) is required to recover the system by shifting back to the upper branch. Consequently, under the same disturbance regime, two equilibria are possible depending on the initial conditions. Moreover, as shown in Figure 3.2, the ecosystem exhibits catastrophic shifts and tipping points, where the behavior of the system changes abruptly.

In the river ecosystem, the potential presence of alternative states has already been emphasized in some studies **(Dent et al., 2002; Corenblit et al., 2014; Bau' et al., 2021)**. In these works, authors demonstrate how the system can show multiple stable equilibrium points and undergo irreversible shifts, depending on the initial conditions. Stable alternative states due to different initial conditions of roots have also been studied in laboratory experiments **(Wang et al., 2016)**.
However, despite a limited number of mainly qualitative studies, the concept of alternative states has not yet been extensively investigated in the context of the river ecosystem.
Moreover, even though there are some theoretical works describing how homogeneous non-spatial ecosystems behave, there are only few works describing spatial-heterogeneous ecosystems behavior. Recent research shows how the stability graph (shown in Figure 3.2) becomes considerably more complex when space is involved, due to coexisting stable states **(Bastiaansen et al., 2022)**, multi-equilibria **(Meron et al., 2019)** and spatial self-organized patterns **(Meron, 2015)**. One of the most important implication of these works is that spatial ecosystems seem to exhibit greater resilience compared to non-spatial theoretical models. In fact, by organizing in spatial patterns and in coexisting states, spatial

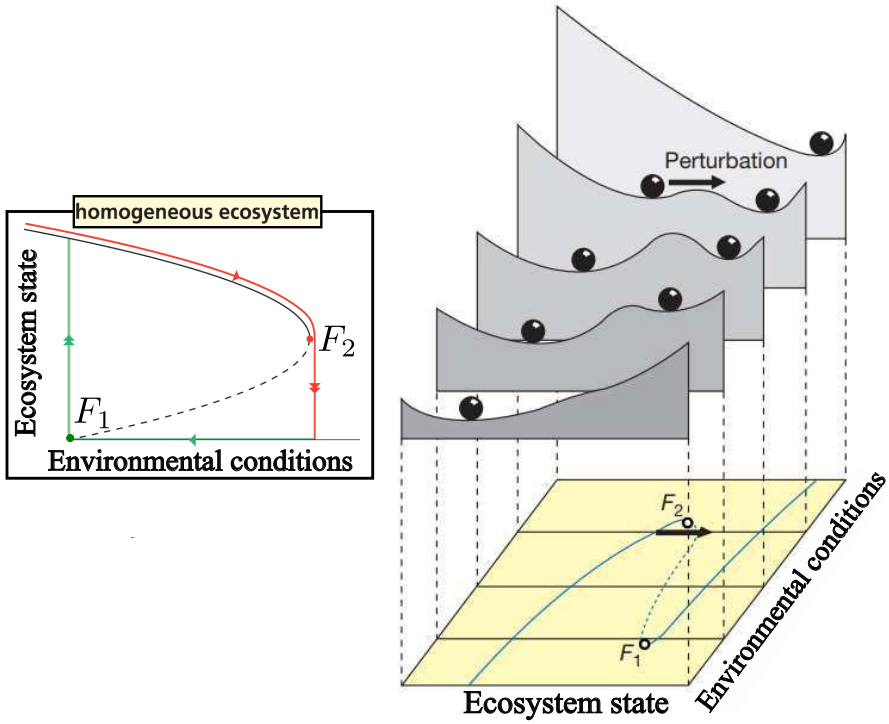

Figure 3.2: Ecosystem stability graph (on the left), and conceptual interpretation with the equilibrium of a marble (right). For some values of the external disturbance (environmental conditions), the ecosystem stability graph can exhibit abrupt shifts and two alternative states, i.e., hysteresis. If the disturbance from the upper branch is increased and a transition to the other branch of equilibrium (tipping point F2) occurs, when then the disturbance is reduced again, the ecosystem does not return to its previous state. Instead, a significant reduction in the disturbance (up to F1) is required to recover the system by shifting back to the upper branch. Adapted from **Scheffer et al.** (**2001**) and **Rietkerk et al.** (**2021**).

ecosystems do not abruptly shift in between two stable alternative states, preventing catastrophic shifts **(Rietkerk et al., 2021)**. For instance, vegetation in savanna and dryland ecosystems, self-organize in spatial patterns. In Figure 3.3 is illustrated the difference between a homogeneous ecosystem (A) and a spatial ecosystem (B) behavior. As shown in Figure 3.3B, the Turing bifurcation is the point where uniform vegetation coverage destabilizes due to worsening external conditions. This leads to the emergence of distinct and regular patterns known as Turing patterns **(Turing, 1990)**. Furthermore, the Busse balloon (grey area in Figure 3.3B) is a region of the parameter space in mathematical models where regular spatial patterns with different wavelengths exist and are stable. Starting from the Turing bifurcation and inside the Busse balloon, ecosystems create alternative pathways and avoid tipping points **(Rietkerk et al., 2021)**. Thus, ecosystems increase their resilience because they persist and do not tip to another basin of attraction. Heterogeneous spatial ecosystems avoid critical transitions and they transitate smoothly and gradually **(Holmgren and Scheffer, 2001)**. Therefore, in real-world data, tipping

points appear to be consistently much fragmented—and thus more gradual with multiple smaller intermediate steps due to a partial restructuring of the ecosystem **(Bastiaansen et al., 2022)**, rather than a single large collapse **(Rosier et al., 2020)**. Understanding how

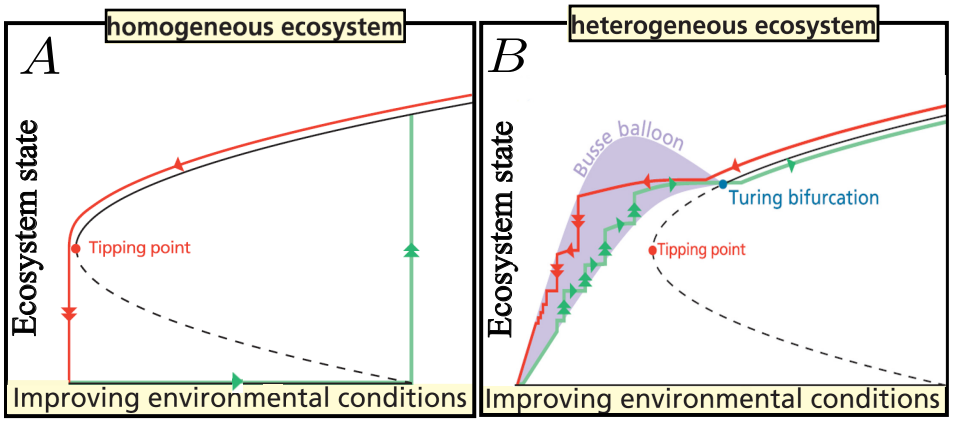

Figure 3.3: (A) Illustration of the hysteresis behavior for a non-spatial homogeneous ecosystem. (B) Illustration of the more complex behavior for multi-stable spatial ecosystems. Here, within the grey area, named the "Busse balloon," spatially self-organized stable states can persist, starting from a specific point, the Turing bifurcation. Instead of a critical transition, multiple smaller and gradual shifts occur. Solid lines represent stable equilibria, dashed lines indicate unstable equilibria. Double arrows signify ecosystem shifts, while single arrows indicate minor ecosystem adjustments. Adapted from **Rietkerk et al.** (**2021**).

spatial interactions modify the equilibrium graph, tipping points, and resilience have not been yet investigated in the context of the river ecosystem.
Quantifying the equilibrium graph and the resilience of spatial ecosystems is essential for developing efficient tools that can contribute to a better understanding of river dynamics and to improving river management. Ignoring alternative states of ecosystems and the potential for catastrophic shifts could lead to significant economic and ecological losses, and restoration projects may be costly or ineffective **(Scheffer et al., 2001)**. To manage an ecosystem optimally, it is necessary to possess a thorough understanding of its equilibrium graph.

Therefore, in this chapter, the aim is to explore how the main inherent feedbacks between vegetation and hydro-morphodynamics affect the static equilibrium graph of the simplified river ecosystem, namely when the system is at steady state. It's important to highlight that in this chapter, the system always reaches a steady state because the negative feedback loop is inhibited and positive effects prevail, as explained in Subsection (2.3.3) and shown in Figure 2.6. In fact, the inhibition of the negative feedback loop suppress the oscillations, and the system is driven towards steady state (alternative stable states or multiple states).
In all the results of this chapter, the root growth parameter values inhibit the negative feedback loop, promoting instead positive effects that push the ecosystem towards stable states (refer to Figure 1.3).

The main objectives of this chapter are defined as follows:

(i) to investigate the presence of hysteresis in the non-spatial model and understand the driving-parameters of the process (section 3.2).

(ii) to analyze how spatial interactions (1D model) may influence the equilibrium graph of the system and how this impacts the resilience (section 3.3).

The method involves numerical simulations, and the models utilized are those described in Chapter 2.

3.2 Bi-stability in a non spatial eco-morphodynamic model

3.2.1 Numerical simulations

With the 0D model three sets of simulations (A), (B), (C), are performed by modifying parameters as shown in Figure 3.4 and as illustrated in Table 3.1.
(i) First, the two parameters governing the root depth growth in equations (2.8) and (2.9)

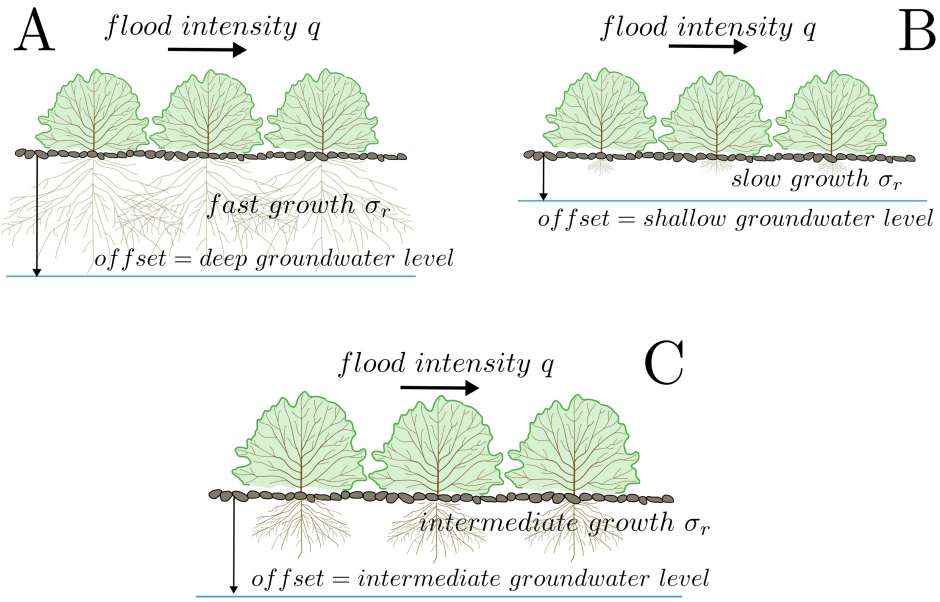

Figure 3.4: Three sets of numerical simulations are performed: (A) limit condition for which roots can grow deep (deep $offset$) and fast (high σ_r) into the riverbed; (B) limit condition for which roots grow shallow (shallow $offset$) and slow (low σ_r) into the riverbed; (C) intermediate condition for which there are intermediate values of the $offset$ and σ_r.

are modified: the velocity σ_r and the maximum depth *offset*. In the set of simulations (A) a limit condition for which roots can grow deep ($\zeta_{upr_{max}} = 2.7\ m$) and fast into the riverbed is chosen. With $\sigma_r = 1$, starting from the initial condition $\zeta_{upr_i} = 0.01\ m$, roots reach immediately 1 m depth ($\approx$ 1 growth-flood cycles). In the set of simulations (B) a

Table 3.1: Run parameters for three different set of simulations A,B,C.

Parameter	set A	set B	set C	Unit
σ_r	1	0.0001	0.002	-
$offset$	2.7	0.15	1.2	m
q	[0-20]	[0-20]	[0-20]	$m^2 s^{-1}$
ζ_{upr_i}	[0-$offset$]	[0-$offset$]	[0-$offset$]	m

limit condition is chosen for which roots grow shallowly ($\zeta_{upr_{max}} = 0.15\ m$) and slowly into the riverbed. With $\sigma_r = 0.0001$ starting from $\zeta_{upr_i} = 0.01\ m$, roots could reach 1 m depth at infinity ($\approx$ 4500 growth-flood cycles). Then, the set of simulations (C) is chosen for which there are intermediate values of the maximum depth ($\zeta_{upr_{max}} = 1.2\ m$) and of σ_r. With $\sigma_r = 0.002$, starting from $\zeta_{upr_i} = 0.01\ m$, roots reach 1 m depth after $\approx$ 200 growth-flood cycles.
(ii) Second, for each set (A), (B), (C), 1000 simulations are performed modifying the range of the flood intensity q from 0 to 20 m^2/s. q=20 m^2/s corresponds to a flood event with a return period of approximately 2-10 years ($\theta \approx 0.3$). For each flood intensity q, the magnitude of the erosion process is quantified by the erosion potential E_p **(Caponi and Siviglia, 2018)** to define a proxy for the magnitude of the hydro-morphodynamic disturbance. E_p is calculated as the value of the erosion after the first growth-flood cycle with vegetation at carrying capacity.
(iii) Third, for each set (A), (B), (C), and for each value of the flood intensity q, 1000 simulations are performed with different initial conditions of the root depth $\zeta_{upr,i}$, in a range from 0 to $offset$.

All the other model parameters are equal for each set (A), (B), (C), and are typical values for gravel-bed rivers. They are summarized in Table 3.2.

These sets of simulations are performed to explore two key aspects:

(i) the relation between root depth growth dynamics (proxy of the resistance force) and E_p (proxy of the hydro-morphodynamic disturbance). For each value of the flood intensity q (proxy for external environmental conditions) corresponds a value of Ep.

(ii) the dependence of the system's steady state on the initial condition of the root depth $\zeta_{upr,i}$.

To ensure reaching the steady state solution, 1000 growth-flood cycles are simulated.

Table 3.2: Run parameters.

Parameter	Description	Value and Unit
p	Porosity	0.4
$k_{s,v}$	Minimum Strickler coefficient with vegetation	$8m^{1/3}s^{-1}$
S	Channel slope	0.006
σ	Vegetation growth rate	0.28
d_s	Sediment diameter	6 cm
K	Carrying capacity	1
B_{min}	Initial vegetation biomass	1.0×10^{-5}
T_v	Vegetation growth time scale	1 growing season
$k_{s,g}$	Strickler coefficient of the bare soil	$30\,\mathrm{m}^{1/3}\mathrm{s}^{-1}$
ΔT_F	Time interval between floods	T_v
L_v	Vegetation patch length	300 m
T_F	Flood duration in the 0D model	0.78 h
β	Shape parameter for the uprooting	1.0
w_m	minimum fraction of ζ_{upr} required for uprooting	0.27
q_B	Unit width sediment flux	m^2s^{-1}

3.2.2 Results

Model results show that for the set of simulations (A), the system always reaches the steady state in the vegetated state (Figure 3.5A). In fact, when roots grow rapidly (high value of σ_r) and deeply into the riverbed (high value of *offset*), roots resistance (proxy ζ_{upr}) is significantly greater than any value of the hydro-morphodynamic disturbance (proxy E_p, range from 0 to 0.54 m). Thus, for every value of the flood intensity q and for every initial condition $\zeta_{upr,i}$, root depth grows and reaches over time the maximum value (ζ_{upr}=2.7 m). At steady state, if the maximum root depth reaches its maximum, the vegetation B achieves the carrying capacity K, i.e., the ecological phase.
For the set of simulations (B), the system always reaches the steady state in bare soil, except when there is no solid transport (for $q \leq 2.4\ m^2/s,\ \theta < \theta_{cr}$), and thus, no uprooting mechanism. In fact, without uprooting, the system always reaches over time the vegetated state, (Figure 3.5B), as there is no hydro-morphodynamic disturbance. When solid transport occurs ($q > 2.4\ m^2/s$) and roots grow slowly (low value of σ_r) and shallowly into the riverbed (low value of *offset*), roots resistance (proxy ζ_{upr}) is significantly smaller than any value of the hydro-morphodynamic disturbance (proxy E_p). Thus, for every value of the flood intensity q and for every initial condition of the root depth $\zeta_{upr,i}$, both vegetation B and root depth ζ_{upr} go over time to bare soil ($\zeta_{upr} = 0$ and $B = B_{min}$).
For the set of simulations (C) the system shows bi-stability between $2.4\ m^2/s \leq q \leq 12.1\ m^2/s$ ($\approx\ 0.08\ m \leq E_p \leq 0.3\ m$) and the steady state depends on the initial condition of the root depth $\zeta_{upr,i}$, (Figure 3.5C). If the initial condition (e.g. $\zeta_{upr,1}$) is above the unstable equilibrium (red line in Figure 3.5C), the system reaches the vegetated state over time because the initial condition is deep enough and its growth is rapid enough to be stronger than the hydro-morphodynamic disturbance (proxy E_p). If the initial condition (e.g. $\zeta_{upr,2}$) is below the unstable equilibrium, the system goes to bare soil over time because the initial condition is not-deep enough into the riverbed and its growth is not rapid

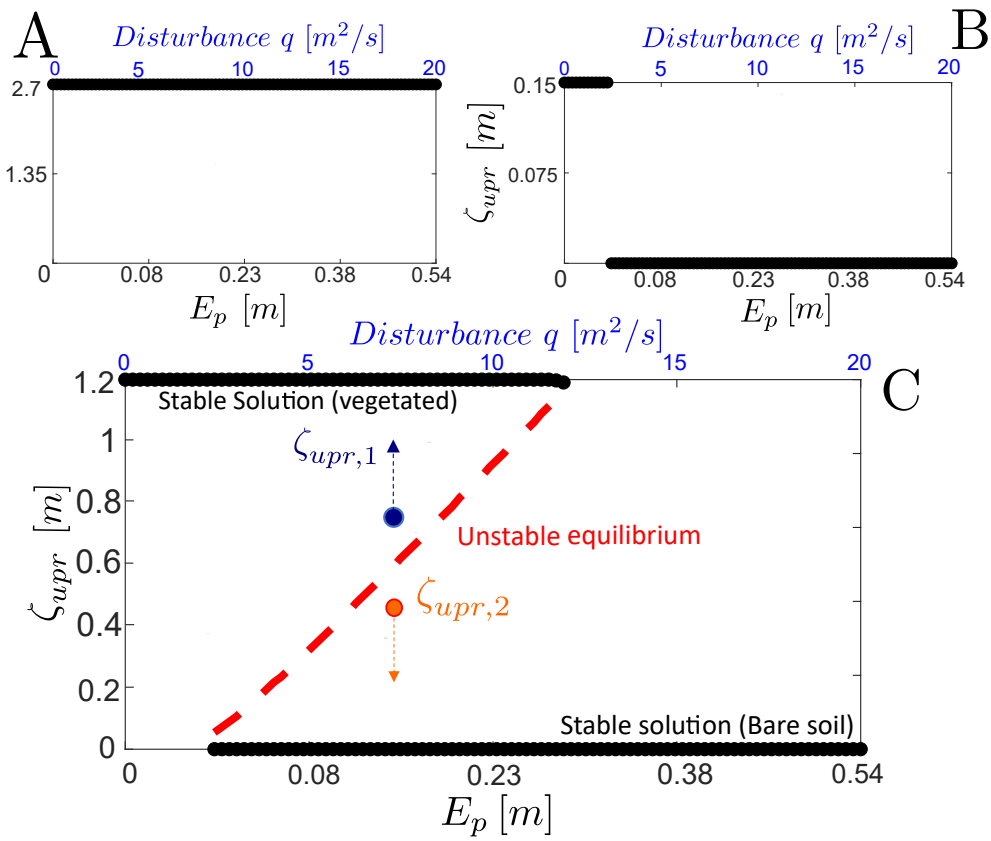

Figure 3.5: (A) When roots grow rapidly (high value of σ_r) and deeply into the riverbed (high value of *offset*) the system always reaches the vegetated state. (B) When roots grow slowly (low value of σ_r) and shallowly into the riverbed (low value of *offset*) the system always reaches the bare soil (except when there is no solid transport and thus no uprooting mechanism (for $q \leq 2.4\ m^2/s,\ \theta < \theta_{cr}$). (C) For intermediate values of σ_r and *offset*, the system shows bi-stability for $2.4\ m^2/s \leq q \leq 12.1\ m^2/s$ ($\approx 0.08\ m \leq E_p \leq 0.3\ m$) and the steady state depends on the initial condition of the root depth $\zeta_{upr,i}$. The red line represents the unstable equilibrium of the system. If the initial condition (e.g. $\zeta_{upr,1}$) is above the unstable equilibrium, the system reaches the vegetated state over time. If the initial condition (e.g. $\zeta_{upr,2}$) is below the unstable equilibrium, the system goes to bare soil over time.

enough to be stronger than the hydro-morphodynamic disturbance (proxy E_p). Therefore, in the range between 2.4 $m^2/s \leq q \leq 12.1\ m^2/s$, roots resistance is comparable to the magnitude of the hydro-morphodynamic disturbance and differences in the initial conditions can lead the system to switch between the two alternative states.
For low value of the flood intensity ($q \leq 2.4\ m^2/s$), the system always reaches the vegetated state over time because roots resistance is higher then the hydro-morphodynamic disturbance E_p for every initial condition. On the contrary, for high value of the flood intensity ($q > 12.1\ m^2/s$), the system always goes in bare soil over time because roots resistance is much lower then the hydro-morphodynamic disturbance E_p for every initial condition.

To determine the unstable equilibrium in the set of simulations (C), simulations are performed for each value of the flood intensity q with 1000 different initial conditions of root depth $\zeta_{upr,i}$ ranging from 0 to $offset$.
Indeed in Figure 3.6 results are shown for a set of simulations, corresponding to Figure 3.5C, with constant flood intensity $q = 7.3\ m^2/s$. The trajectories (i.e., solutions) of several initial conditions of the root depth ζ_{upr} are plotted over the dimensionless time t^*. If the initial conditions are above the unstable equilibrium (e.g. $\zeta_{upr,1}$), all the trajectories over time go toward the vegetated state. If the initial conditions are below the unstable equilibrium (e.g. $\zeta_{upr,2}$), all the trajectories go over time to bare soil. In Figure 3.6A several growth-flood cycles are simulated, without discarding any cycle, with the purpose to show the root depth trajectories over time. Instead, in Figure 3.6B the steady state solution of ζ_{upr} is shown as a function of $\zeta_{upr,i}$, discarding the transition cycles. The critical value at which the system switches the basin of attraction is the unstable equilibrium (red line in both Figure 3.6A and 3.6B), as qualitatively explained in Figure 3.1.
From these results, it can be observed how the system undergoes critical shifts and tipping points (e.g., in Figure 3.6B the value of $\zeta_{upr,i} = 0.7$ is a tipping point). It is also important to highlight that small differences in the initial conditions, especially when close to the unstable equilibrium, can significantly affect the final equilibrium of the system.

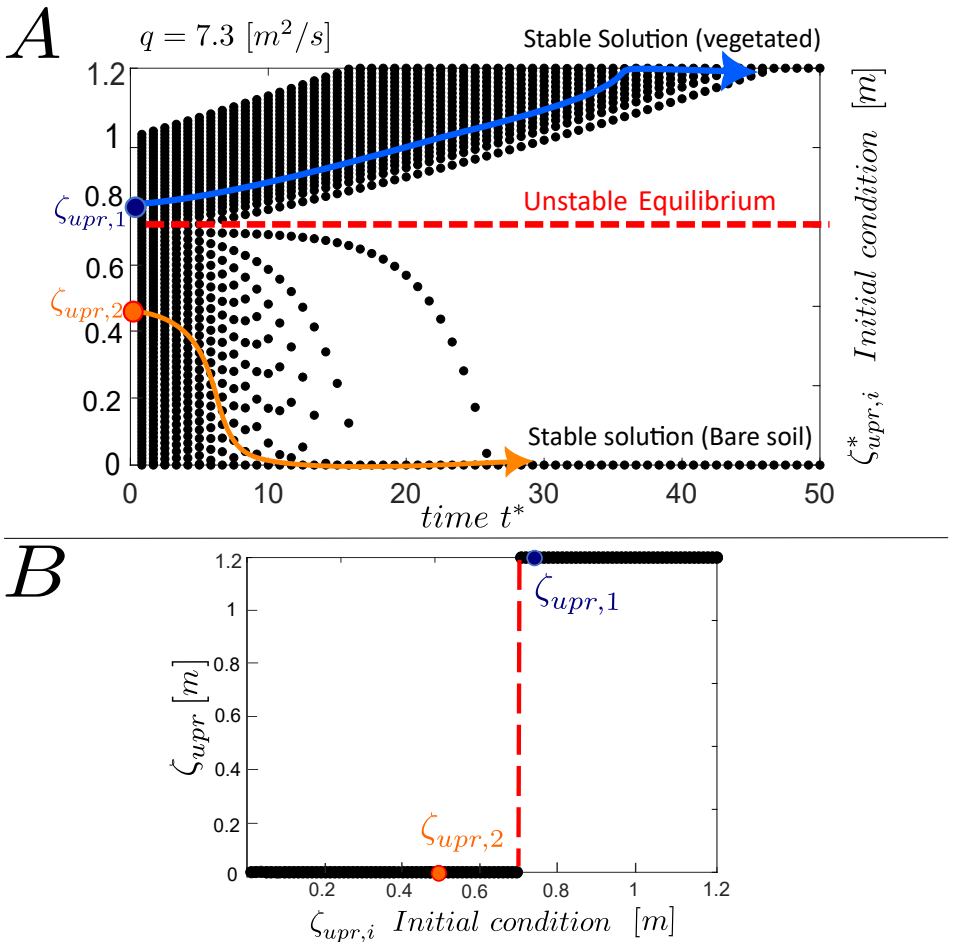

Figure 3.6: Set of simulations corresponding to Figure 3.5C, in the case with constant flood intensity $q = 7.3\ m^2/s$. (A) Trajectories of initial conditions of the root depth ζ_{upr_i} are shown over time t^*. If the initial condition is above the unstable equilibrium (e.g. $\zeta_{upr,1}$) the trajectory over time goes toward the vegetated state. If the initial condition is below the unstable equilibrium (e.g. $\zeta_{upr,2}$) the trajectory over time goes to bare soil. (B) ζ_{upr} is plotted at steady state as a function of the initial condition ζ_{upr_i}. The red line, in both figures, is the unstable equilibrium.

3.3 Multi-stability in a spatial eco-morphodynamic model

3.3.1 Numerical simulations

With the 1D model three sets of simulations (A), (B), (C) are performed by modifying parameters as shown in Figure 3.4 and as illustrated in Table 3.1. Indeed, the setup is similar to the one of the non-spatial model.
For each value of the flood intensity q, the proxy for the hydro-morphodynamic disturbance E_p is calculated as the mean value of erosion after the first growth-flood cycle, within the vegetated area with biomass at carrying capacity. For each value of q, $E_{p,max}$ is also calculated, which is the maximum local erosion reached after the first growth-flood cycle within the vegetated area with biomass at carrying capacity.
All the other model parameters are chosen as typical values for gravel-bed rivers and they are the same as those used in the 0D model (refer to Table 3.2), except for flood duration which is $T_F(1D) = 3\ h$ in the 1D model (and $T_F = 0.78\ h$ in the 0D model). The flood duration is calibrated such that $T_F(0D)/T_F(1D) = 0.26$ to establish morphodynamic equivalence between the 1D model and the 0D model, ensuring that the average erosion in the 1D model matches the erosion potential E_p in the 0D model, as explained in Appendix (A.3).
These sets of simulations are performed to explore how the spatial heterogeneity modifies these two key aspects:

(i) the relation between root depth growth dynamics (proxy of the resistance force) and E_p (proxy of the hydro-morphodynamic disturbance). For each value of the flood intensity q (proxy for external environmental conditions), corresponds a value of Ep.

(ii) the dependence of the system's steady state on the initial condition of root depth $\zeta_{upr,i}$.

To ensure reaching the steady state solution, 500 growth-flood cycles are simulated. Compared to the 0D model, the growth-flood cycles have been reduced here due to the significantly longer computational time required. However, with the chosen parameters, the system always reaches the steady state before 500 growth-flood cycles.

3.3.2 Results

Multi-stability graph

Model results show that for the sets of simulations (A) and (B), (respectively Figure 3.7A and 3.7B), the behavior is similar to the one described for the corresponding sets of the 0D model (Figure 3.5A and 3.5B).
Instead, for the set of simulations (C) the system shows a more complex multi-stable behavior (Figure 3.7C). The multiple states encompass the entire area of the Figure 3.7C where the black dots can be observed. In fact, as illustrated in Figure 3.8 ($A - C - E$), if the initial conditions of root depth $\zeta_{upr,i}$ (green points) are within the domain of attraction (green areas), all trajectories eventually converge over time (t_{ss} is the time at steady state)

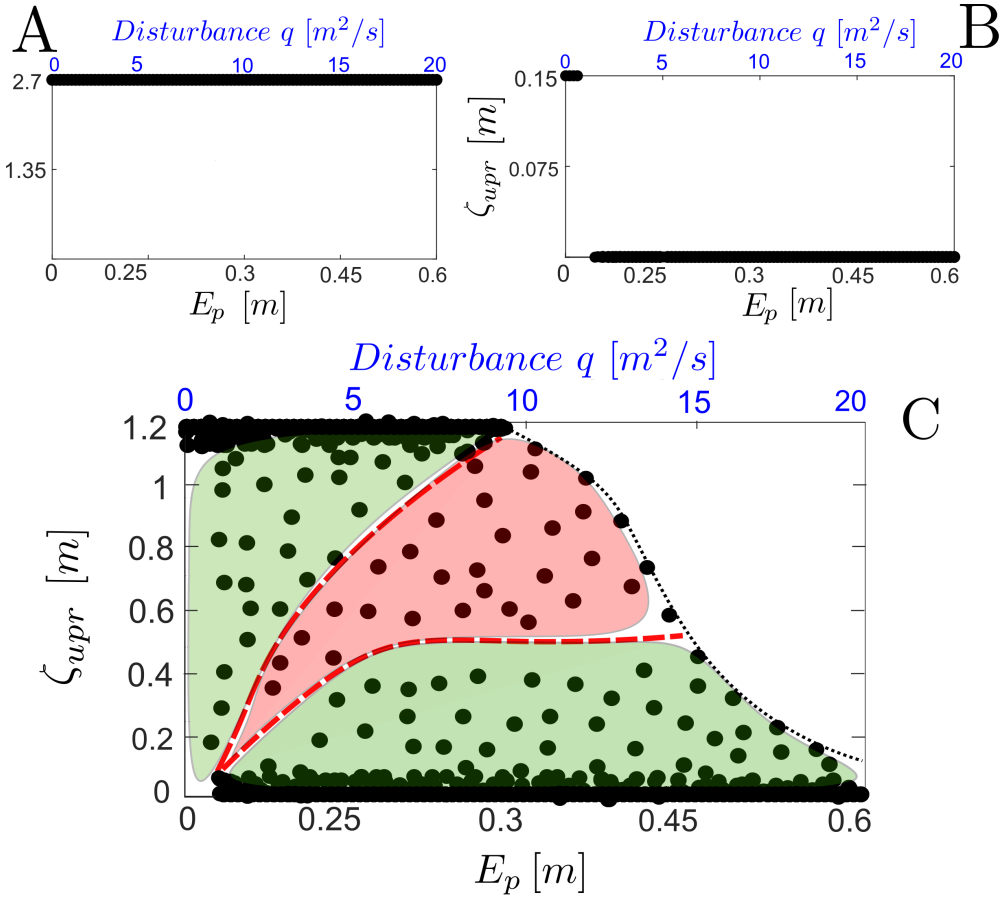

Figure 3.7: (A) When roots grow rapidly (high value of σ_r) and deeply into the riverbed (high value of *offset*), the system always reaches the vegetated state. (B) When roots grow slowly (low value of σ_r) and shallowly into the riverbed (low value of *offset*), the system always reaches the bare soil (except when there is no solid transport, and thus no uprooting mechanism, i.e., for $q \leq 1.0\ m^2/s,\ \theta < \theta_{cr}$). (C) For intermediate values of σ_r and *offset*, the system shows a more complex multi-stable behavior. The red zone represents the multi-stability zone, while the green areas are the domains of attraction of the two homogeneous states (i.e., bare soil and vegetated state). If the initial conditions are inside the domains of attraction, the system reaches the vegetated state or bare soil over time. If the initial conditions are inside the multi-stability zone, the system reaches an equilibrium in between the two alternative states. The black dots represent the equilibrium states.

to one of the two alternative states (vegetated riverbed or bare soil). Conversely, as shown in Figure 3.8 ($B-D-F$), when the initial conditions of root depth (red points) are within the region of multi-stability (red area), all trajectories over time reach different equilibria across the entire area in between the two alternative states.
Thus, if the initial conditions are inside the upper domain of attraction, roots are deep enough and their growth is rapid enough to resist against the hydro-morphodynamic disturbance (proxy E_p) and they go over time to the vegetated state. If the initial conditions

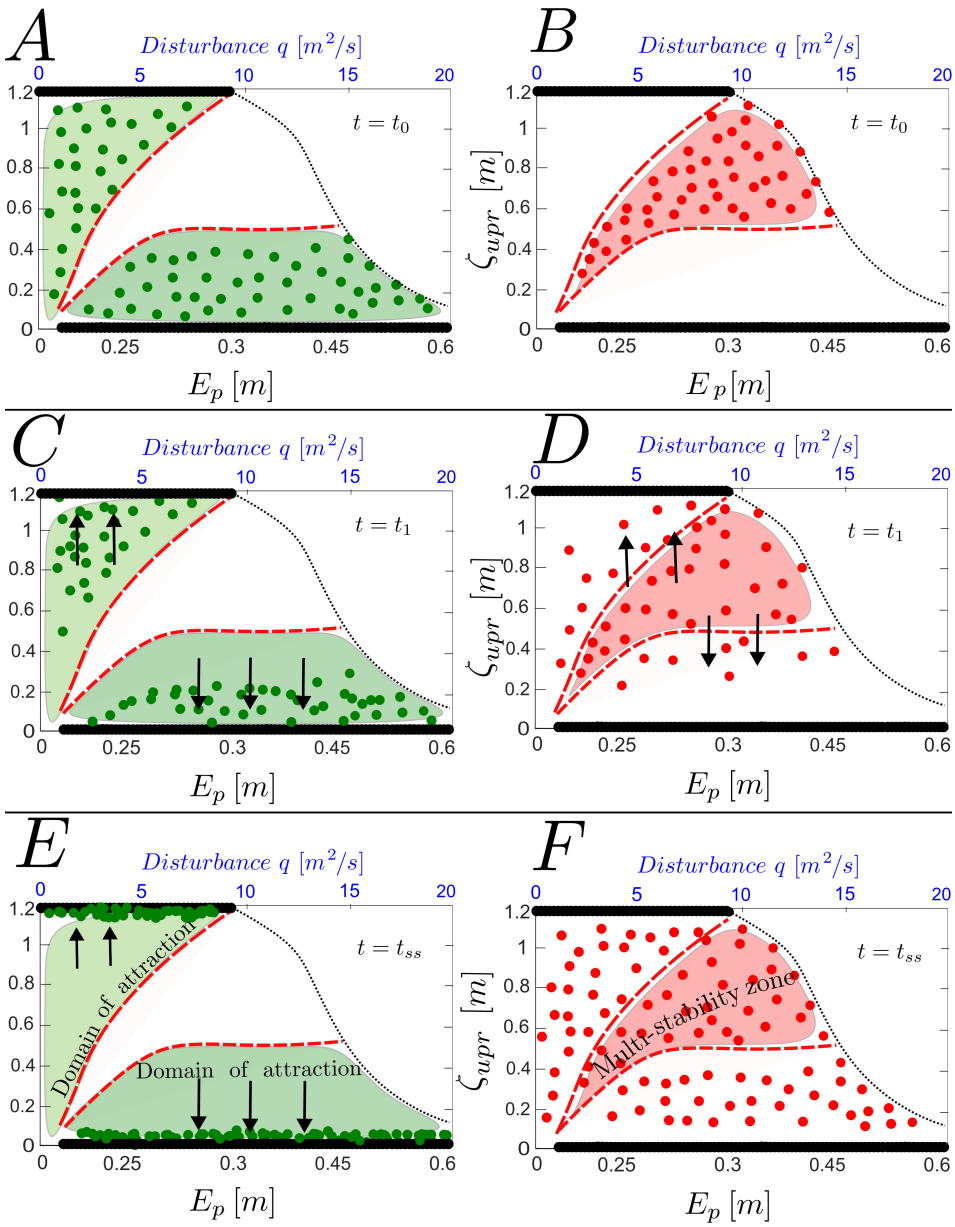

Figure 3.8: Explanation of the multi-stable solution for the spatial model. (A-C-E) If the initial conditions of root depth $\zeta_{upr,i}$ (green points) are within the domain of attraction (green areas), all trajectories eventually converge over time (t_{ss} is the time at steady state) to one of the two alternative states (vegetated riverbed or bare soil). (B-D-F) Conversely, when the initial conditions of root depth (red dots) are within the region of multi-stability (red area), all trajectories over time reach different equilibria across the entire area in between the two alternative states (red dots when $t = t_{ss}$).

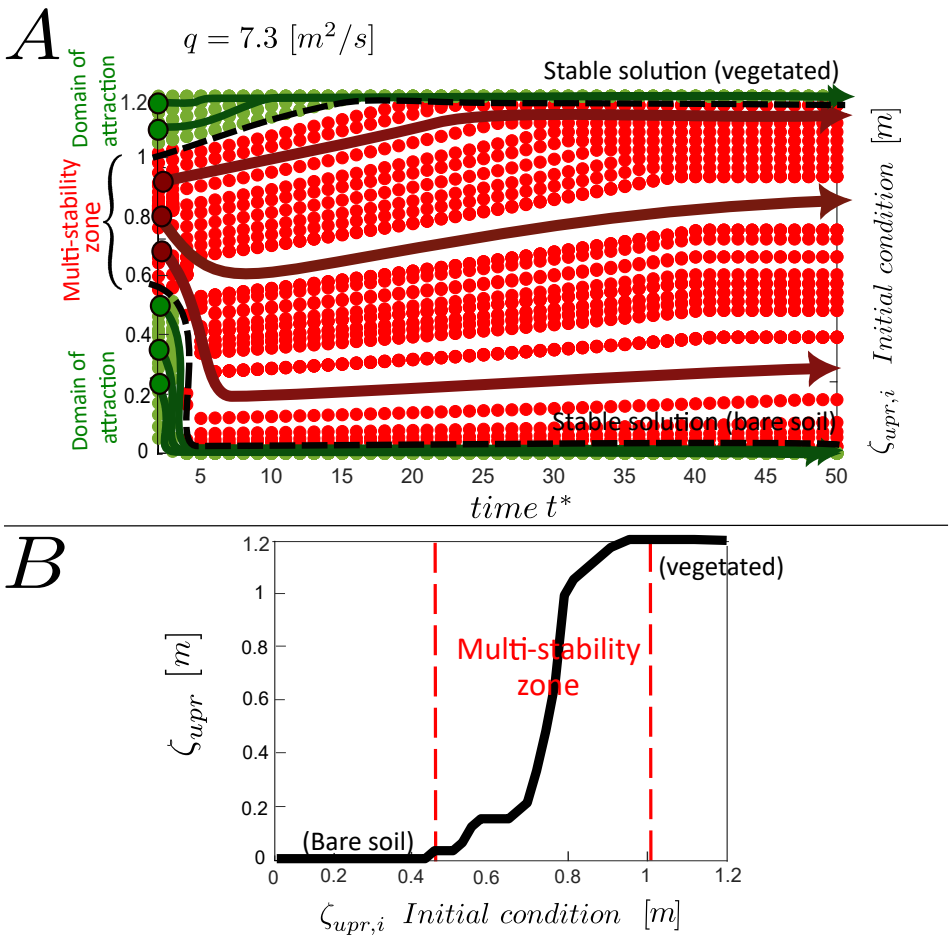

Figure 3.9: Set of simulations corresponding to Figure 3.7C with constant flood intensity $q = 7.3\ m^2/s$. (A) Trajectories of initial conditions of the root depth ζ_{upr} are shown over time t^*. If the initial conditions are inside the domains of attraction ($\zeta_{upr,i} \leq 0.45\ m$ or $\zeta_{upr,i} \geq 1.0\ m$), all the trajectories over time go toward the vegetated state or bare soil. If the initial conditions are inside the multi-stability zone ($0.45\ m < \zeta_{upr,i} < 1\ m$), they reach the steady state solution in between the two alternative stable states. (B) The steady-state solution of ζ_{upr} is shown as a function of the initial condition $\zeta_{upr,i}$, where the two red lines delimit the multi-stability zone.

are inside the lower domain of attraction, roots are too shallow and their growth is not rapid enough to resist against the hydro-morphodynamic disturbance and they go over time to bare soil. However, if the initial conditions are inside the multi-stability zone, the hydro-morphodynamic disturbance is able to uproot only a portion of the vegetated patch, while the other part resists against it and reaches its maximum growth over time. Moreover, in Figure 3.8, one can observe how multi-stability prevents critical shifts and tipping points. Indeed, the 1D system does not show critical transitions as seen in the non-spatial model (Figure 3.5C), but it exhibits a smoother behavior due to spatial interactions.
Figure 3.9 displays results for a set of simulations, corresponding to Figure 3.7C, with

constant flood intensity $q = 7.3\ m^2/s$. In Figure 3.9A, the trajectories of several initial conditions of the root depth ζ_{upr_i} are plotted over the dimensionless time t^*. If the initial conditions are inside the domains of attraction ($\zeta_{upr,i} \leq 0.45\ m$ or $\zeta_{upr,i} \geq 1.0\ m$), all the trajectories over time go toward the vegetated state or bare soil. If the initial conditions are inside the multi-stability zone ($0.45\ m < \zeta_{upr,i} < 1\ m$), the steady state solution is in between the two alternative stable states because the hydro-morphodynamic disturbance is able to uproot only part of the vegetated patch, while the other part of the patch resists against it and reaches its maximum over time.
To define the multi-stability zone, simulations are performed for each value of the flood intensity q with 100 different initial conditions of root depth $\zeta_{upr,i}$, ranging from 0 to $offset$. The range of initial conditions that reaches the equilibrium between the two alternative states defines the multi-stability zone (as shown in Figure 3.9). Figure 3.9B displays the steady state solution of ζ_{upr} as a function of the initial condition $\zeta_{upr,i}$, where the two red lines delimit the multi-stability zone.

In Figure 3.10, it is observed that the line delimiting the upper domain of attraction is

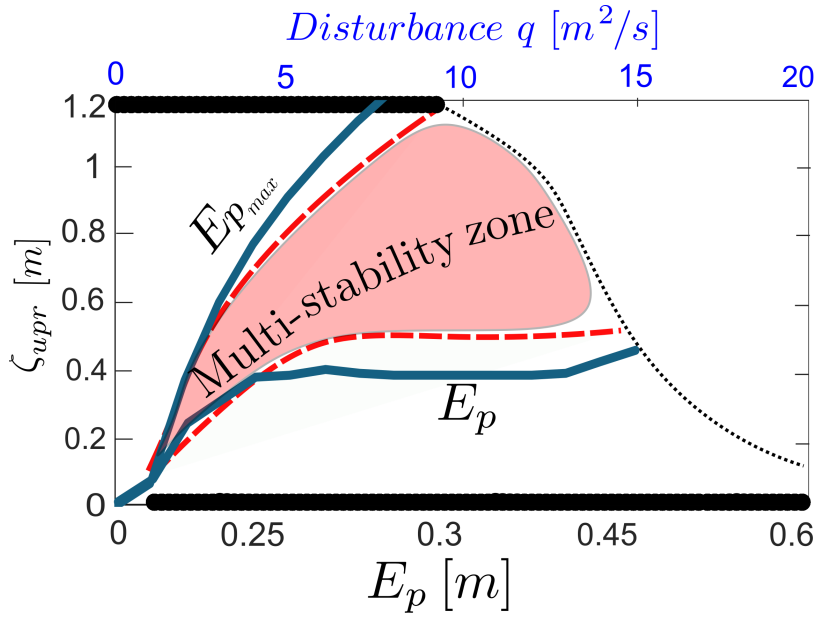

Figure 3.10: Link of the multi-stability graph with the value of the hydro-morphodynamic disturbance. The line delimiting the upper domain of attraction is linked to the value of the maximum local erosion $E_{p,max}$. Conversely, the line delimiting the lower domain of attraction is linked to the value of the average erosion E_p.

linked to the value of $E_{p,max}$. In fact, if the initial conditions of roots are deeper than the maximum point of erosion $E_{p,max}$, no plant is uprooted and all the patch goes to the carrying capacity over time. Conversely, the line delimiting the lower domain of attraction is linked to the value of E_p. In fact, if the average erosion E_p is greater than the initial conditions of roots, the erosion is able to uproot every plant, leading the system to bare soil. The curves of E_p and $E_{p,max}$ are wider than the multi-stability zone because they are calculated with biomass at carrying capacity (and thus at maximum disturbance), whereas

during the simulations the vegetation is not always at carrying capacity (and, therefore, the disturbance is lower).

Spatial interactions

Based on the previous results, it can be observed that multi-stability prevents critical shifts and tipping points, instead smoothing out the system's behavior through spatial interactions. Figure 3.11A, displays the spatial distribution along the x axis for the case with $q = 7.3\ m^2/s$ and $\zeta_{upr,i} = 0.78\ m$, where the initial condition is inside the multi-stability zone. This initial condition with negligible biomass but non-negligible root depth could be representative of (i) a winter season condition, (ii) a canopy damaged by sediment transport, or (iii) juvenile flexible plants that lower into the flow (and therefore with negligible variations in Ks). At steady state, in Figure 3.11B, part of the patch is uprooted, while the remaining part reaches the vegetated state. Also the riverbed and water profile adjust depending on the remaining patch. This capacity of the patch to partially resist and not be completely uprooted for certain values of the disturbance is what makes the system's behavior smooth, avoiding critical shifts and tipping points.

Figure 3.12 illustrates only the spatial distribution of roots, along the x axis, for the case with $q = 7.3\ m^2/s$ and $\zeta_{upr,i} = 0.7\ m$ (brown line), where the initial condition is inside the multi-stability zone. Over time, part of the patch is uprooted, while the remaining part reaches the $offset$ (yellow line). It's important to note that the final average is equal to $\zeta_{upr} = 0.21\ m$, meaning the final solution ends up outside the multi-stability zone, in the lower domain of attraction. Therefore, points with initial conditions inside the multi-stability zone in Figure 3.8 can span the entire area between the two alternative states depending on the value of the final average solution.

Figure 3.13 represents the multi-stable states configuration. The different lengths of the final patch at steady state determine all the intermediate points of multi-stability between the two alternative stable states. Additional simulations are conducted simplifying the 1D model and removing spatial interactions, as detailed in Appendix (A.1) and Appendix (B). The results in the Appendix indicate that the simplified model can only exhibit stability or bi-stability, confirming that spatial interactions are the key element for multi-stability.

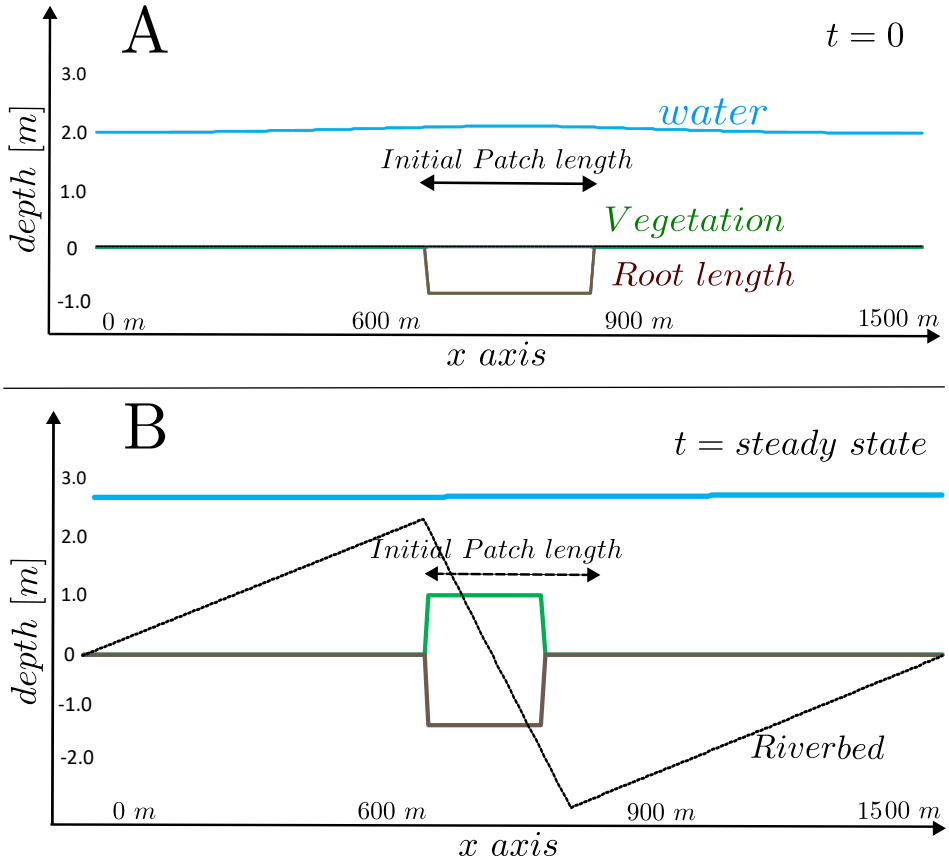

Figure 3.11: (A) Spatial distribution and numerical solution along the x axis for the case with $q = 7.3\ m^2/s$ and $\zeta_{upr,i} = 0.78\ m$, at the initial condition (t=0). (B) At steady state, part of the patch is uprooted, while the remaining part reaches the vegetated state (vegetation reaches the carrying capacity, and roots reach the $offset$).

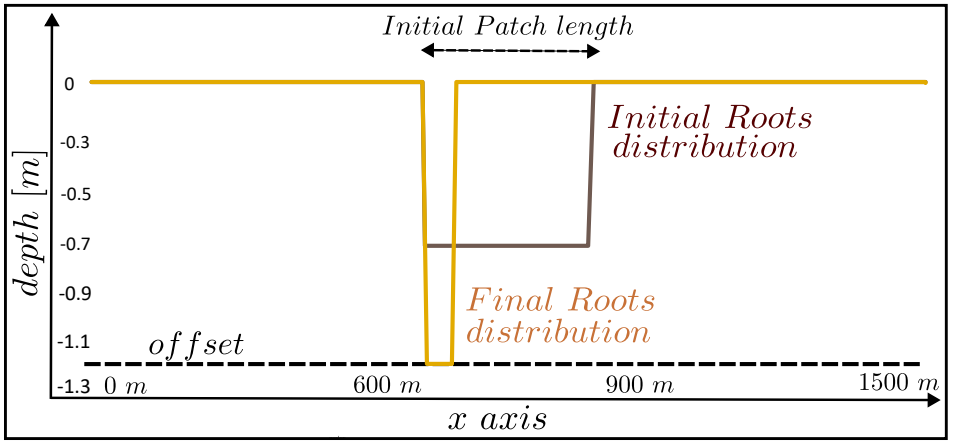

Figure 3.12: Spatial distribution and numerical solution along the x axis for the case with $q = 7.3\ m^2/s$ and $\zeta_{upr,i} = 0.7\ m$ (brown line), the initial condition is inside the multi-stability zone. Over time, part of the patch is uprooted, while the remaining part reaches the $offset$ (yellow line). The final average is equal to $\zeta_{upr} = 0.21\ m$.

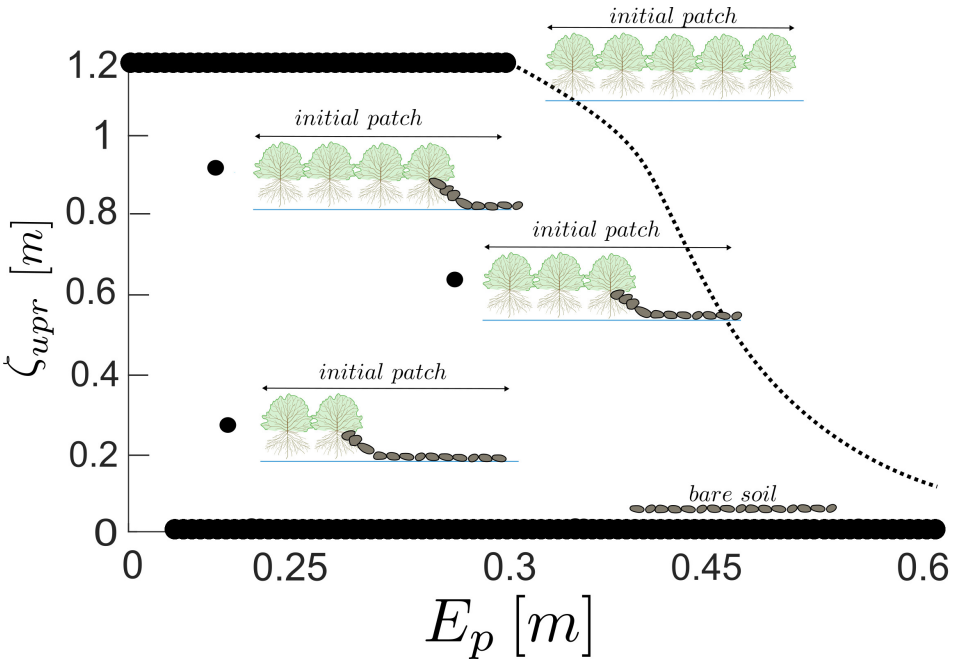

Figure 3.13: Multiple stable states configuration due to spatial interactions. The different lengths of the final patch at steady state determine all the intermediate points of multi-stability between the two alternative stable states.

3.4 Conclusion and implications

In this chapter, the established objectives are achieved:

(i) In the non-spatial model, hysteresis is observed, and the driving parameters of the process are related to the root growth (σ_r and *offset*). The process is more generally driven by the ratio between the resistance force (proxy ζ_{upr}) and the hydro-morphodynamic disturbance force (proxy E_p).

(ii) In the 1D model, spatial interactions modify the equilibrium graph of the ecosystem from bi-stability to multi-stability. Moreover, the spatial distribution of vegetation appears to smooth critical transitions and tipping points. Thus, the simplified ecosystem can persist and find equilibrium in infinite states between the two alternative states, not only within them. The transition between the two alternative states is gradual and the resilience increases compared to the non-spatial model.

In all the results of this chapter, the root growth parameter values (σ_r and *offset*) inhibit the negative feedback loop, promoting positive effects that push the ecosystem towards alternative stable states (refer to Figure 1.3), namely vegetated state or bare soil, or both simultaneously (hysteresis).
Mathematically, in the non-spatial model, when the resistance force prevails over the hydro-morphodynamic disturbance force, the system is pushed over time toward the equations (2.14a) and (2.15a), i.e., vegetated state. On the contrary, the system is pushed over time toward the equations (2.14c) and (2.15c), i.e., bare soil. When the two forces are comparable, the system can be pushed towards either state (a, c) depending on the initial condition, i.e., hysteresis.
In the spatial model, the behavior is similar to the 0D model, as shown in the Appendix (A). Thus, when the resistance force prevails over the hydro-morphodynamic disturbance force, also the 1D system is pushed toward the vegetated state, and, on the contrary, to bare soil. However, if the two forces are comparable (multi-stability zone), only a portion of the vegetated patch is uprooted and turns into bare soil, while the remaining part persists, reaching over time the vegetated state.
These results demonstrate that the final equilibrium of the non-spatial model can exhibit hysteresis, as in the theoretical graph proposed by **Scheffer et al.** (**2001**). Moreover, results of the 0D model show tipping points and instantaneous shifts between stable states (Figure 3.5C and Figure 3.6). Subsequently, it can be observed how this behavior becomes more complex and multi-stable in the 1D model (refer to Figure 3.7C and Figure 3.9).
The 1D model shows how spatial interactions smooth critical transitions and tipping points. Indeed, the system avoids abrupt shifts and self-organizes into multi-stable states. Transitions between alternative states are gradual, showing smaller intermediate steps (refer to Figure 3.7C). This is due to the spatial distribution of vegetation which can persist after being subjected to the hydro-morphodynamic disturbance, increasing the resilience of the system.
These results are conceptually in line with recent works on spatial ecosystems **(Rietkerk et al., 2004, 2021; Bastiaansen et al., 2022)**. Surprisingly, despite the significant differences between the simplified ecosystem and the savanna-forest ecosystem studied by **Rietkerk et al. (2021)**, both systems exhibit similar static behavior. In Figure 3.14A, **Ri-**

etkerk et al. show coexistence of stable states between the forest and savanna alternative states. Also in the results of this chapter, this coexistence between bare soil and vegetation is evident, Figure 3.14B. In both ecosystems, spatial interactions smooth out tipping points and critical transitions and the final equilibrium depends on both the intensity of disturbance and the initial conditions of the vegetation.
These results could suggest that even very different ecosystems can demonstrate similarities in their static behavior and thus, a general common behavior may exist.

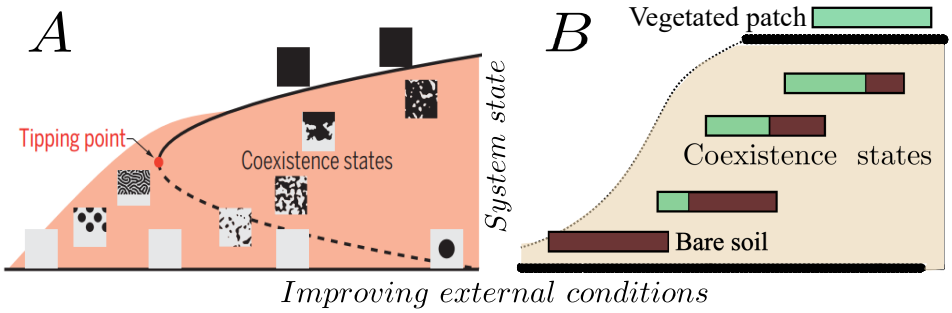

Figure 3.14: (A) The static behavior of the savanna-forest ecosystem by **Rietkerk et al. (2021)** compared to (B) the results of the simplified river ecosystem. Both systems exhibit multi-stability and smoothed behavior.

One of the main implications of these results is that real river ecosystems can be more resilient than previously thought, due to the ability of system to self-organize and persist despite of the external disturbance. However, this does not change the basic concept behind the tipping points theory: the system still exhibits critical states and nonlinear shifts, but the behavior is more smoothed due to spatial heterogeneity.
These results (refer to Figure 3.8) can help quantify the spatial resilience of the river ecosystem. Understanding the equilibrium graph of the river ecosystem can be crucial for developing efficient tools that can contribute to a better understanding of river dynamics and to improving river management. Indeed, to manage the ecosystem, one can act on both the x-axis (hydro-morphodynamic disturbance) or on the y-axis (resistance force). It is essential to have a good understanding of the equilibrium graph of the spatial ecosystem to achieve the desired outcomes in river management. Quantifying resilience can also help communicate effectively with politicians and stakeholders to make informed decisions for the preservation of ecosystems.

3.4.1 Limitations of the analysis

One of the main limitations of the current research lies in the complexity of connecting these models with real ecosystems. Moreover, hysteresis and multiple states are difficult to detect in real river ecosystems. In fact, in real river ecosystems, the interactions among different elements are much more complex compared to the fundamental feedbacks studied in these models, and there are many other components (such as stochastic disturbance, 2D spatial distribution, colonization by vegetation, etc.) that complicate the analysis. In the literature, there are only a few laboratory experiments **(Wang et al., 2016)**, and there have been no field studies so far.

Furthermore, due to the emergence property, the equilibrium graph of the 2D spatial ecosystem is expected to be more complex than the graph found in the 1D model. In fact, the 2D spatial river ecosystem tends to self-organize into patterns (e.g., morphological bars), and the direction and intensity of negative/positive feedbacks can vary at each point in space. However, the equilibrium graph of the 1D model (Figure 3.7C) may be useful as a conceptual basis for the more complex 2D model graph, just as the 0D graph was useful for deriving the 1D graph. Additionally, it is expected that the concept of increased resilience and smoothed critical transitions also holds true in a 2D system.

For this reason, future research could first focus on calibrating and parameterizing the models. Secondly, it is suggested to focus on laboratory or real-world data analysis (especially considering the current increase in available data) to investigate the presence of alternative and multiple states in real river ecosystems. Thirdly, it is suggested to also focus on investigating the 2D equilibrium graph with numerical models.

3.5 Beyond static equilibrium: Oscillations and dynamic equilibrium

In this chapter, the static equilibrium of the simplified river ecosystem is analyzed, namely when root growth dynamics inhibit the negative feedback loop (refer to Figure 2.6). However, when the negative feedback loop prevails, it is found that the system oscillates without reaching a steady state, but rather maintains a dynamic equilibrium, as shown in the Figure 3.15.

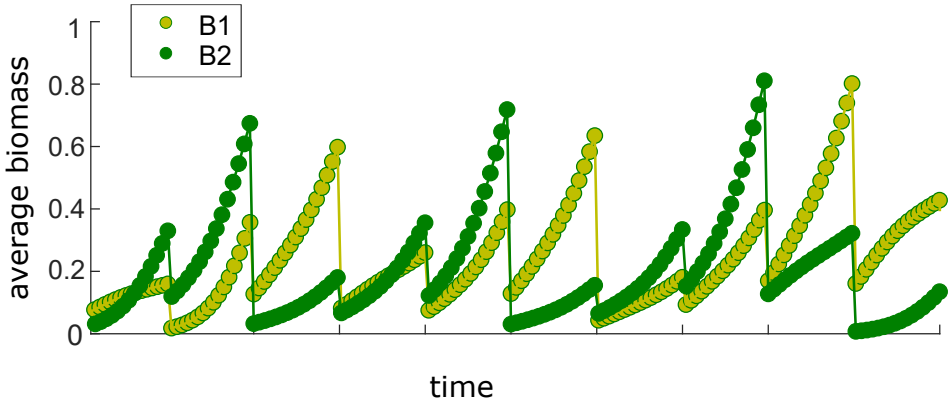

Figure 3.15: When the negative feedback loop prevails, the simplified river ecosystem does not reach a static equilibrium, but rather oscillates dynamically. Moreover, for some parameters, the system exhibits a strong dependence on initial conditions, meaning small variations ($\approx 10^{-5}$) of initial conditions (vegetation $B1$, vegetation $B2$) diverge over time.

Furthermore, it was observed that for some parameters, these oscillations are aperiodic and exhibit a strong dependence on initial conditions. As shown in Figure 3.15, if the

initial condition of the vegetation $B1$ is changed by a small quantity ($|B1 - B2| \approx 10^{-5}$) the numerical solutions diverge over time. This is the commonly called "Butterfly Effect" **(Lorenz, 1972)**, Figure 3.16.

Figure 3.16: The strong dependence on initial conditions is commonly known as "the Butterfly Effect".

In the next chapter, the dynamic equilibrium of the simplified river ecosystem will be studied, and the nature of the observed aperiodic oscillations will be investigated.

Dynamic equilibrium and Chaos

Chapter 4

Oscillations and chaos

4.1 Introduction: Chaotic systems and predictability

At the beginning of the 20th century, the mathematician Poincaré realized that, for some nonlinear deterministic systems, small differences in present observations may be amplified over time, producing significant differences in future conditions—the so-called "Butterfly Effect" **(Lorenz, 1972)**.

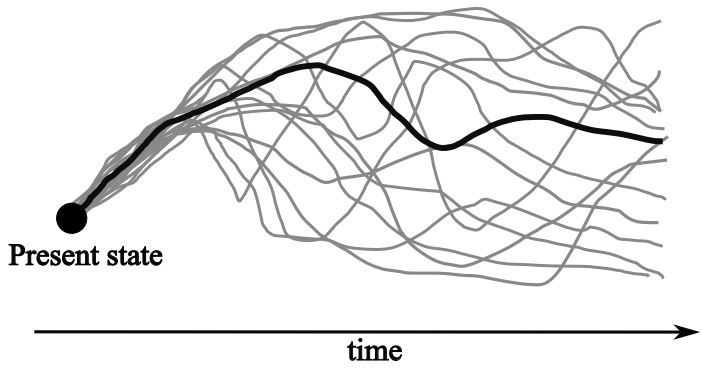

Figure 4.1: In chaotic systems, even a slight alteration of the initial conditions leads to an exponential divergence of the trajectories over time. The black trajectory is the one that is realized, the gray ones are the trajectories that would occur by changing slightly the initial condition **(Slingo and Palmer, 2011)**.

These nonlinear deterministic systems, strongly sensitive to initial conditions, are defined as chaotic systems. According to Laplace's deterministic concept, if the present state of a system is known perfectly, then its future condition could be perfectly known as well **(Van Kampen, 1991)**. However, due to limitations in numerical representation and inevitable measurement errors in physical quantities, the initial conditions of a system can never be known perfectly, but only approximately **(Stone, 1989)**.

Thus, even though chaotic systems are deterministic, dependence on initial conditions and the limitations in their quantification, constrain the predictability. Regardless of how close the initial conditions are, their trajectories will diverge exponentially, impacting the quality of predictions (as shown in Figure 4.1).
Even though chaos limits the long-term predictability, it should not be seen only as a limitation. The amplification of small fluctuations can provide natural systems with access to renewal and novelty **(Crutchfield et al., 1986)**, increasing dynamics, enhancing adaptability and reinforcing the system against the external disturbance.
Moreover, chaotic systems are not synonymous of randomness **(Stone, 1989)**. Their trajectories diverge but remain confined to a well-defined region of the phase space, the attractor. Chaos denies the long-term predictability of the system, but it can also establish the constructive limits of its short-term predictability. In fact, the estimation of the Maximum Lyapunov Exponent (λ) provides a method to quantify the time scale of predictability.
The predictability scale of the system strongly depends on the system itself and can range from seconds, as in the double pendulum **(Shinbrot et al., 1992)**, to million years, as in the case of planets **(Sussman and Wisdom, 1992)**. Chaotic behavior has been found in several models of natural phenomena such as the atmosphere **(Lorenz, 1963)**, (Figure 4.2), forest ecosystem disturbed by fire **(Reluga, 2004)** and in the human heartbeat **(Goldberger, 1991)**.

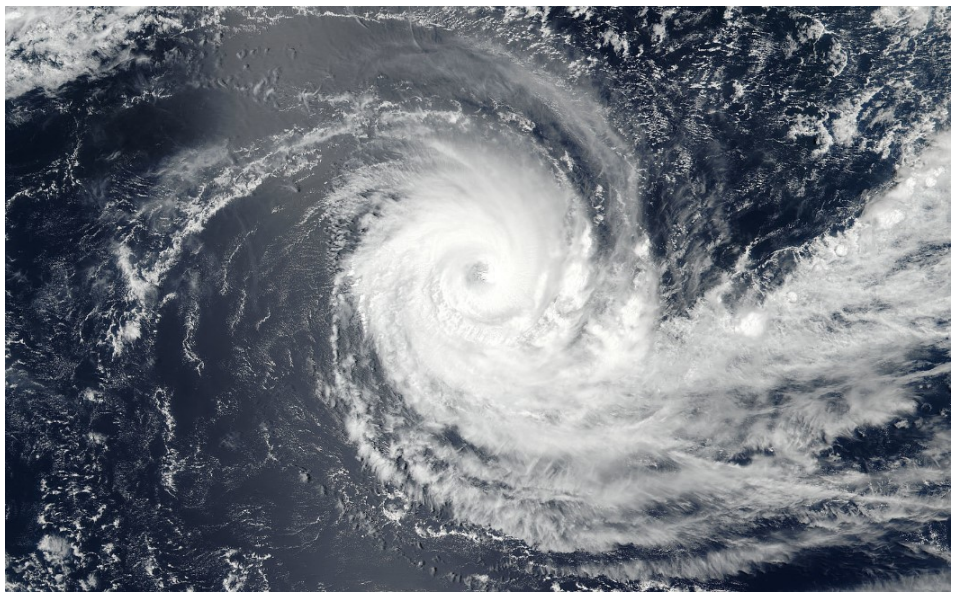

Figure 4.2: The atmosphere is an example of a chaotic system in nature. Photo taken by NOAA/NASA Goddard Rapid Response Team, 2018.

Chaos and complex behavior has also been recently investigated in geomorphological numerical models, such as in braided rivers **(Stecca et al., 2017)**, in delta networks **(Salter et al., 2020)**, and in fractal basins by **Rinaldo** (**2005**).
However, the chaotic behavior in numerical eco-morphodynamic models at the reach scale

has not yet been specifically investigated.
Understanding when ecosystems lose their equilibrium and when they exhibit oscillations or chaotic behavior is of fundamental importance for developing efficient tools that can contribute to a better understanding of river dynamics and to improving predictions of river trajectories. For example, in chaotic systems, probabilistic approaches can be used for forecasting, as already well known by the weather prediction community **(Slingo and Palmer, 2011)**.

Thus, in this chapter, the dynamics of the simplified ecosystem are investigated, namely how the system transitions from a state of stable equilibrium to an oscillatory state. It is important to emphasize that when the system does not reach a steady state, it is because the negative feedback loop is not inhibited by root growth dynamics. Vegetation grows (Figure 4.3A) and increases the roughness, resulting in reduced flow velocity within the vegetated area (Figure 4.3B). Vegetation reduces sediment transport, leading to a greater imbalance between the vegetated and bare areas and thus inducing erosion (Figure 4.3C). Erosion increases the likelihood of vegetation uprooting, and when scour reaches root depth, uprooting occurs (Figure 4.3D). The overall feedback loop is negative: higher vegetation biomass causes greater sediment flux imbalance and more erosion, ultimately resulting in less vegetation.

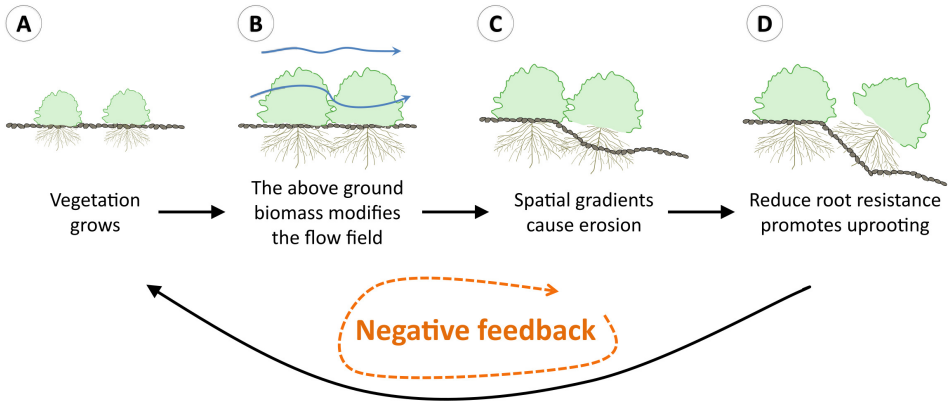

Figure 4.3: Schematic representation of the biogeomorphic negative feedback loop. Vegetation grows (A) and increases the roughness, resulting in reduced flow velocity within the vegetated area (B). Vegetation reduces sediment transport, leading to a greater imbalance between the vegetated and bare areas and thus inducing erosion (C). Erosion increases the likelihood of vegetation uprooting, and when scour reaches root depth, uprooting occurs (D). The overall feedback loop is negative: higher vegetation biomass causes greater sediment flux imbalance and more erosion, ultimately resulting in less vegetation. Vegetation regrows during low-flow periods, maintaining the negative feedback cycle

Moreover, to simplify the system analysis, an additional assumption is made, namely that the root depth ζ_{upr} is constant and equal to the maximum value $offset$. This results in a 3-variables system instead of 4, which is simpler to treat mathematically and numerically. It was decided to keep the root depth constant because simulations showed that this parameter strongly influences the system's dynamics, and this simplification was necessary to have full control of the analysis. Additionally, roots physically grow quickly in the early

stages of the plant's life and then remain rather constant over time.
The main objectives of this chapter are defined as follows:

(i) Investigating the presence of chaotic oscillations in the models and defining the route to chaos, attractors, fractals, and the main driving parameters of the process.

(ii) Quantifying the scale of predictability, namely the Lyapunov time of the simplified river ecosystem.

The method involves stability analysis of the 0D model and numerical simulations with both the non-spatial and spatial model described in Chapter 2.

Before presenting the analysis and results, a brief description of the concepts of the route to chaos, fractals, and attractors is provided here.

4.1.1 Route to chaos: From stability to instability

The system can transition from a stable state to aperiodic oscillations (i.e., chaos) through several "routes to chaos", by modifying driving parameters. Understanding the route to chaos is crucial to comprehend how the dynamical system evolves from a stable region to a chaotic-unstable region and to understand how sensitive the shift is to parameters. As shown in Figure 4.4, there are several routes to chaos, such as intermittency (left), period doubling (center), and Neimark-Sacker bifurcation (right).
In the period doubling route to chaos, the system transitions from stability to chaos through periodic oscillations, losing stability and doubling its period until reaching chaos, as shown in Figure 4.4 (center). However, within the chaotic regions, "periodic windows" may emerge, exhibiting brief episodes of order and periodic behavior.

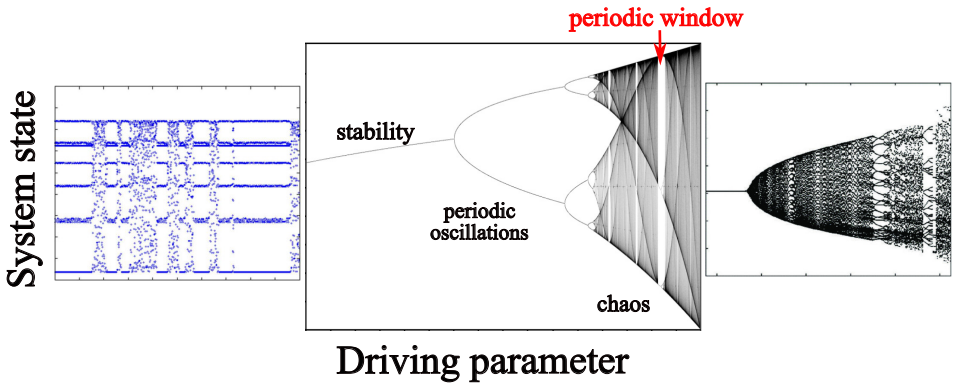

Figure 4.4: The system can transition from a stable state to a chaos through several routes to chaos, such as intermittency (left), period doubling (center), and Neimark-Sacker bifurcation (right). Adapted from **Gritli et al.** (**2012**), **Wikimedia Commons**, **Zhang et al.** (**2018**).

The bifurcation points of period doubling can be identified through the stability analysis and the Cobweb maps of the system. Cobweb maps are a graphical method used to

iteratively represent a map and to investigate its dynamic behavior **(Strogatz, 2018)**.

4.1.2 Fractals and attractors

How can chaotic trajectories diverge exponentially and still remain confined to a well-defined region of the phase space, the attractor? This paradox is explained by the concept of fractals and the mechanism of stretching and folding.
In 1963 Lorenz was simulating the behavior of a model of convection in the atmosphere. Surprisingly, though the solution exhibited divergent outcomes with slight changes in the initial conditions (i.e., chaos), Lorenz noted that the structure was order and enclosed in a specific region of space, but creating a "infinite complex of surfaces" **(Lorenz, 1963)** namely a "strange attractor" with a fractal structure **(Strogatz, 2018)**.

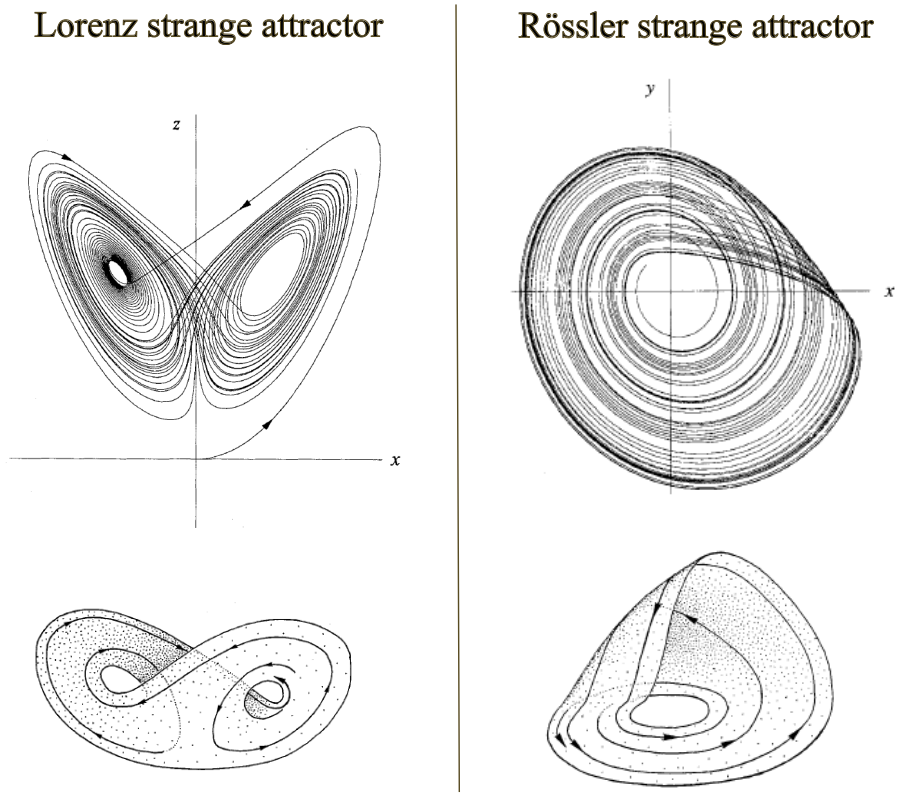

Figure 4.5: Two examples of strange attractors for chaotic solutions, the Lorenz attractor (1963) on the left and the Rössler attractor (1976) on the right. The axes x, z, and x, y represent selected variables of the two dynamical systems, respectively, and the trajectories (black lines) are their solutions over time. Adapted from **Strogatz** (**2018**).

Trajectories are obtained by plotting a graph with system variables numbered m as axes (i.e., phase space with m dimensions) and tracing the mathematical solution of the dynamical system over time.

Two well-known examples of strange attractors include the already mentioned Lorenz attractor and the Rössler attractor, shown in Figure 4.5. The chaotic trajectories of these strange attractors are confined to a specific bounded region but they also diverge exponentially. They exist in a finite space but they give rise to an infinite structure that repeats itself, a fractal. This is explained by the mechanisms of stretching and folding. The system stretches the trajectories in the phase space, causing them to diverge. However, it then folds them, bringing them back into the confined region. This process is repeated cyclically over time **(Strogatz, 2018)**.
Fractals are geometric objects with precise properties:
(i) symmetry and self-similarity, namely they repeat the same shape on smaller scales,
(ii) structure at arbitrary small scales
(iii) a not integer dimension.
A well-known example of a fractal is the Mandelbrot set **(Mandelbrot, 1982)**, given by a very simple equation:

$$z_{n+1} = z_n^2 + c \tag{4.1}$$

where z is the variable of the system, n is the number of iterations and c is a parameter with a real and an imaginary part (complex number). Starting from this equation a highly complex order structure is obtained, as shown in Figure 4.6. The x and y axes of the area represent different values of the parameter c of equation (4.1), respectively the real and imaginary parts. To define when the solution is chaotic or stable, it is necessary to calculate the Maximum Lyapunov Exponent λ (MLE). The inner part of the Mandelbrot set (black in Figure 4.6) represents the stable solution (negative value of the MLE) of the system, while the outer part (blue in Figure 4.6) is the chaotic solution (positive value of the MLE). If one zooms in on Figure 4.6, it becomes apparent that it repeats itself infinitely (zoom in on the red area).

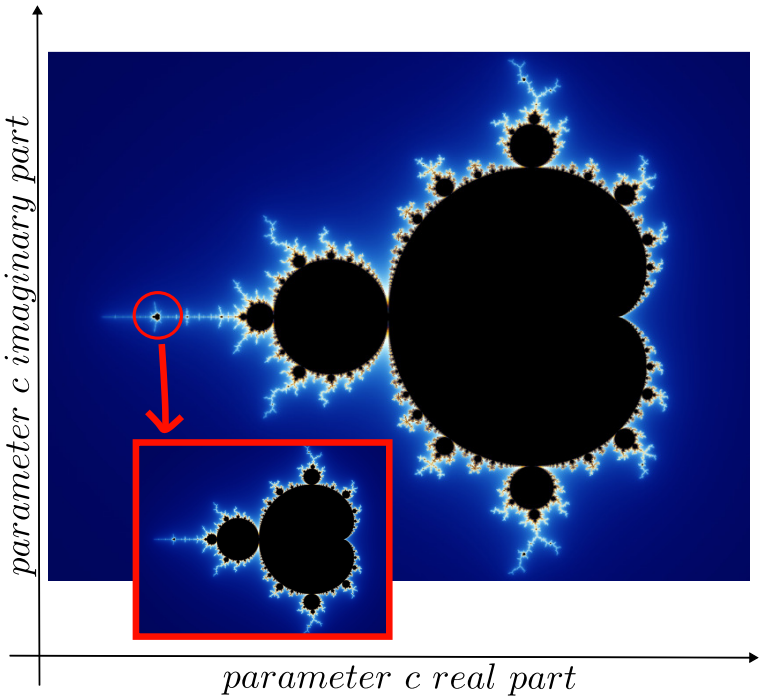

Figure 4.6: Example of chaotic fractal solution, the Mandelbrot set **(Mandelbrot, 1982)**. The x and y axes of the area represent different values of the parameter c of equation (4.1), respectively the real and imaginary parts. The stable solution is the black part of the Figure, the unstable chaotic solution is represented by the blue color. If one zooms in on the figure, it becomes apparent that it repeats itself infinitely (zoom in on the red area). Adapted from **Wikimedia Commons**.

4.2 Oscillations and chaos in the 0D model

In this section, the 0D model is used to:

(i) conduct a stability analysis of the system and to draw the Cobweb maps to define the route to chaos of the system.

(ii) estimate the Maximum Lyapunov exponent (λ) to define the time scale of predictability for several parameter configurations through numerical simulations (details shown in Subsection 4.2.1).

(iii) investigate the fractal structure of the system through numerical simulations.

The stability analysis and fractal solutions are exclusive to the 0D model due to (i) its analytical tractability and (ii) significantly lower computational time requirements compared to the 1D model. Nevertheless, in Appendix (A), it is demonstrated how the dynamic behavior of the 0D model is comparable to that of the 1D model, indicating that the common biogeomorphic feedbacks and the intrinsic disturbance mechanism are the key ingredients generating the chaotic behavior.

4.2.1 Methodology

Stability analysis and Cobweb maps

To define the nature of the oscillations emerging in the system, a stability analysis is conducted on the 0D model. In this section, we recombine without modifying the equations of the 0D model (described in Section 2.4)
It is assumed $\zeta_{upr} = const$ and the logistic equation (2.7) is solved as explained in subsection 2.3.2.
Second, the sediment continuity equation (2.12) in discrete form is combined, and starting from equation (2.14), the following map for the 0D system is obtained:

$$B^-_{n+1} = \begin{cases} B^+_{n+1} & \text{if} \quad 0 \leq \mathcal{W}_{n+1} < w_m \,, \quad \text{(a)} \\ \left(1 - \frac{\mathcal{W}_{n+1} - w_m}{1 - w_m}\right)^{\beta} B^+_{n+1} & \text{if} \quad w_m \leq \mathcal{W}_{n+1} \leq 1 \,, \quad \text{(b)} \\ B_{min} & \text{if} \quad \mathcal{W}_{n+1} > 1 \,, \quad \text{(c)} \end{cases} \tag{4.2}$$

where $\mathcal{W} = \frac{\Delta z_B}{\zeta_{upr}} = \frac{E}{\zeta_{upr}}$. Additionally:

$$\mathcal{W}_{n+1} = \frac{E(B^+_{n+1})}{\zeta_{upr}} \,, \tag{4.3}$$

$$B^+_{n+1} = \frac{B^-_n K e^{\sigma \Delta T_F}}{B^-_n \left(e^{\sigma \Delta T_F} - 1\right) + K} \,, \tag{4.4}$$

$$E(B^+_{n+1}) = \left\{ C_2 - C_1 \left[\max\left(\Theta - \theta_{cr}, 0\right)\right]^{\frac{3}{2}} \right\} \frac{\Delta T_F}{L_v} \,, \tag{4.5}$$

with

$$C_1 = \frac{8\sqrt{(s-1)g d_s^3}}{1-p} \,, \tag{4.6}$$

$$C_2 = C_1 \left(\theta_g - \theta_{cr}\right)^{\frac{3}{2}} \,, \tag{4.7}$$

$$C_3 = \frac{q^{3/5} S}{k_{s,g}^2 (s-1) d_s} \,, \tag{4.8}$$

and

$$\Theta = C_3 \left[\left(\frac{k_{s,v} - k_{s,g}}{K} \right) B_{n+1}^+ + k_{s,g} \right]^{\frac{7}{5}} \,. \tag{4.9}$$

The stability of the map is studied as described in Section (10.1) of **Strogatz (2018)**. B^* is a fixed point of a map if it is satisfied $B^* = f(B^*)$, and $B_n = B^*$, where n is the number of iterations. Thus, $B_{n+1} = f(B_n) = f(B^*) = B^*$ and the orbit remains at B^* for all future iterations. To determine the stability of B^*, a nearby orbit $B_n = B^* + \eta_n$ is considered and and it is checked if the orbit is attracted to or repelled from B^*. Thus:

$$B^* + \eta_{n+1} = B_{n+1} = f(B^* + \eta_n) = f(B^*) + f'(B^*)\eta_n + O({\eta_n}^2) \,, \tag{4.10}$$

but since $f(B^*) = B^*$ and neglecting the $O({\eta_n}^2)$, it is obtained:

$$\eta_{n+1} = f'(B^*)\eta_n \,. \tag{4.11}$$

This is a linear equation in η, and is called the linearization about B^*, with the eigenvalue λ=$f'(B^*)$. If $|\lambda| = |f'(B^*)| < 1$, then $\eta_n \to 0$ as $n \to \infty$ and the fixed point B^* is linearly stable. Conversely, if $|\lambda| = |f'(B^*)| > 1$ the fixed point is unstable.
In the map, when $w_m \leq \mathcal{W}_{n+1} \leq 1$:

$$B_{n+1}^- = \left(1 - \frac{\mathcal{W}_{n+1} - w_m}{1 - w_m}\right)^{\beta} B_{n+1}^+ \,, \tag{4.12}$$

in explicit form:

$$B_{n+1}^- = \left(1 - \frac{\left\{ C_2 - C_1 \left[\max\left(\Theta - \theta_{cr}, 0\right) \right]^{\frac{3}{2}} \right\} \frac{\Delta T_F}{L_v} - w_m}{1 - w_m} \right)^{\beta} \frac{B_n^- K e^{\sigma \Delta T_F}}{B_n^- \left(e^{\sigma \Delta T_F} - 1 \right) + K} \,, \tag{4.13}$$

B_{n+1}^- is plotted as a function of B_n^- as illustrated in Figure 4.7 and the intersection point of this curve with the line $B_{n+1}^- = B_n^-$ (red line) is found to determine the fixed point B^*. Then, an analysis is conducted to determine whether the derivative (blue dashed line) at B^* satisfies $|f'(B^*)| < 1$ defining the stability of the system.
In the period-doubling route to chaos, the derivative is equal to $|f'(B^*)| = 1$ at the first bifurcation. If the derivative $|f'(B^*)| < 1$ the system is stable; if the derivative is $|f'(B^*)| > 1$ the system becomes unstable. In the marginal case where $|f'(B^*)| = -1$,

linearization cannot provide any insight into its behavior.
In addition to the local view offered by the linearization, the graphical method of cobweb maps can also be used to provide a picture of the system's global behavior (green line in Figure 4.7). Cobweb maps are especially useful when they can offer explanations where local analysis fails, for example, in marginal cases. From the Cobweb maps method, given an initial condition $B^-_{n_0}$ draw a vertical line until it intersects the curve f. From this point, intersect horizontally the line $B^-_{n+1} = B^-_n$ and then vertically to the curve again. It is necessary to repeat the process n times (excluding the first steps, which represent the transition zone) to obtain the solution of the system.
The same analysis for several values is repeated for (i) the vegetation growth velocity σ of equation (2.7) and (ii) the uprooting parameter β and w_m of equations (2.14, 2.15). These parameters are chosen because they are the main factors to shape the behavior of the analyzed map (4.13). All the other model parameters are as described in Table 3.2, moreover the flood intensity q is constant and equal to 12 m^2/s and the root growth velocity is $\sigma_r = \infty$.

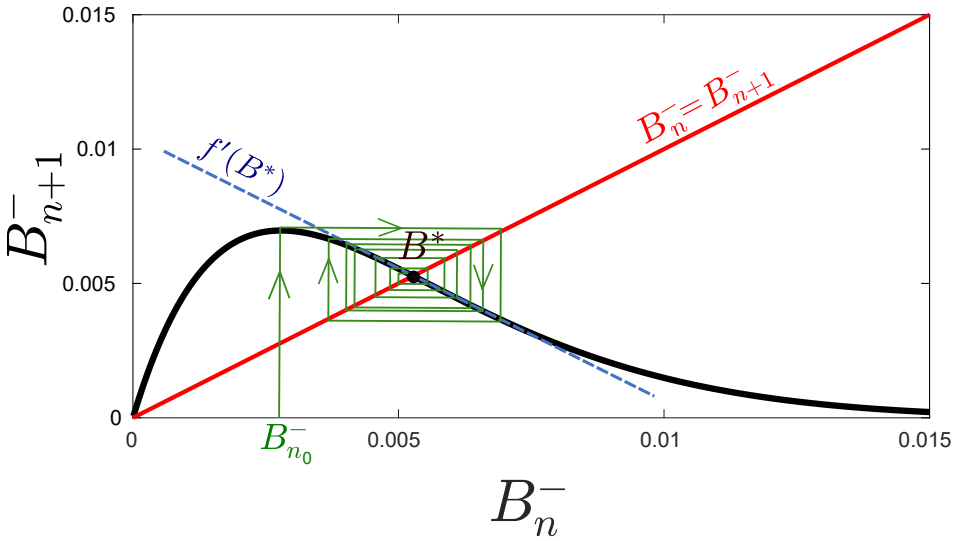

Figure 4.7: Stability analysis and Cobweb map. To study the stability of the system, B^-_{n+1} is plotted as a function of B^-_n and the intersection point of this curve with the line $B^-_{n+1} = B^-_n$ is found to determine the fixed point B^*. An analysis of the derivative at B^* is then conducted to determine the system's stability, where $|f'(B^*)| < 1$ indicates stability, while $|f'(B^*)| > 1$ signifies instability. In this Figure, $|f'(B^*)| < 1$, thus the system is stable and the Cobweb map (green line) converges to the unique solution of the system, the fixed point B^*.

Maximum Lyapunov Exponent (λ)

By definition, a chaotic system exhibits aperiodic oscillations, strong sensitivity on initial conditions, and positivity of the Maximum Lyapunov Exponent (λ). In the 0D discrete model the Maximum Lyapunov Exponent (λ) is calculated as described in Section (10.5) of **Strogatz (2018)**. In fact, the 0D model is a dynamical system defined as a *map* because time is discrete rather than continuous.

Given an initial point B_{n1}, consider a neighboring point $B_{n2} = B_{n1} + \delta_0$, where the initial separation δ_0 is extremely small. Let δ_n be the distance after n iterations. If $|\delta_n| \approx |\delta_0| e^{\lambda n}$, then λ is called the Maximum Lyapunov Exponent (λ). Considering that:

$$\delta_n = f^n(B_{n1} + \delta_0) - f^n(B_{n1}) \,, \tag{4.14}$$

thus, if λ is computed, it is obtained:

$$\lambda = \frac{1}{n} \ln |\frac{\delta_n}{\delta_0}| = \frac{1}{n} \ln |\frac{f^n(B_{n1} + \delta_0) - f^n(B_{n1})}{\delta_0}| \,, \tag{4.15}$$

and with $\delta_0 \to 0$:

$$\lambda = \frac{1}{n} \ln |(f^n)'(B_{n1})| \,, \tag{4.16}$$

applying the chain rule and considering $n \to \infty$, the Maximum Lyapunov Exponent (λ) for the orbit starting at B_{n1} is defined as:

$$\lambda = \lim_{n \to \infty} \left\{ \frac{1}{n} \sum_{i=0}^{n-1} \ln |f'(B_{n_i})| \right\} \,, \tag{4.17}$$

λ is positive for chaotic attractors; λ is negative for stable fixed points and periodic oscillations.

Numerical simulations

In the non-spatial model the magnitude of the erosion process, serving as a proxy for the hydro-morphodynamic disturbance, is first quantified using the erosion potential E_p **(Caponi and Siviglia, 2018)**, as defined in Subsection (3.2.1). Additionally, the proxy for the system's resistance is defined as the constant value of the root depth ζ_{upr}, due to the ability of roots to anchor in the riverbed and resist to the disturbance. The choice of a constant root depth is mainly made to simplify the model and have full control over the dynamics. Physically, this choice can be explained by the fact that plant roots grow rapidly during the early stages of life and then remain rather stable over time. Furthermore, the ratio between disturbance and resistance ($\omega_{z_B} = \frac{E_p}{\zeta_{upr}}$) is introduced as a normalized parameter to measure the relative strength of these components, as suggested by previous work **(Bertoldi et al., 2014; Caponi and Siviglia, 2018; Perona and Crouzy, 2018)**. When ω_{z_B} is small, it indicates that the anchoring capacity of roots prevails over the disturbance, favoring vegetation establishment. Conversely, when ω_{z_B} is large, it signifies that the disturbance prevails over the resistance force and plants are uprooted.

The chosen configuration allows isolating and controlling the intrinsic mechanism of erosion caused by the the presence of vegetation, as explained in Section (2.1).
A set of numerical simulations is performed to quantify the Maximum Lyapunov Exponent by modifying: (i) the value of the vegetation growth rates σ and (ii) the value of ω_{z_B}, (iii) the unit width stream power, computed as the product of the unit-width discharge q by the river slope, S. Although the unit width stream power and ω_{z_B} are two dependent parameters, they have been investigated separately because the aim is to provide an estimation of chaos for a well-known parameter in morphodynamics (unit width stream power) rather

than for the estimated one (ω_{z_B}). To explore the fractal solution of the system, a matrix of simulations is performed where the vegetation growth rate σ is modified on the x-axis and the parameter $\Sigma = \frac{1}{\omega_{z_B}}$ and β are modified on the y-axis. The Maximum Lyapunov Exponent (MLE) is then calculated on the third axis (colors indicate different values of the MLE) for each simulation.

All the other model parameters are as described in Table 3.2, moreover the flood intensity q is constant and equal to 12 m^2/s and the root growth velocity is $\sigma_r = \infty$. The value of E_p for $q = 12\ m^2/s$ is 0.35 m. To ensure reaching the steady state solution, 1000 growth-flood cycles were simulated, with the first 700 cycles discarded and only the last 300 cycles considered, as outlined in Subsection (3.2.1).

4.2.2 Results

Stability analysis and Cobwebs

In Figure 4.8 the stability of the system is investigated for several values of the vegetation growth rate σ, plotting B^-_{n+1} as a function of B^-_n and finding the intersection point of this curve with the line $B^-_{n+1} = B^-_n$ to determine the fixed point B^*. In Figure 4.8A it can be observed that all the curves show a behavior with a maximum. For $\sigma = 0.10$ (Figure 4.8B) the derivative $|f'(B^*)| < 1$, indicating that the system is stable. The fixed point B^* is the solution of the system, as shown by the convergence of the Cobweb map. However, when $\sigma = 0.12$ (Figure 4.8C) the derivative $|f'(B^*)| > 1$, indicating system instability. In this case, when the Cobweb map is drawn, the system is observed to jump, after a period of transition, between two different solutions (green dots), exhibiting periodic oscillation. If $\sigma = 0.18$ (Figure 4.8D) the derivative $|f'(B^*)| > 1$, thus the system shows instability and the Cobweb map jumps between infinite solutions, displaying a chaotic behavior.
An investigation is conducted into how the stability of the system is altered by varying values of β and w_m (refer to Figure 4.9): curves show always the same behavior with a maximum that depends on the chosen parameters. For the same value of $\beta = 1$, the curve with the highest peak is the one with $w_m = 0.50$ because uprooting occurs later for larger values of w_m. In the case with $\beta = 9.0$, the peak of the curve is the lowest because with high values of β the uprooting curve descends rapidly.
Through stability analysis, it is demonstrated that the system's route to chaos is a period-doubling bifurcation. The period-doubling bifurcation will be presented in the next Subsection, in Figure 4.10A, where both the numerical and analytical results, coinciding, are presented together. In Figure 4.10A, for the selected parameters $\zeta_{upr} = 0.12$, $\beta = 1.0$, and $w_m = 0.27$, it is found that the derivative is equal to $|f'(B^*)| = 1$ at the first bifurcation point for $\sigma = 0.10$. Before the first bifurcation, the derivative is $|f'(B^*)| < 1$ and the system is stable; after the first bifurcation, the derivative is $|f'(B^*)| > 1$ and the system becomes unstable.

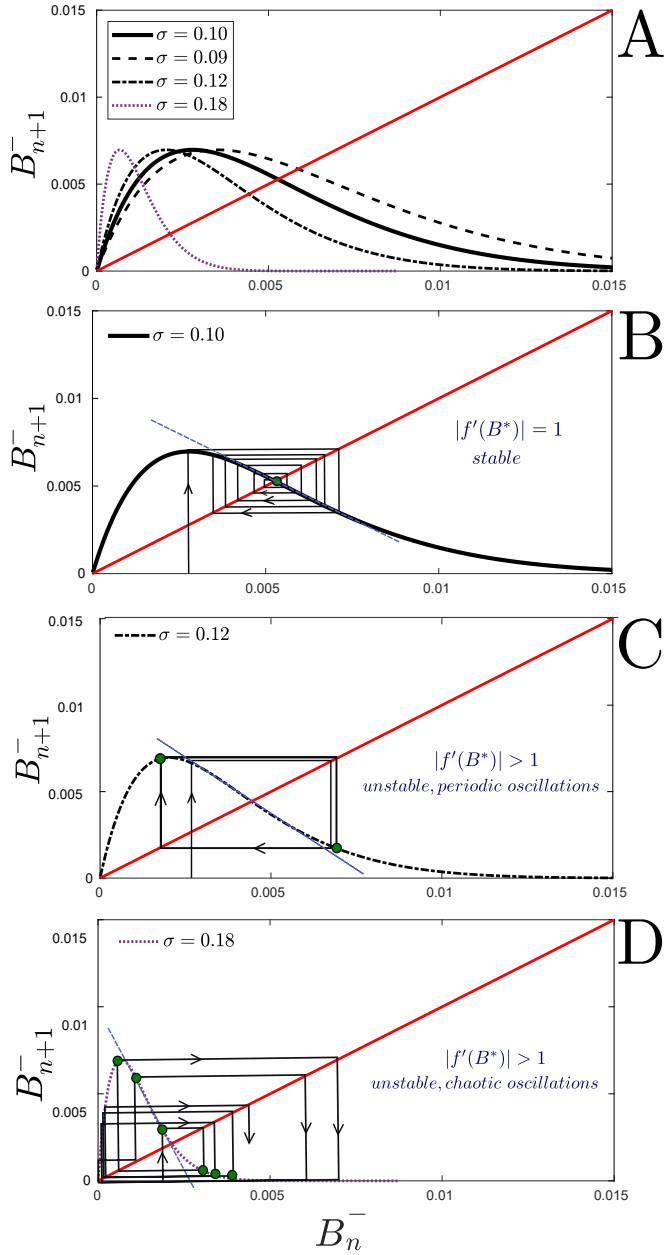

Figure 4.8: Stability analysis of the system for different values of σ, where $\zeta_{upr} = 0.12$, $\beta = 0.9$ and $w_m = 0$. These values have been chosen considering that β and w_m can vary, as detailed in the Appendix A.3. For $\sigma = 0.10$ the derivative $|f'(B^*)| < 1$, indicating system stability. The fixed point B^* is the solution of the system, as shown by the convergence of the Cobweb map. When $\sigma = 0.12$ the derivative $|f'(B^*)| > 1$ indicating system instability. In this case, when the Cobweb map is plotted, the system is observed to jump, after a period of transition, between two distinct solutions (green dots), indicating a periodic oscillation. If $\sigma = 0.18$ the derivative $|f'(B^*)| > 1$, thus the system shows instability and the Cobweb map displays infinite solutions and thus a chaotic behavior.

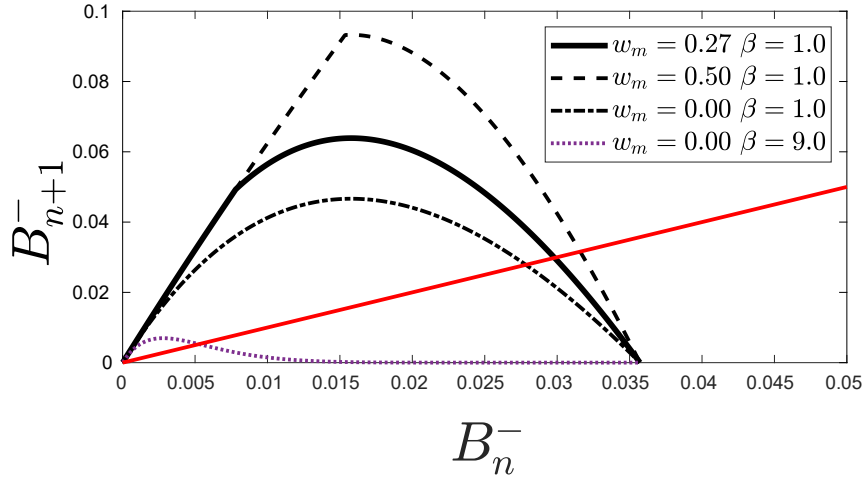

Figure 4.9: Stability analysis of the system for different values of β and w_m: curves show always a behavior with a maximum.

Period-doubling bifurcation and positivity of MLE

In the numerical results presented here, $\zeta_{upr} = 0.12$, $\beta = 1.0$, and $w_m = 0.27$ are utilized. These values are obtained by fitting the 0D model to the 1D model, as illustrated in Appendix (A.3). As shown in the Appendix (A), despite the simplification, the 0D model shows a dynamic behavior similar to that of the 1D model.
Model results show (refer to Figure 4.10A) a route to chaos defined by a period-doubling bifurcation. The first bifurcation occurs at $\sigma = 0.10$ and the second bifurcation occurs at $\sigma = 0.127$, respectively, the chaotic regime starts at about $\sigma = 0.134$. The corresponding Maximum Lyapunov Exponents (refer to Figure 4.10B) are negative when the solution is stable or periodic, zero at the bifurcation points, and positive in the chaotic zone. The time scale of predictability of the system is also calculated, defined as the inverse of the Maximum Lyapunov Exponent **(Kantz and Schreiber, 2004)**. Since in the calculation of the MLE, every iteration n in equation (4.16) corresponds to one growth-flood cycle, the time scale of predictability $\frac{1}{\lambda}$ is approximately calculated as 2 growth-flood cycles. This implies that in the chaotic zone, after a few growth-flood cycles, the system is no longer predictable. Furthermore, it is demonstrated (refer to Figure 4.10C) that the MLE is independent of the model parameters and remains positive and constant across a broad range of hydro-morphodynamic disturbance/vegetation resistance ratios ω_{z_B}. Chaotic behavior is prevented when ω_{z_B} tends to zero or infinity resulting in negative values of the MLE (Figure 4.10C, *Inset*). Additionally, the variability of the MLE is examined as a function of the unit-width stream power within a range typical of gravel-bed rivers (Figure 4.10D). Again, the values are largely constant, between 0.04 and 0.07, and depend more on the choice of parameters β and w_m than on the values of the stream power. However, rivers with small stream power (0.02-0.03 m^2/s) are characterized by smaller values of the Lyapunov exponents and thus longer predictability horizon. These results confirm that the Lyapunov time of the system is only a few growth-flood cycles and is nearly constant over a wide range of parameters and hydro-morphodynamic configurations.

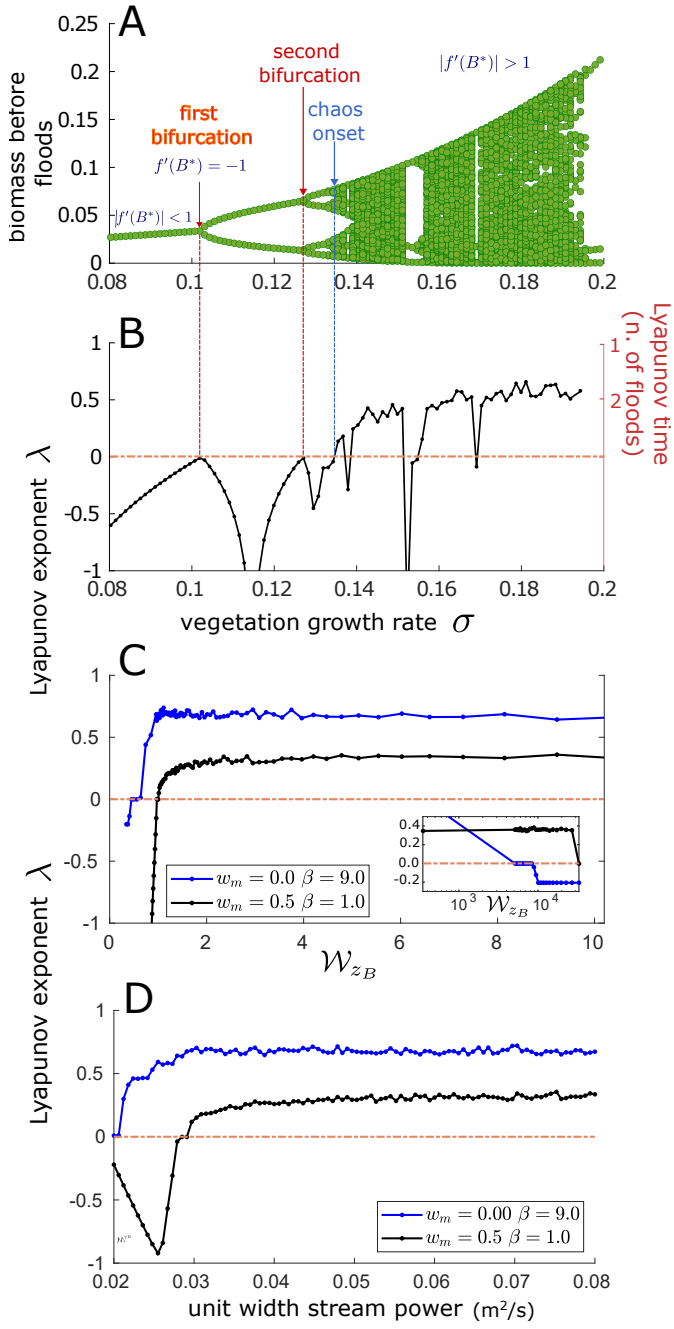

Figure 4.10: (A) Bifurcation diagram showing biomass before floods B^- as a function of σ: the route to chaos is defined by period-doubling. (B) The corresponding Maximum Lyapunov Exponents are negative when the solution is stable or periodic, zero at the bifurcation points, and positive in the chaotic zone. The time scale of predictability in the chaotic zone is about 2 growth-flood cycles. (C) The Maximum Lyapunov Exponent is positive and nearly constant over a wide range of disturbance/resistance ratios and (D) also for typical ranges of unit-width stream power.

Fractals

The solution of the system is a fractal solution (Figure 4.11), i.e., it is self-similar and it repeats itself on different scales infinitely. In fact, in the zoomed-in inset, one can observe the curve repeating infinitely on smaller scales with smaller portions exhibiting similar patterns to the entire structure (self-similar). This result shows how the solution of the system has an intrinsic order and it's not random. By changing the set of parameters, modifying, for example, the uprooting parameter β on the y-axis, the solution remains fractal but yields different figures (Figure 4.12).

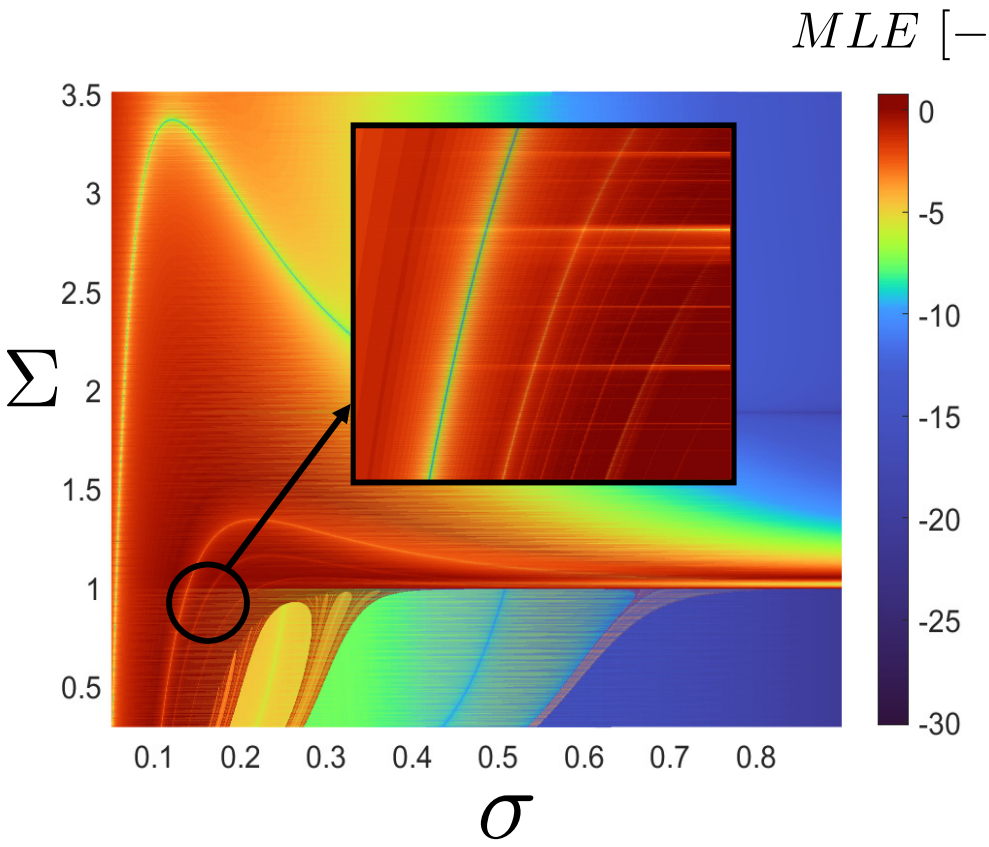

Figure 4.11: Fractal solution of the system. A matrix of simulations is conducted, where the vegetation growth rate σ is plotted on the x-axis and the parameter $\Sigma = \frac{1}{\omega_{z_B}}$ is plotted on the y-axis. Subsequently, the Maximum Lyapunov Exponent (MLE) is plotted on the third axis, with colors indicating different values of the MLE. In the zoomed-in inset, the MLE color scale is different to highlight the repetition property.

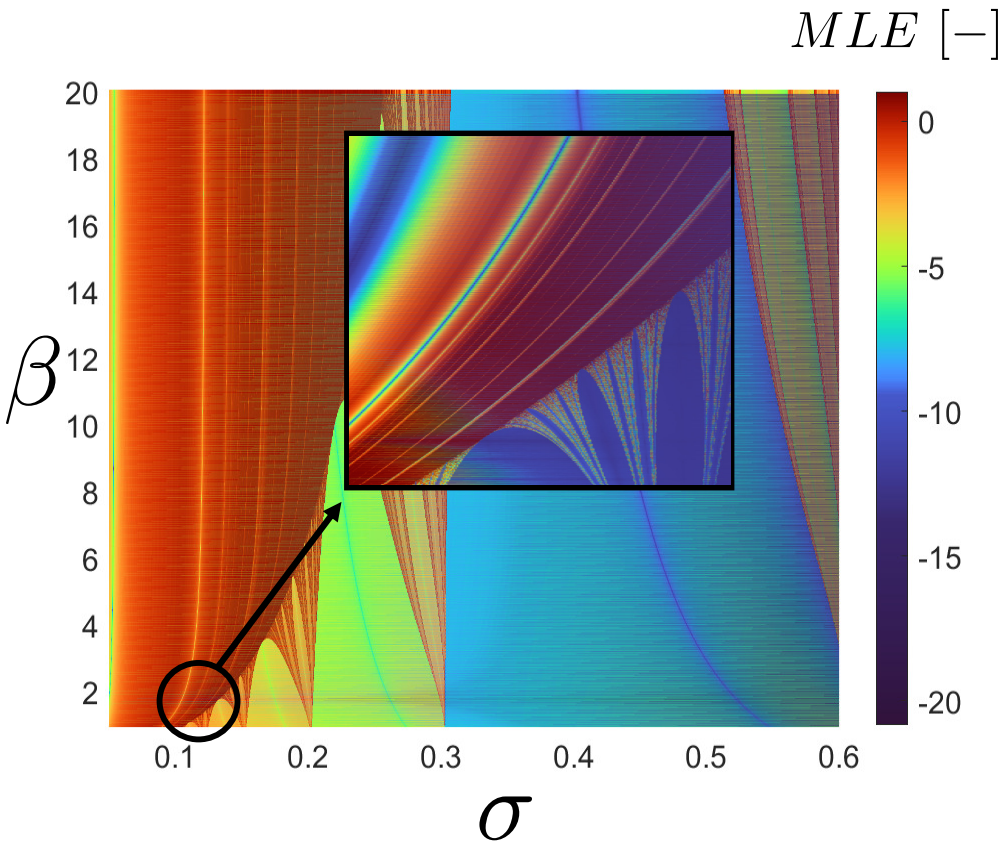

Figure 4.12: Fractal solution of the system. A matrix of simulations is conducted where the vegetation growth rate σ is modified on the x-axis and the uprooting parameter β is adjusted on the y-axis. Subsequently, the Maximum Lyapunov Exponent (MLE) is plotted on the third axis, with colors indicating different values of the MLE. In the zoomed-in inset, the MLE color scale is different to highlight the repetition property.

4.3 Oscillations and chaos in the 1D model

In this section, the 1D model is used to:

(i) analyze some periodic and aperiodic oscillatory time series, calculate the corresponding Maximum Lyapunov Exponents, and show the attractors.

(ii) plot the bifurcation graph of the system as a function of the vegetation growth rate σ.

4.3.1 Methodology

Maximum Lyapunov Exponent (λ)

The calculation of the Maximum Lyapunov Exponent (λ) in a multi-dimensional system is more complex than the method used for the 0D model (map).
Indeed, the time evolution of dynamical systems is defined within a specific phase space **(Kantz and Schreiber, 2003)**. Consequently, a vector space can be defined, referred to as the 'phase space' of the system. By specifying a point within this space, the system's state is effectively determined.
The primary challenge encountered is reconstructing the phase space of the system from a time series, which essentially constitutes an observation of its behavior. This challenge is commonly referred to as the 'problem of the phase space reconstruction,' and it is solved using the method of delay. The time series consists of a sequence of scalar measurements, denoted as n, representing a particular quantity (in this case, vegetation B), which depends on the current state of the system (x), taken at multiples of a fixed sampling time Δt:

$$B_n = B(\mathbf{x}(n\Delta t)) \ .$$

Through the method of delay, the phase space of the system (referred to as the embedding phase space) can be reconstructed from the time series. A delay reconstruction is formed by the vectors $\mathbf{B}_n$, which are defined as follows:

$$\mathbf{B}_n = (B_{n-(m-1)\tau}, B_{n-(m-2)\tau}, \ldots, B_{n-\tau}, B_n) \ ,$$

Here, m represents the dimensions, and τ is the lag or delay time, which is the time difference in the number of samples τ (or in time units, $\tau\Delta t$) between adjacent components of the delay vectors.
In chaotic systems, trajectories diverge exponentially fast in time. The exponent that measures how fast the system diverges (and thus the strength of chaos) is the Maximum Lyapunov Exponent (λ).
Let $\mathbf{B}_{n1}$ and $\mathbf{B}_{n2}$ be two points in phase space with a distance $||\mathbf{B}_{n1} - \mathbf{B}_{n2}|| = \delta_0 \ll 1$. Denote by $\delta_{\Delta n}$ the distance, some time Δn ahead, between the two trajectories emerging from these points, $\delta_{\Delta n} = ||\mathbf{B}_{n1+\Delta n} - \mathbf{B}_{n2+\Delta n}||$. Then, λ is determined by:

$$|\delta_{\Delta n}| \approx |\delta_0| e^{\lambda \Delta n}, \quad \delta_{\Delta n} \ll 1, \quad \Delta n \gg 1 \ . \tag{4.18}$$

Naturally, two trajectories can not separate farther than the size of the attractor, such that the law of equation (4.18) is only valid during times in for which $\delta_{\Delta n} \ll 1$. If λ is positive, this means that the nearby trajectories diverge exponentially, indicating chaos. The inverse

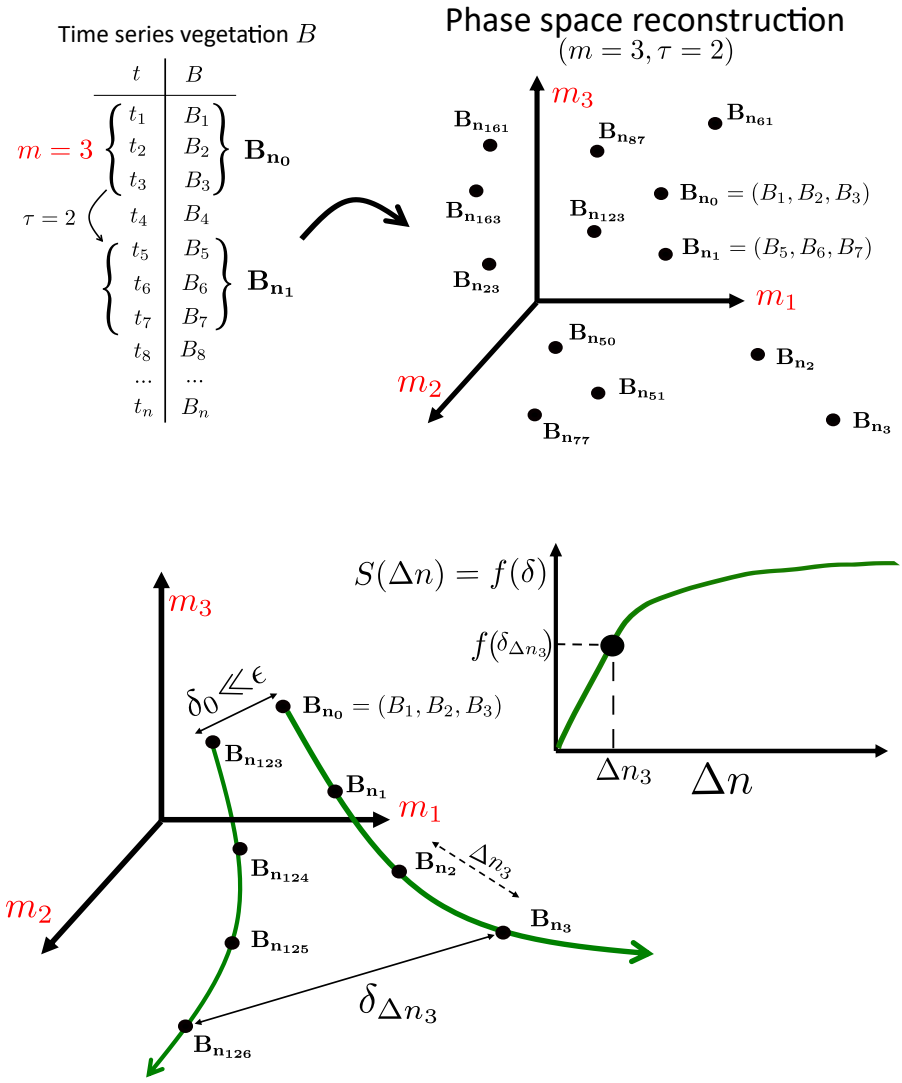

Figure 4.13: Calculation of the Maximum Lyapunov Exponent (λ) in the 1D model. From the time series of vegetation B, the phase space of the system can be reconstructed using the method of delays. In the example depicted in this Figure, a dimension of $m = 3$ and a time delay of $\tau = 2$ are chosen; from the time series, 3-dimensional vectors $\mathbf{B}_n$ are created and plotted in the phase space (m_1, m_2, m_3). τ is the time difference in number of samples between adjacent components of the delay vectors. Next, all the neighbors of a selected point $\mathbf{B}_{n_0}$ are identified, which are points closer than ϵ at $\Delta n = 0$ (i.e., $|\mathbf{B}_{n_{123}} - \mathbf{B}_{n_0}| = \delta_0 < \epsilon$). For the sake of clarity, the Figure displays only one neighbor, $\mathbf{B}_{n_{123}}$. Following that, the divergence of the trajectories' distance, denoted as δ, is calculated over a relative time period Δn. Finally, $S(\Delta n)$ is computed as a function of δ over time and an average of all the neighbors. This process is repeated for several values of $\mathbf{B}_{n_0}$. The initial slope of $S(\Delta n)$ is an estimation of the Maximum Lyapunov Exponent λ, which provides insights into the chaotic nature of the system.

of the Maximum Lyapunov Exponent ($\frac{1}{\lambda}$) is the time scale of predictability of the system. There are several algorithms for the calculation of the Maximum Lyapunov Exponent (λ); here, the algorithm proposed by **Kantz** (**1994**) is utilized.
In the embedding phase space, a point $\mathbf{B}_{n_0}$ is chosen from the time series, and all neighbors with a distance smaller than ϵ are selected. Then, for many values of n_0, the average over the distances of all neighbors to the reference part of the trajectory is computed as a function of the relative time. The logarithm of the average distance at time Δn is some effective expansion rate over the time span Δn (plus the logarithm of the initial distance). Thus, it is calculated:

$$S(\Delta n) = \frac{1}{N}\sum_{n_0=1}^{N} \ln\left(\frac{1}{|U(\mathbf{B}_{n_0})|}\sum_{\mathbf{B}_n \in U(\mathbf{B}_{n_0})} |B_{n_0+\Delta n} - B_{n+\Delta n}|\right). \tag{4.19}$$

Where $\mathbf{B}_{n_0}$ are embedding vectors, $\mathbf{U}(\mathbf{B}_{n_0})$ is the neighborhood of $\mathbf{B}_{n_0}$ with diameter ϵ, $\delta = |B_{n_0+\Delta n} - B_{n+\Delta_n}|$ is the distance δ. If, for some range of Δn, the function $S(\Delta n)$ exhibits a robust linear increase and it reaches a plateau **(Franchi and Ricci, 2014)**, the system is chaotic, and its slope is an estimation of the Maximum Lyapunov Exponent (λ) per time step, which must be converted to the desired units (e.g., number of growth-flood cycles). $S(\Delta n)$ is calculated for various values to enhance the robustness of the analysis because, a priori, the embedding dimension m, the time lag τ and the optimal distance ϵ may not be known. The program $lyap_k$ in the TISEAN 3.0.1 software package **(Hegger et al., 1999)** performs the necessary calculations to create the curves $S(\Delta n)$ and estimate the Maximum Lyapunov Exponent (λ).
The analysis is conducted using the vegetation B time series including the transient phase from growth-flood cycle 1-50. A negative value of the Maximum Lyapunov Exponent (λ) indicates stable or periodic solutions, whereas positive values indicate irregular-chaotic dynamics.

Numerical simulations

The magnitude of the erosion process, which represents the hydro-morphodynamic disturbance, is initially quantified using the erosion potential E_p, as defined in Subsection (3.3.1). The resistance ζ_{upr} and the ratio between disturbance and resistance ($\omega_{z_B} = \frac{E_p}{\zeta_{upr}}$) are calculated as defined in Subsection (4.2.1).
A set of numerical simulations are performed to estimate the Maximum Lyapunov exponent and the attractors by modifying: (i) the value of ω_{z_B} to investigate several ratios between the disturbance and the resistance, (ii) the value of the vegetation growth rates σ to investigate different vegetation types. All the results plotted represent the average values of the variables of the system within the patch.
All the other model parameters are as described in Table 3.2, moreover the flood intensity q is constant and equal to 12 m^2/s, the flood duration is 3 hours and the root growth velocity is $\sigma_r = \infty$. The value of E_p for $q = 12\ m^2/s$ is 0.35 m, which corresponds to a flood event with a return period of approximately 2-5 years ($\theta \approx 0.23$).

4.3.2 Results

Time series analysis and attractors

Model results show three different possible behaviors: (i) a stable solution (Figure 4.14A), (ii) periodic oscillations (Figure 4.14B), or (iii) aperiodic oscillations (Figure 4.14C).
In Figure 4.14A, the disturbance is weaker than the resistance ($\omega_{z_B} = 10^{-3}$). Thus, over time, vegetation B grows ($\sigma = 0.2$) and it is not uprooted, indeed the root resistance is greater than the erosion. After a transition phase, it reaches a stable solution at the vegetated state ($K = 1$). For the sake of clarity, in Figure 4.14 it is not plotted the transition phase (1-28 growth-flood cycles).
If the trajectories of the three variables of the system are plotted (x-axis represents vegetation B, y-axis represents the erosion Δz_B, and the color scale represents the water depth h) in the phase space, it can be observed that the attractor of the system consists of only one point (see the *right side* of Figure 4.14A).
In Figure 4.14B, during low flow periods, vegetation grows until the carrying capacity ($K = 1$), due to the high value of ($\sigma = 0.8$), but then it is completely uprooted during floods due to the higher value of the disturbance ($\omega_{z_B} = 2.9$). This behavior gives rise to periodic oscillations and thus, if the trajectories of the three variables of the system in the phase space are plotted, it can be observed that the attractor of the system consists of a periodic 2D-curve (see the *right side* of Figure 4.14B).
In Figure 4.14C vegation grows ($\sigma = 0.2$) during the first low flow period but then it is partially uprooted during the first flood ($\omega_{z_B} = 2.9$), thus, in the second low flood period it grows differently due to the varied initial conditions and so forth. This behavior gives rise to aperiodic oscillations between the bare soil and the vegetated state. If the trajectories of the three variables of the system are plotted in the phase space, it can be observed that the attractor of the system in this case consists of a strange 3D-attractor, which never repeat itself (see the *right side* of Figure 4.14C). Moreover, when the initial condition of the vegetation (B_1, B_2, B_3) is changed by a small quantity ($\approx 10^{-5}$), it is found that the system in Figure 4.14C is strong sensitive to initial conditions. Thus, the trajectories of the three simulations start closed but then they diverge over time. In Figure 4.14A and 4.14B the trajectories of B_1, B_2, B_3 overlap because when the system is in a periodic or stable configuration is not sensitive dependent on initial conditions.

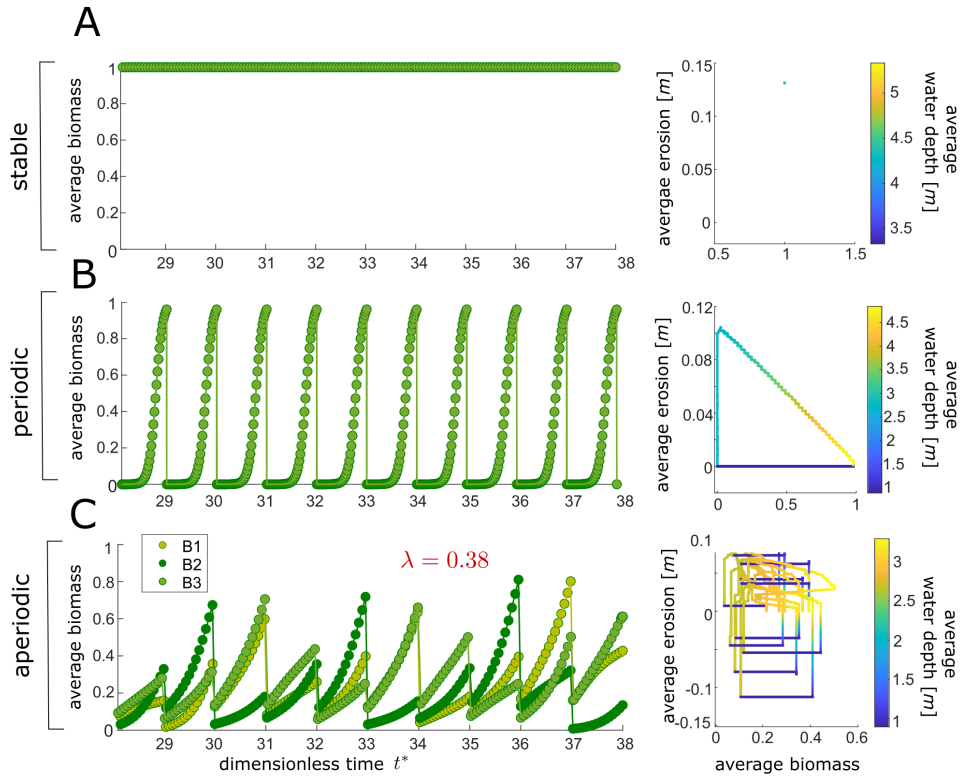

Figure 4.14: (A) If $\omega_{z_B} = 10^{-3}$ and $\sigma = 0.2$, vegetation B reaches, after a transition phase, a stable solution at the vegetated state ($K = 1$) over time t^*. The transition phase (1-28 growth-flood cycles) is not plotted. The attractor of the system consists of only one point (*right side*). (B) If $\omega_{z_B} = 2.9$ and $\sigma = 0.8$, vegetation grows until the carrying capacity $K = 1$, but then it is completely uprooted during floods. This behavior gives rise to periodic oscillations, and the attractor of the system consists of a periodic 2D-curve (*right side*). (C) If $\omega_{z_B} = 2.9$ and $\sigma = 0.2$ vegetation grows during the first low flow period but then it is partially uprooted during the first flood. Subsequently, during the second low flow period it shows distinct growth due to different initial conditions and so forth. This behavior gives rise to aperiodic oscillations and the attractor of the system is a strange 3D-attractor (*right side*). Moreover, the initial condition of the vegetation is changed by a small quantity ($B_1 = 1.0\times10^{-5}, B_2 = 1.1\times10^{-5}, B_3 = 1.2\times10^{-5}$) and it is found that the system in this case is strong sensitive to initial conditions, thus the trajectories of the three simulations diverge over time and the Maximum Lyapunov Exponent is positive ($\lambda = 0.38$).

Maximum Lyapunov Exponent (λ)

In Figure 4.15, the Maximum Lyapunov Exponent (λ) is calculated for time series of vegetation B corresponding to Figure 4.14. The cases in Figure 4.15A and Figure 4.15B, corresponding to, respectively, the calculation of the time series of Figure 4.14A and Figure 4.14B, show negative values of the Maximum Lyapunov Exponent (λ). In fact, in Figure 4.15A the curve $S(\Delta n)$ exhibits a robust linear increase but it does not reach a plateau over the time span Δn. In Figure 4.15B the curve $S(\Delta n)$ does not exhibit a robust linear increase over the time span Δn. In these cases the nearby trajectories do not diverge exponentially, the system is not chaotic, and it shows stable solution (Figure 4.14A) or periodic oscillations (Figure 4.14B). In the case of Figure 4.15C, corresponding to the calculation of the time series of Figure 4.14C, the curve $S(\Delta n)$ exhibits a robust linear increase reaching a plateau over time span Δn. The slope of its linear increase (λ=0.38) represents an estimation of the Maximum Lyapunov Exponent. In this case the nearby trajectories diverge exponentially, the system is chaotic, and it shows irregular oscillations. The inverse of the Maximum Lyapunov Exponent is the time scale of predictability, which must be converted to the desired units (i.e., $\approx$ 2.6 number of growth-flood cycles). This result is consistent with the Maximum Lyapunov Exponent calculated in the 0D model (refer to 4.2.2).

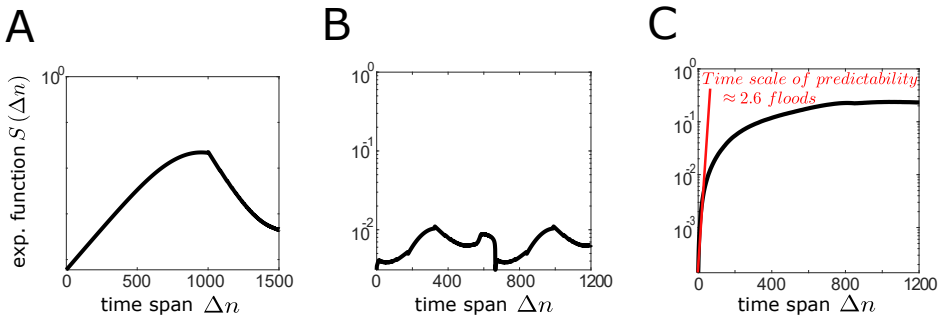

Figure 4.15: Value of the Maximum Lyapunov Exponent (λ) for time series of vegetation B corresponding to Figure 4.14. In Figure 4.15A (refer to Figure 4.14A) the curve $S(\Delta n)$ exhibits a linear increase but it does not reach a plateau over time span Δn, representing a non-chaotic solution. In Figure 4.15B (refer to Figure 4.14B) the curve $S(\Delta n)$ does not exhibit a robust linear increase, representing a non-chaotic solution. In Figure 4.15C (refer to Figure 4.14C) the curve $S(\Delta n)$ exhibits a robust linear increase and a plateau over time span Δn, representing a chaotic solution. The inverse of the slope of its linear increase (i.e., Maximum Lyapunov Exponent λ) is the time scale of predictability (e.g., $\approx$ 2.6 number of growth-flood cycles).

Since in Figure 4.14C it is found (i) strong dependence on initial conditions, (ii) aperiodic oscillations and (iii) positivity of the Maximum Lyapunov Exponent ($\lambda = 0.38$), the chaoticity of the system for this parameter setting is demonstrated.

Bifurcation graph and chaotic zone

In Figure 4.16A and 4.16B, the vegetation at the beginning (B^-, yellow points) and at the end (B^+, green points) of every growth period is plotted as a function of the parameter σ. If ω_{z_B} is small (Figure 4.16A) or big (Figure 4.16B) the system does not show chaotic behavior. In Figure 4.16A, the resistance ζ_{upr} is much greater than the disturbance (erosion potential E_p) and the system reaches its stability at the vegetated state, thus B^-= B^+= K, for every value of σ. In Figure 4.16B, vegetation grows, during low flow periods, depending on the value of σ, but the disturbance E_p is much greater than the resistance ζ_{upr}. Indeed, vegetation is completely uprooted at every flood period ($B^- = Bmin$), inducing periodic oscillations.
If the vegetation resistance and the hydro-morphodynamic disturbance have the same order of magnitude the system shows chaotic behavior (Figure 4.16C). In the case C, a plot of the biomass before floods, B^+, is shown as a function of σ, revealing a bifurcation diagram. Within the range of σ [0.0, 0.65], the system exhibits chaotic behavior, characterized by multiple values of B^+ due to aperiodic oscillations, as well as periodic windows — open areas where periodic cycles emerge within the chaotic zone. A stable period-3 cycle is found in the range [0.22, 0.26] and a stable period-2 cycle is observed in the largest period window in the range [0.34, 0.52]. For growth rates above 0.69 the solutions are periodic. Moreover, the Maximum Lyapunov Exponent (red bars) is calculated for several time series of vegetation B, consistently demonstrating its positivity within the chaotic zone. The time scale of predictability of the system is also calculated, revealing its equivalence to only a few growth-flood cycles (3-4) within every range of the chaotic behavior, as shown in the right vertical axis of the figure. This implies that the system, with these parameter settings, is not predictable after a few growth-flood cycles.
It is also important to underline that the results are plotted for the variable vegetation B, but all the other variables of the system behave dynamically in the same way. In other words, if the vegetation is stable, the other variables of the system are also stable; if it oscillates periodically, the other variables also oscillate periodically; if the vegetation is chaotic, the other variables are also chaotic.

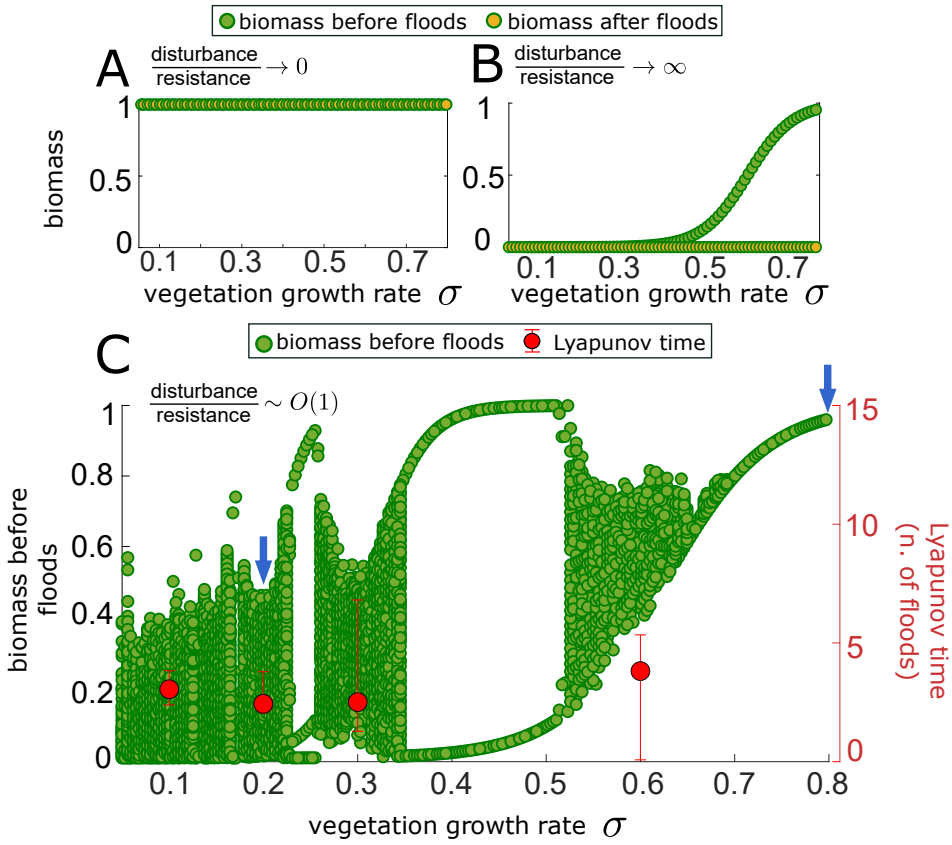

Figure 4.16: The vegetation at the beginning (B^-) and at the end (B^+) of every growth period is plotted as a function of the parameter σ. (A) If the resistance is much bigger than the disturbance ($\frac{E_p}{\zeta_{upr}} = 10^{-3}$) the system reaches its stability at the vegetated state $B^- = B^+ = 1$, for every value of σ. (B) If the disturbance is much bigger than the resistance ($\frac{E_p}{\zeta_{upr}} = 10^6$), the vegetation grows during low flow periods but then it is completely uprooted at every flood period ($B^- = Bmin$), inducing periodic oscillations. (C) If the resistance and the disturbance have the same order of magnitude ($\frac{E_p}{\zeta_{upr}} = 2.9$) the system shows chaotic behavior, characterized by multiple values of B^+ due to aperiodic oscillations, and a bifurcation diagram. The Maximum Lyapunov Exponent (red bars) is calculated for several time series of vegetation B, consistently demonstrating its positivity within the chaotic zone. The red dot in the center of the plot represents the mean, while the bottom and top of the error bars represent the minimum and the maximum values in the data set, respectively. Moreover, the time scale of predictability of the system is calculated, as shown on the right vertical axis. The blue arrows refer to the vegetation time series in Figure 4.14B and 4.14C.

4.4 Conclusion and implications

In this chapter, the established objectives are achieved:

(i) Through these analyses, it has been established that the observed aperiodic oscillations are chaotic. The system exhibits chaotic oscillations when (i) the total negative feedback loop prevails and when (ii) vegetation resistance (proxy ζ_{upr}) is of the same order of magnitude as the hydro-morphodynamic disturbance (proxy E_p). The route to chaos for the system is also identified, namely period-doubling bifurcation, and established that the system is driven by the intrisic mechanisms of eco-morphodynamic feedbacks. The fractal solutions and attractors are also defined.

(ii) The timescale of predictability (Lyapunov time) has been quantified, equivalent to a few growth-flood cycles. This implies that the system is not predictable beyond a few growth-flood cycles.

It's important to mention that these conclusions are valid for both the spatial and non-spatial models.

These results show how the system can lose its equilibrium and exhibit either periodic or chaotic oscillations depending on where it is located in the period-doubling bifurcation (refer to Figure 4.10C and 4.16C). From these results, it seems that the system can enter and exit chaotic zones, depending on the ratio between plant resistance and hydro-morphodynamic disturbance. When the system is in the stable or periodically oscillatory zone, it is deterministic predictable. However, when it enters inside the chaotic zone, it becomes unpredictable in the long term. In fact, in the chaotic zone, the maximum Lyapunov time scales indicates a predictability for only a few growth-flood cycles.
In natural rivers, the duration of these growth-flood cycles can vary considerably, depending on the type of vegetation (e.g., aquatic vs. riparian) and on the flood magnitude that is able to uproot the vegetation. In low-energy small rivers where macrophytes are the main engineering species **(Gurnell, 2014)** the growth-flood cycle is likely to be annual. In larger gravel-bed rivers, the return interval of floods that can significantly affect vegetation has been reported to vary from 1-2 years for partial vegetation removal on highly dynamic braided rivers **(Surian et al., 2015)**, to several decades for major vegetation renewal **(Belletti et al., 2014)**. Riparian trees grow rapidly, exerting a strong impact on the flow field already after a few years, when the biomass is closer to the ground. Also the resistance of riparian plants develops in short time, where roots of phreatophytic plants grow to reach the ground water level and can easily reach depths $> 1\ m$ in 1-2 years **(Mahoney and Rood, 1998)**. This analysis suggests that chaotic behavior is more likely to manifest when the magnitude of flood disturbance and associated erosion closely matches the resistance exerted by roots. Therefore, different river systems may exhibit chaotic behavior on different time scales, also depending on the growth stage of the vegetation and its root network. Moreover, these results suggest that external factors that amplify the erosion process, such as bedform migration and bank erosion, are likely to modify the nonlinear dynamics considered here, where the morphological disturbance is uniquely generated by the presence of vegetation. Increased erosion, if not balanced by vegetation resistance, may prevent the emergence of chaos within the system. This intrinsic mechanism is not limited to rivers

and can play an important role in different types of vegetated landscapes, where the interplay between time-dependent disturbances and vegetation resistance is key to shaping their evolution, such as in salt marshes, wetlands, and coastal dunes **(Goldstein and Moore, 2016; Marani et al., 2010; Bertagni et al., 2018; Schwarz et al., 2018)**.
Chaotic behavior has been found in fluvial system considering only sediment-flow interactions, when flow is redistributed in multiple anabranches, like in braided rivers **(Stecca and Hicks, 2022)** and in deltas **(Salter et al., 2020)**. However, in less complex river morphologies, such as those with migrating bars, the emergence of chaos from these interactions remains unproven **(Schielen et al., 1993)**, although it may occur within certain parameter ranges. Despite using simplified eco-morphodynamic models in this analysis, the results demonstrate that adding vegetation may enhance the occurrence of deterministic chaos over a wide range of typical value of stream power (refer to Figure 4.10D).
The presence of chaos could have significant implications for the capability of models to predict river trajectories and for river management. In fact, if rivers exhibit chaotic zones, their management outcomes may not unfold as planned **(Wohl et al., 2015)**.

4.4.1 Limitations of the analysis

There are several limitations regarding this analysis. Firstly, the models used in this thesis are highly simplified, especially the vegetation equations, which have not been parameterized yet. Future research could modify and parameterize the vegetation model to make it more realistic and to observe how chaotic behavior varies depending on it. For example, one could add some important feedbacks such as (i) dependence between biomass B and root depth ζ_{upr}, (ii) dependence of vegetation on the riverbed position, (iii) or cohesive effect of the roots, etc.
Secondly, in the literature, there is a significant debate on the actual importance of chaos in natural systems. Some authors argue that natural systems tend to remain mainly in a zone of stability or periodic oscillations **(Berryman and Millstein, 1989; Upadhyay and Rai, 1997)**. Others, on the contrary, assert that chaos is a fundamental element for evolution and the maintenance of biodiversity **(Jones and Culliney, 1999; Rogers et al., 2022; Munch et al., 2022)**.
Moreover, it is complex to demonstrate the presence of chaos in real river ecosystems. In fact (i) there are not sufficient long time series data to calculate the Maximum Lyapunov Exponent and (ii) in real time series, noise is present due to stochastic elements, such as flood events.
Additionally, it is unknown whether the value of the Maximum Lyapunov Exponent in more complex 2D-models has the same order of magnitude as the one estimated in this analysis. What can be stated with this research is that (i) chaos has been found for a wide range of parameters typical of gravel rivers in the models (ii) the values of the Maximum Lyapunov coefficients in 0D and 1D models are of the same order of magnitude.
It is hoped that these studies on a simplified river ecosystem can serve as a guide for future research in laboratory experiments and real-world analysis, especially considering the current increase in available data. Second, it is hoped that these studies can be useful for conducting analyses on heterogeneous 2D eco-morphodynamic models, such as estimating the order of magnitude of the Maximum Lyapunov Exponent.
Finally, it would be interesting to investigate how stochastic disturbance modifies the

chaotic behavior. In fact, in these analyses, deterministic disturbances are considered, but stochastic events, that have a strong control on vegetation dynamics **(Bertagni et al., 2018)**, could either enhance or mitigate the intrisic chaotic behavior.

Chapter 5

Conclusions and implications

In the river ecosystem, water, sediments, and vegetation interact through nonlinear interactions, which lead to positive and negative feedbacks. These feedbacks, governed by the interplay between disturbance and resistance, generate highly nonlinear and complex processes. In this thesis, eco-morphodynamic models are developed, both non-spatial and spatial, to study a simplified river ecosystem through the lens of the dynamical system theory. The main positive and negative eco-morphodynamic feedbacks are modeled to investigate how they control the complex river dynamics, both statics and dynamics.
In both models, the biomass increases the roughness, reducing flow velocity. Variations in the flow field and the reduction of bottom shear stress modify sediment transport, leading to a greater imbalance between the vegetated and bare areas and thus, inducing erosion. Erosion increases the probability of vegetation uprooting, and when scour reaches root depth, uprooting occurs. The overall feedback loop is negative: higher vegetation biomass causes greater sediment flux imbalance and more erosion, ultimately resulting in less vegetation. However, root growth may inhibit the negative feedback loop, promoting positive feedbacks.
The aim was to address the two research objectives outlined in Section (1.4). Indeed, the aim was to (i) investigate the presence of hysteresis behavior in the simplified ecosystem and how space influences this behavior; (ii) investigate the presence of oscillatory or chaotic behavior, define its properties and driving parameters and quantify the time scale of predictability.
Here, the main key findings of this research are illustrated:

(i) When the negative feedback loop is inhibited, the system tends to reach a steady state. However, the equilibrium is not always unique. The non-spatial model can also show hysteresis, leading to both the vegetated and bare soil depending on the initial condition. In the spatial model, the behavior can become even more complex, exhibiting multi-stability, meaning infinite possible equilibria between the two alternative states are possible.

(ii) When the negative feedback loop prevails, the system oscillates dynamically. These oscillations can be periodic or chaotic and the transition from a stable state to a chaotic one occurs through a period-doubling bifurcation. The solution is confined

within the attractor and the predictability time scale is only a few growth-flood cycles.

5.1 From statics to dynamics

The prevalence or inhibition of the negative feedback loop is what determines the stability or oscillations of the system. The ratio between the hydro-morphodynamic disturbance and vegetation resistance inhibits or increases the negative feedback loop.
In Figure 5.1, different ratios are examined by adjusting the root growth velocity parameter σ_r. A set of simulations are performed with the non-spatial model, where the parameters are those described in Table 3.2 and $offset = 0.8$, $\sigma = 0.12$, and $\beta = 2$. The vegetation before floods B^+ is plotted as a function of the erosion potential E_p. The Figure 5.1 shows how the prevalence of the negative feedback loop and its inhibition varies in the plots (A-E) depending on the value of σ_r. The regions for very low or very high values of Ep have always inhibited negative feedback loop (blue arrows), while in the intermediate regions (red arrows) the negative feedback loop can prevail depending on the value of σ_r. In Figure 5.1(A), it is observed that, when the value of σ_r is high (i.e., ζ_{upr} can be considered constant because it reaches immediately the $offset$) the negative feedback loop prevails, and the system exhibits periodic oscillations and chaos, except for low value of E_p (< 0.2), where the ratio between the resistance and the disturbance ω_{z_B} is low and the inhibition prevails. As the value of σ_r decreases, in order from Figure 5.1(A) to Figure 5.1(E), the negative feedback loop is inhibited, suppressing the oscillations and leading to bi-stability Figure 5.1(E).

5.2 Prediction of evolutionary trajectories

Understanding how positive and negative feedbacks govern the complex dynamics of river ecosystems can have significant implications for predicting evolutionary trajectories and river management. In fact, as observed in this analysis, both in chaotic and multi-stability zones, initial conditions can be crucial and can significantly impact the system's trajectory. An example of how the dependence on initial condition and multi-stability can complicate river management is provided by **Bau' et al.** (**2021**). Their case study is a cross-section representative of the braided reach of the River Maggia. They combine stochastic and deterministic approaches of phreatophytic vegetation dynamics into a analytical framework. At high elevations above the phreatic surface, roots go deep into the soil to reach the water table. Conversely, at lower elevations close to the phreatic surface, roots develop near the soil surface **(Tron et al., 2015; Bau' et al., 2019)**. The main mechanism of death for plants is flow-induced uprooting, modeled with a critical depth leading to plant collapse while the external disturbance is a stochastic river discharge. They also combine the 1D Exner equation for conditions of net bed erosion with a Meyer-Peter and Müller type sediment transport relationship. In 1953, a dam was built on the Maggia River, causing a significant hydrological change that led to vegetation encroachment and gradual channel narrowing. Figure 5.2, displays the case study and analysis by **Bau' et al.** (**2021**) in accordance with the results of this thesis. At point 1 the eco-morphodynamic system is in equilibrium before the construction of a dam. After the construction of the dam, the hydro-morphodynamic

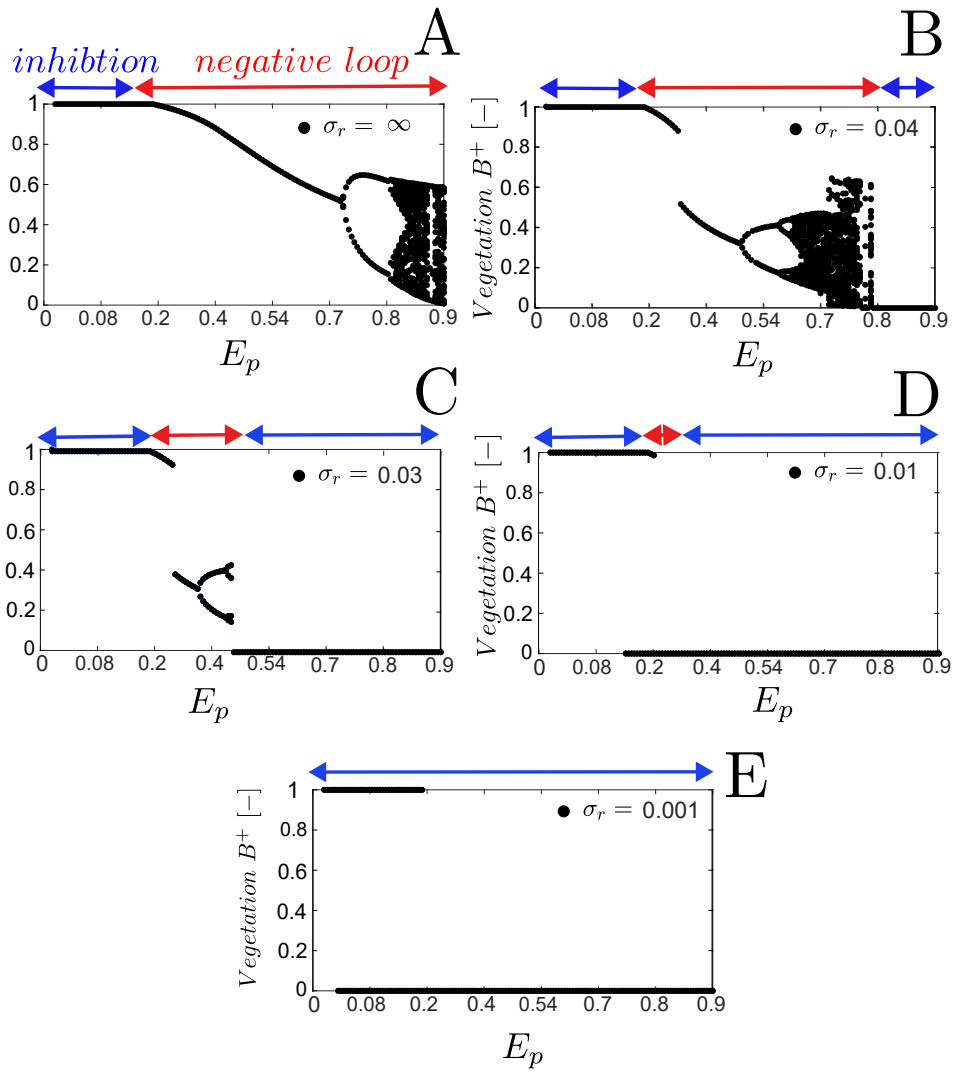

Figure 5.1: Set of simulations performed with the non-spatial model, where the parameters are those described in Table 3.2 and $offset = 0.8$, $\sigma = 0.12$, and $\beta = 2$. The vegetation before floods B^+ is plotted as a function of the erosion potential E_p, varying the value of the root growth velocity σ_r. (A) the value of σ_r is high (i.e., ζ_{upr} can be considered constant because it reaches immediately the $offset$) and the system exhibits periodic oscillations and chaos due to the prevalence of the negative feedback loop (red arrow). (B-C-D-E) as the value of σ_r decreases the negative feedback loop is inhibited (blue arrow), leading to bi-stability.

disturbance (E_p) decreases, and the system shifts to point 2. However, as the disturbance decreases, phreatophytic roots also deepen because the groundwater table lowers due to the dam construction. Due to deeper initial conditions, the system finds its new equilibrium at point 3 between the two alternative states. Assuming removal of the dam and a return to the initial hydro-morphodynamic disturbance E_p, the new equilibrium point 4 differs from the starting point 1 due to deeper root conditions and the presence of multiple possible equilibria.
To return to point 1, it is necessary to increase the hydro-morphodynamic disturbance to point 5, where the system has enough strength to remove the deeper roots, reaching the equilibrium at point 6. Ultimately, reverting to the initial hydro-morphodynamic condition E_p allows the system to return to point 1. However, even upon returning to point 1 with the same mean root value, the spatial distribution is likely to differ from the initial one due to changes in the riverbed and water depth resulting from previous alterations. Thus, it is unlikely that the system returns to the exact starting condition as before the dam construction. Differently from **(Bau' et al., 2021)**, the results of this thesis show not just a possible hysteresis cycle, but all possible multi-equilibria points starting from different initial conditions. Additionally, it provides an explanation as to why the river exhibits multiple stable equilibrium points and where the system is likely to find its new equilibrium.

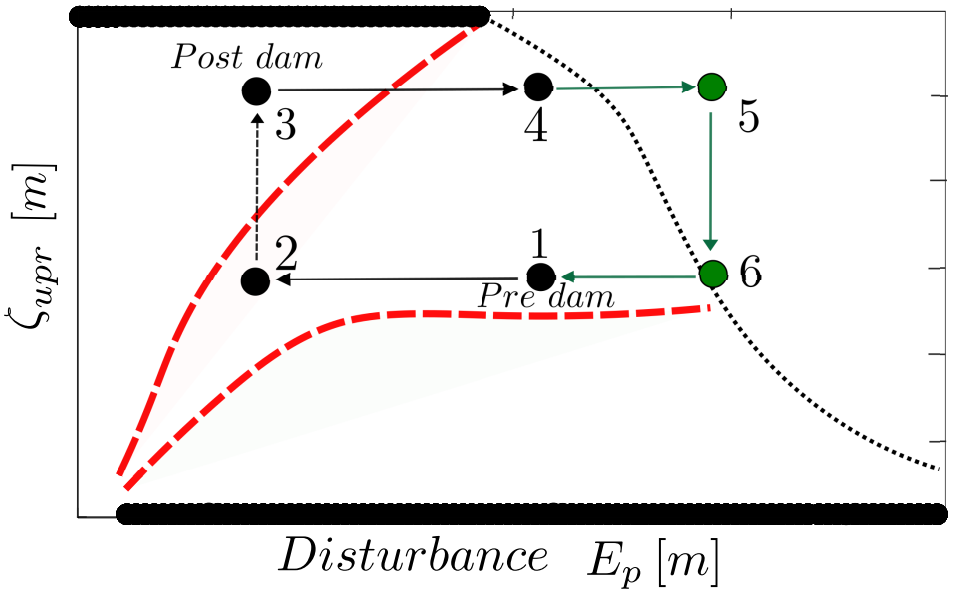

Figure 5.2: Interpretation of **Bau' et al.'s** (**2021**) results according to the multi-stability graph. The construction and successive removal of a dam alter the initial conditions, pushing the system to different equilibria.

The illustrated example shows how the construction and subsequent removal of the dam might not restore the initial conditions of the system, reducing the effectiveness of river management and yielding unexpected results.
Developing models capable of identifying multi-stability behaviors is fundamental to improving the ability to predict river responses and ecosystem restoration.

Moreover, the system can also exhibit non-static behaviors, periodic oscillations, and chaotic dynamics. In this analysis, chaos inherently limits the predictability of the models to a few growth-flood cycles. The strong dependence on initial conditions complicate the ability of models to predict evolutionary trajectories.
However, even though models cannot precisely determine where the outcomes will go, one could identify a zone where they will likely to be (refer to Figure 5.3). In fact, although the chaotic solution cannot be precisely identified, it is confined within the attractor and has a well-defined intrinsic fractal order. Thus, the chaotic solution remains confined within a well-defined zone, even though it is challenging to precisely define its exact position. One could determine this zone by modifying the approach to predictive eco-morphodynamic models, their development, and their interpretation **(Phillips, 2003)**. For instance, most

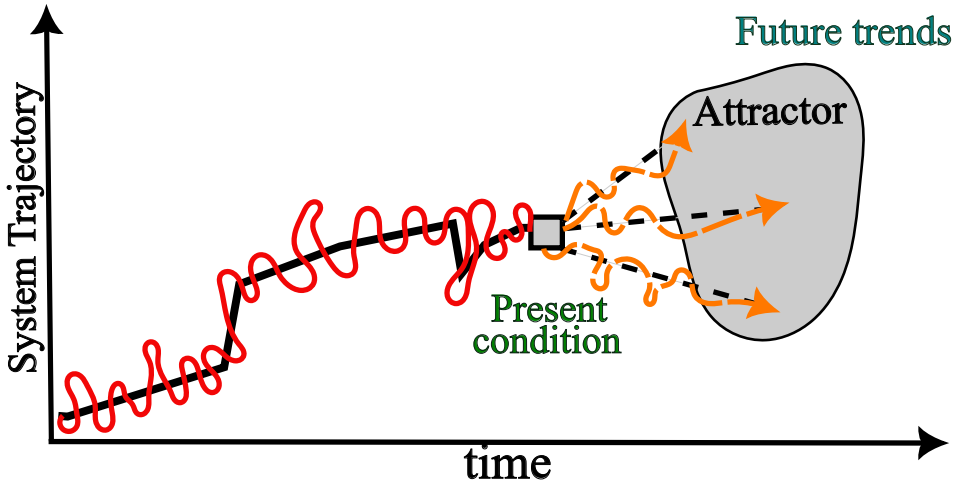

Figure 5.3: Illustration of the system's trajectory over time. If the system enters a chaotic zone, its future trajectory can not be precisely determined. However, a zone known as the attractor can be defined, within which it is likely that the trajectory will go. Adapted from **Dufour and Piégay (2009) and Slingo and Palmer (2011)**.

state-of-the-art predictive approaches rely on statistical methods **(Slingo and Palmer, 2011)**. Another approach is the data-driven machine learning, which has successfully predicted dynamics of some chaotic flows with accurate short-term predictions and long-term statistics **(Doan et al., 2021)**. In other studies, combinations of machine learning with physics-based methods are implemented **(Bar-Sinai et al., 2019)**. Chaos, therefore, imposes limits but also opens up possibilities for developing new tools to predict the trajectories of the river ecosystem and to improve river management.

5.3 General implications

The disturbance-resistance ratio in the models shifts the system equilibrium, induces oscillations, or drives the ecosystem into a chaotic behavior. Climate change and anthropogenic pressure are altering the hydro-morphodynamic disturbance **(Blöschl et al., 2017)**, modifying the ecosystem dynamics. Indeed, variations in the flood regime alter the ratio between disturbance and resistance, thus varying the balance between positive and negative feedbacks and thereby driving the system towards stability or chaos. Understanding whether the impact of climate change on real rivers leads them towards stability or chaos is crucial for determining how to enhance ecosystem resistance and increase resilience.

Since 1950 there is a clear evidence that the fundamental shifts in the state and functioning of the whole Earth ecosystem are driven mainly by human-global economic activities and not by natural variability. Due to this Great Acceleration of human-economic disturbance, humanity has entered into a new geological epoch defined as the Anthropocene **(Steffen et al., 2015)**. The human-global economic activities are modifying the equilibrium of ecosystems, pushing them outside the normal operating parameters. In the language of complex systems, climate change and anthropogenic pressure are modifying the feedbacks balance and creating positive feedback loops that pushes ecosystems towards planetary boundaries **(Rockström et al., 2009)**.

Environmental, social, and economic systems are all complex systems, strongly intercorrelated with each other. A solid understanding of ecosystem dynamics, including whether they exhibit chaotic and unpredictable behaviour, or if they show oscillations or multi-stability, is necessary for preserving the environment and biodiversity. Due to the deep interconnections, the understanding of ecosystem dynamics also play a more hidden but crucial role in reducing social inequality and avoiding economic crises.
With a deep understanding of ecosystem dynamics, one can comprehend their functioning and actively shape the direction for a sustainable future. In fact, a sustainable future is based on healthy ecosystems, social equity, and economical safety. All these objectives can not be achieved without simultaneously satisfying the other two since they are deeply interconnected. In this sense, the human activities and the economic system should not be seen merely as an external disturbance to the Earth's ecosystem. In fact, humanity has permanently altered the Earth's ecosystem, becoming an integral part of this new socio-economic-ecological realty.
By studying this new socio-economic-ecological reality from a dynamical systems perspective, a better understanding can be gained of how to improve its equilibrium, synergy, and resilience. More precisely, it is unthinkable to revert to the lost paradise of natural world **(Dufour and Piégay, 2009)**, but a new socio-economic-ecological equilibrium should be sought.
This awareness must be acquired to fulfill the social duty as scientists: sharing the knowledge with politicians and citizens to collaboratively make the most suitable decisions to build a sustainable future. In fact, since the socio-economic-ecological system is self-regulated, like any complex system, the adaptation or non-adaptation to a new equilibrium also depend on the political and economic choices made as part of the system **(Levin, 1998; Holling, 2001)**.

Appendix A

Link between 0D model with 1D model

A.1 Assumptions of the simplified 1D model

To investigate the behavior of the 1D model without spatial variations, two assumptions are made (refer to Figure A.1):

(i) at the end of each growth period, the vegetation B and root depth ζ_{upr} are uniformly redistributed within the vegetated patch L_v, while preserving their total values.
(ii) at the end of each growth period, the riverbed slope is reset to its initial value S.

Figure A.1 is a sketch of the 1D eco-morphodynamic model (A and B) and its simplified version (A and C). In Figure A.1(A) before the first flood, the slope of the riverbed S is constant, and the vegetation B and the root depth ζ_{upr} are uniformly distributed throughout the entire vegetated patch of length L_v. After the flood, the vegetation and the root depth are partially uprooted, and the slope S changes due to eco-morphodynamic feedbacks. During the next growth period the vegetation and the root depth in the uprooted zone grow differently from the non-uprooted zone (due to different initial conditions). Thus, the new riverbed configuration at the end of the growth period is not uniform inside the vegetated patch. Figure A.1(B) shows the complete 1D model and the configuration described above is used as initial condition for the next flood event. Figure A.1(C) shows the simplified 1D model, where the vegetation B and root depth ζ_{upr} are redistributed uniformly in the vegetated patch (while preserving their total values) and the initial slope is reset to its original constant value S.

A.2 Link between 0D model with 1D model

Despite the further simplifications and removal of the spatial component (refer to Appendix A.1), the 0D model shows a dynamic behavior similar to that of the 1D model, indicating that biogeomorphic feedbacks and the intrinsic disturbance mechanism are the key ingredients generating the chaotic behavior. To investigate a connection between

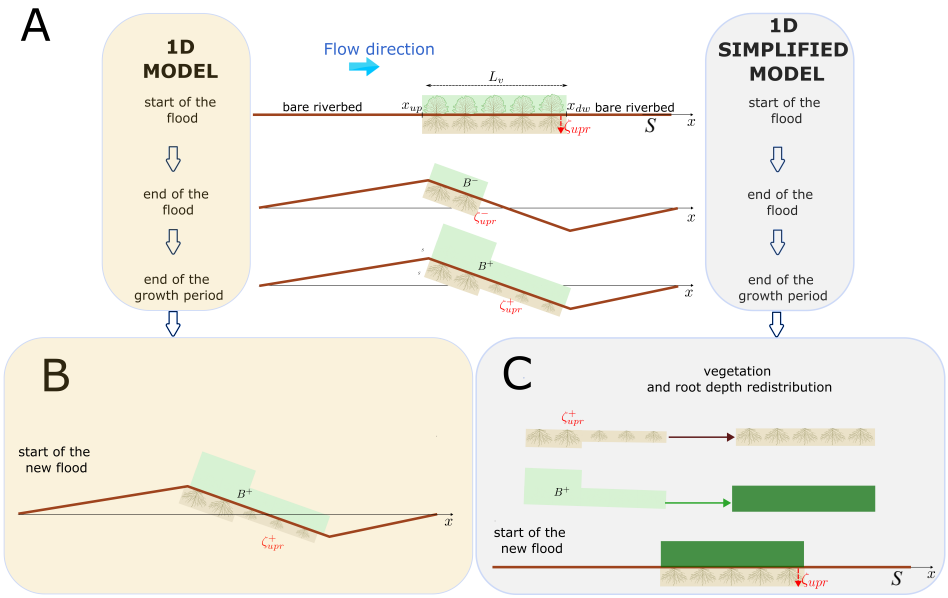

Figure A.1: Sketch of the 1D eco-morphodynamic model (A and B) and its simplified version (A and C).

the models, the behavior of the uprooting function is examined for (i) the 0D model, (ii) the simplified 1D model, and (iii) the complete 1D model, using parameters from Table 3.2.

A.3 0D Model calibration

Figure A.2(A) shows the behavior of the uprooting function of the 0D model, which characterizes the survival of vegetation during floods. Figure A.2(B) shows the behavior of the uprooting function of the 1D simplified model. It exhibits a linear behavior with $\beta = 1$ and $w_m = 0.27$. Figure A.2(C) shows the behavior of the uprooting function of the 1D complete model. Results show strong nonlinear behavior, depending on different values of σ: it can be stated that β frequently exceeded unity, and w_w varied between 0 and 0.4. To establish morphodynamic equivalence between the complete 1D model and the 0D model, the flood duration is calibrated such that $T_F(0D)/T_F(1D) = 0.26$, ensuring that the average erosion in the control volume matches the erosion potential E_p. This calibrated value is used for the analysis of the 0D model.

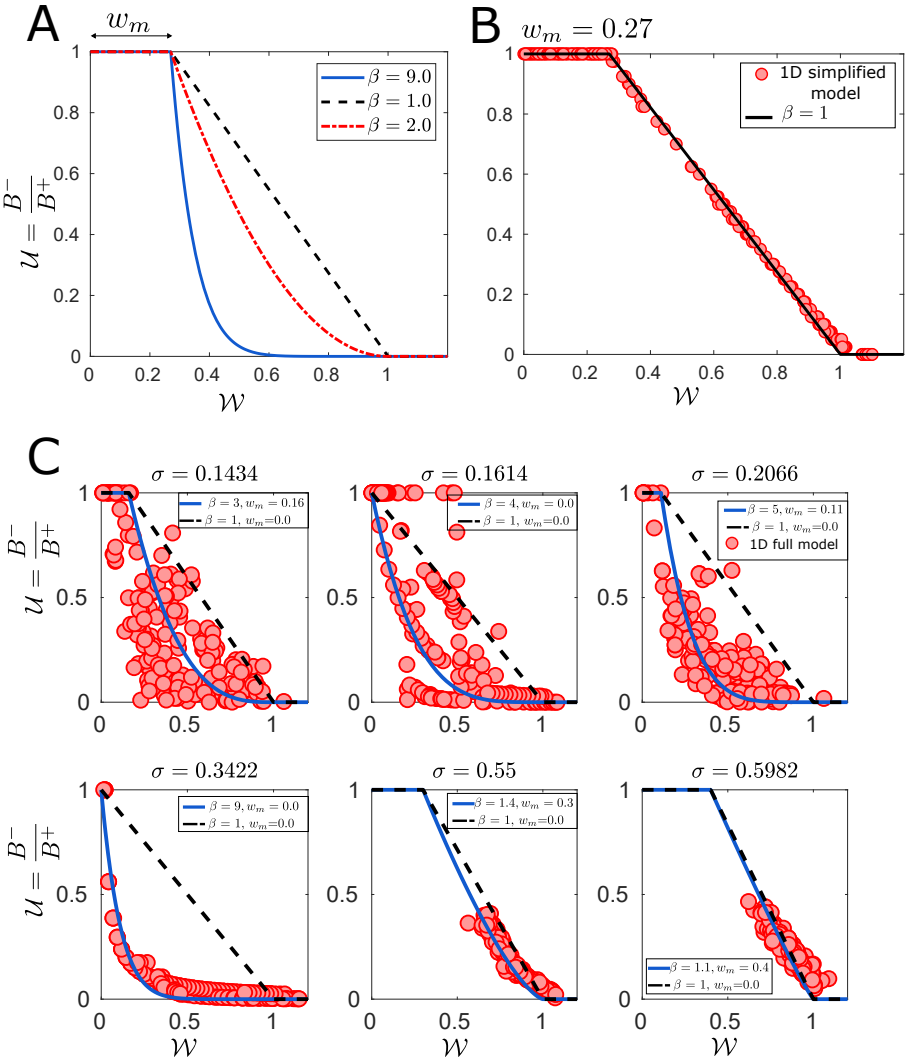

Figure A.2: (A) Behavior of the uprooting function of the 0D model. (B) Behavior of the uprooting function of the 1D simplified model. It exhibits a linear behavior with $\beta = 1$ and $w_m = 0.27$. (C) Behavior of the uprooting function of the 1D complete model. It exhibits a nonlinear behavior, where $\beta > 1$ and w_w varying between 0 and 0.4.

Appendix B

Simplified 1D model and bi-stability

B.1 Numerical simulations

Simulations were performed with the simplified 1D model. All the details of the numerical simulations remain consistent with the analysis described in Section (3.3).

B.2 Results

The results show that for high values of σ_r and *offset*, (Figure B.1A), the system always reaches the steady state in the vegetated state. In contrast, for low values of σ_r and *offset* (Figure B.1B), the system always reaches the steady state in bare soil, except when there is no solid transport (for $q \leq 0.8\ m^2/s,\ \theta < \theta_{cr}$). These results are similar to both the 0D and the complete 1D models.
For intermediate values of σ_r and $offset$, similarly to the 0D model, the system shows bi-stability between $0.8\ m^2/s \leq q \leq 8.0\ m^2/s$ and the steady state depends on the initial condition of the root depth $\zeta_{upr,i}$. To determine the unstable equilibrium, simulations were performed for each value of q with 100 different initial conditions of root depth, $\zeta_{upr,i}$ ranging from [0-1.2].
Differently from the complete 1D model, the simplified 1D model does not exhibit multi-stability, but only bi-stability. This result confirms that spatial interactions are the key element of multi-stability. In fact, spatial interactions are eliminated in the simplified 1D model thanks to the assumptions made above. The results of the simplified 1D model are consistent with the results of the non-spatial model.

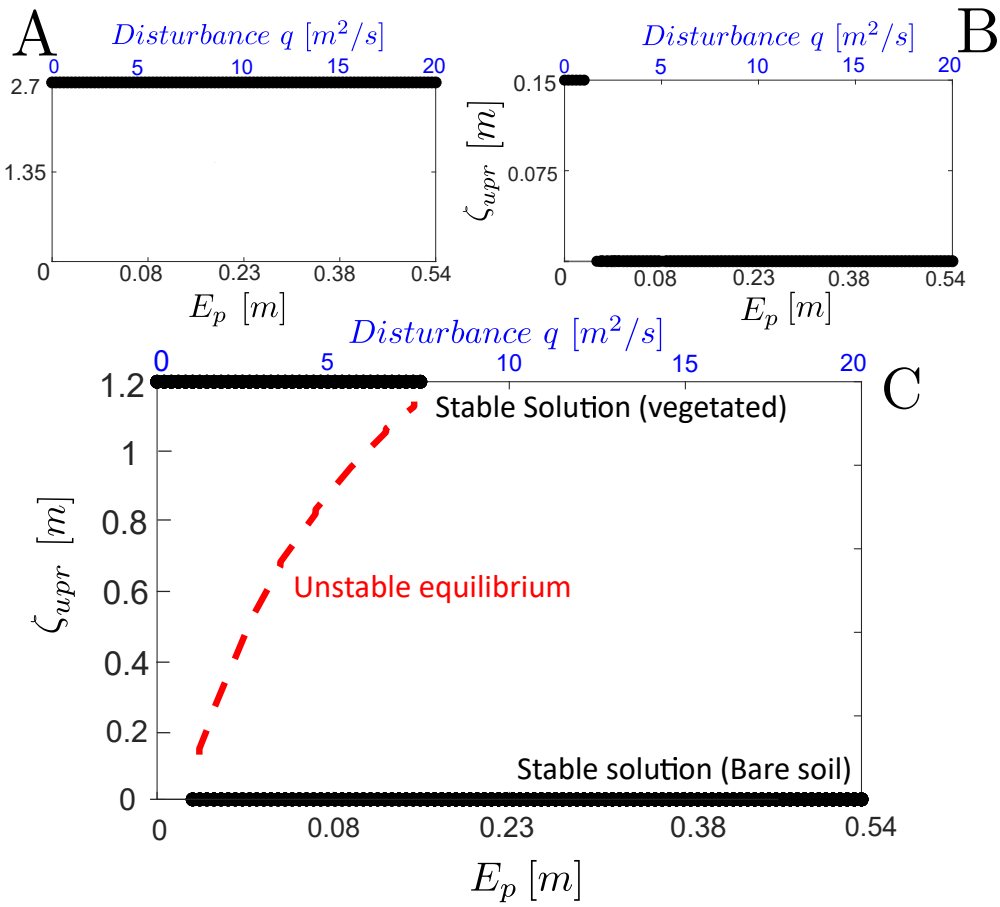

Figure B.1: (A) When roots grow rapidly (high value of σ_r) or deeply into the riverbed (high value of *offset*) the system always reaches the vegetated state. (B) When roots grow slowly (low value of σ_r) or shallowly into the riverbed (low value of *offset*) the system always reaches the bare soil, except when there is no solid transport and thus no uprooting mechanism (for $q \leq 0.8\ m^2/s,\ \theta < \theta_{cr}$). (C) For intermediate values of σ_r and the *offset*, the system exhibits bi-stability for $0.8\ m^2/s \leq q \leq 8.0\ m^2/s$, consistent with the non-spatial model. No multi-stability can be observed. The red line represents the unstable equilibrium of the system.

List of Figures

List of Tables

Bibliography

Balke, T. and C. Nilsson (2019). Increasing synchrony of annual river-flood peaks and growing season in europe. Geophysical Research Letters 46(17-18), 10446–10453.

Bar-Sinai, Y., S. Hoyer, J. Hickey, and M. P. Brenner (2019). Learning data-driven discretizations for partial differential equations. Proceedings of the National Academy of Sciences 116(31), 15344–15349.

Bastiaansen, R., H. A. Dijkstra, and A. S. von der Heydt (2022). Fragmented tipping in a spatially heterogeneous world. Environmental Research Letters 17(4), 045006.

Bau', V., A. G. Borthwick, and P. Perona (2021). Plant roots steer resilience to perturbation of river floodplains. Geophysical Research Letters 48(9), e2021GL092388.

Bau', V., S. Zen, G. Calvani, and P. Perona (2019). Extracting the critical rooting length in plant uprooting by flow from pullout experiments. Water Resources Research 55(12), 10424–10442.

Belletti, B., S. Dufour, and H. Piégay (2014). Regional assessment of the multi-decadal changes in braided riverscapes following large floods (example of 12 reaches in south east of france). Advances in Geosciences 37, 57–71.

Berryman, A. and J. Millstein (1989). Are ecological systems chaotic—and if not, why not? Trends in Ecology & Evolution 4(1), 26–28.

Bertagni, M. B., P. Perona, and C. Camporeale (2018). Parametric transitions between bare and vegetated states in water-driven patterns. Proceedings of the National Academy of Sciences 115(32), 8125–8130.

Bertoldi, W., A. Siviglia, S. Tettamanti, M. Toffolon, D. Vetsch, and S. Francalanci (2014). Modeling vegetation controls on fluvial morphological trajectories. Geophysical Research Letters 41(20), 7167–7175.

Blöschl, G., J. Hall, J. Parajka, R. A. Perdigão, B. Merz, B. Arheimer, G. T. Aronica, A. Bilibashi, O. Bonacci, M. Borga, et al. (2017). Changing climate shifts timing of european floods. Science 357(6351), 588–590.

Bouma, T., L. Van Duren, S. Temmerman, T. Claverie, A. Blanco-Garcia, T. Ysebaert, and P. Herman (2007). Spatial flow and sedimentation patterns within patches of epibenthic structures: Combining field, flume and modelling experiments. Continental Shelf Research 27(8), 1020–1045.

Bywater-Reyes, S., A. C. Wilcox, J. C. Stella, and A. F. Lightbody (2015). Flow and scour constraints on uprooting of pioneer woody seedlings. Water Resources Research 51(11), 9190–9206.

Camporeale, C., E. Perucca, L. Ridolfi, and A. Gurnell (2013). Modeling the interactions between river morphodynamics and riparian vegetation. Reviews of Geophysics 51(3), 379–414.

Camporeale, C. and L. Ridolfi (2006). Riparian vegetation distribution induced by river flow variability: A stochastic approach. Water resources research 42(10).

Caponi, F., A. Koch, W. Bertoldi, D. F. Vetsch, and A. Siviglia (2019). When does vegetation establish on gravel bars? observations and modeling in the alpine rhine river. Frontiers in Environmental Science 7, 124.

Caponi, F. and A. Siviglia (2018). Numerical modeling of plant root controls on gravel bed river morphodynamics. Geophysical Research Letters 45(17), 9013–9023.

Caponi, F., D. F. Vetsch, and A. Siviglia (2020). A model study of the combined effect of above and below ground plant traits on the ecomorphodynamics of gravel bars. Scientific reports 10(1), 1–14.

Cavagna, A., A. Cimarelli, I. Giardina, G. Parisi, R. Santagati, F. Stefanini, and M. Viale (2010). Scale-free correlations in starling flocks. Proceedings of the National Academy of Sciences 107(26), 11865–11870.

Corenblit, D., J. Steiger, E. González, A. M. Gurnell, G. Charrier, J. Darrozes, J. Dousseau, F. Julien, L. Lambs, S. Larrue, et al. (2014). The biogeomorphological life cycle of poplars during the fluvial biogeomorphological succession: a special focus on populus nigra l. Earth Surface Processes and Landforms 39(4), 546–563.

Corenblit, D., J. Steiger, A. M. Gurnell, and R. J. Naiman (2009). Plants intertwine fluvial landform dynamics with ecological succession and natural selection: a niche construction perspective for riparian systems. Global Ecology and Biogeography 18(4), 507–520.

Corenblit, D., E. Tabacchi, J. Steiger, and A. M. Gurnell (2007). Reciprocal interactions and adjustments between fluvial landforms and vegetation dynamics in river corridors: a review of complementary approaches. Earth-Science Reviews 84(1-2), 56–86.

Corning, P. A. (2012). The re-emergence of emergence, and the causal role of synergy in emergent evolution. Synthese 185(2), 295–317.

Coulthard, T., D. Hicks, and M. J. Van De Wiel (2007). Cellular modelling of river catchments and reaches: advantages, limitations and prospects. Geomorphology 90(3-4), 192–207.

Crosato, A. and M. S. Saleh (2011). Numerical study on the effects of floodplain vegetation on river planform style. Earth Surface Processes and Landforms 36(6), 711–720.

Crouzy, B., K. Edmaier, N. Pasquale, and P. Perona (2013). Impact of floods on the statistical distribution of riverbed vegetation. Geomorphology 202, 51–58.

Crutchfield, J., J. Farmer, N. Packard, and R. Shaw (1986). Chaos scientific american 225 (6): 46-57. Crutchfeld646225Scientific American.

DeAngelis, D. L., W. M. Post, and C. C. Travis (2012). Positive feedback in natural systems, Volume 15. Springer Science & Business Media.

Dent, C. L., G. S. Cumming, and S. R. Carpenter (2002). Multiple states in river and lake ecosystems. Philosophical Transactions of the Royal Society of London. Series B: Biological Sciences 357(1421), 635–645.

Diehl, R. M., A. C. Wilcox, J. C. Stella, L. Kui, L. S. Sklar, and A. Lightbody (2017). Fluvial sediment supply and pioneer woody seedlings as a control on bar-surface topography. Earth Surface Processes and Landforms 42(5), 724–734.

Doan, N. A. K., W. Polifke, and L. Magri (2021). Short-and long-term predictions of chaotic flows and extreme events: a physics-constrained reservoir computing approach. Proceedings of the Royal Society A 477(2253), 20210135.

Dufour, S. and H. Piégay (2009). From the myth of a lost paradise to targeted river restoration: forget natural references and focus on human benefits. River research and applications 25(5), 568–581.

Edmaier, K., P. Burlando, and P. Perona (2011). Mechanisms of vegetation uprooting by flow in alluvial non-cohesive sediment. Hydrology and Earth System Sciences 15(5), 1615–1627.

Edmaier, K., B. Crouzy, and P. Perona (2015). Experimental characterization of vegetation uprooting by flow. Journal of Geophysical Research: Biogeosciences 120(9), 1812–1824.

Fan, Y., G. Miguez-Macho, E. G. Jobbágy, R. B. Jackson, and C. Otero-Casal (2017). Hydrologic regulation of plant rooting depth. Proceedings of the National Academy of Sciences 114(40), 10572–10577.

Franchi, M. and L. Ricci (2014). Statistical properties of the maximum lyapunov exponent calculated via the divergence rate method. Physical Review E 90(6), 062920.

Goldberger, A. L. (1991). Is the normal heartbeat chaotic or homeostatic? Physiology 6(2), 87–91.

Goldstein, E. B. and L. J. Moore (2016). Stability and bistability in a one-dimensional model of coastal foredune height. Journal of Geophysical Research: Earth Surface 121(5), 964–977.

Gregory, P. (2007, 11). Plant roots: Growth, activity and interaction with soils. Plant Roots: Growth, Activity and Interaction with Soils, 1–318.

Grimaudo, R., P. Lazzari, C. Solidoro, and D. Valenti (2022). Effects of solar irradiance noise on a complex marine trophic web. Scientific Reports 12(1), 12163.

Gritli, H., S. Belghith, and N. Khraeif (2012). Intermittency and interior crisis as route to chaos in dynamic walking of two biped robots. International Journal of Bifurcation and Chaos 22(03), 1250056.

Gurnell, A. (2014). Plants as river system engineers. Earth Surface Processes and Landforms 39(1), 4–25.

Hegger, R., H. Kantz, and T. Schreiber (1999). Practical implementation of nonlinear time series methods: The tisean package. Chaos: An Interdisciplinary Journal of Nonlinear Science 9(2).

Holling, C. S. (1973). Resilience and stability of ecological systems. Annual review of ecology and systematics 4(1), 1–23.

Holling, C. S. (2001). Understanding the complexity of economic, ecological, and social systems. Ecosystems 4, 390–405.

Holloway, J. V., M. C. Rillig, and A. M. Gurnell (2017). Underground riparian wood: Buried stem and coarse root structures of black poplar (populus nigra l.). Geomorphology 279, 188–198.

Holmgren, M. and M. Scheffer (2001). El niño as a window of opportunity for the restoration of degraded arid ecosystems. Ecosystems 4, 151–159.

Isaeva, V. (2012). Self-organization in biological systems. Biology Bulletin 39, 110–118.

Jones, C. G., J. H. Lawton, and M. Shachak (1994). Organisms as ecosystem engineers. Oikos, 373–386.

Jones, D. and J. Culliney (1999). The fractal self and the organization of nature: The daoist sage and chaos theory. Zygon® 34(4), 643–654.

Kantz, H. (1994). A robust method to estimate the maximal lyapunov exponent of a time series. Physics Letters A 185(1), 77–87.

Kantz, H. and T. Schreiber (2003). Nonlinear Time Series Analysis (2 ed.). Cambridge University Press.

Kantz, H. and T. Schreiber (2004). Nonlinear time series analysis, Volume 7. Cambridge university press.

Kim, H. S., I. Kimura, and Y. Shimizu (2015). Bed morphological changes around a finite patch of vegetation. Earth Surface Processes and Landforms 40(3), 375–388. ESP-13-0354.R3.

Lake, P. S. (2013). Resistance, resilience and restoration. Ecological management & restoration 14(1), 20–24.

Le Bouteiller, C. and J. Venditti (2015). Sediment transport and shear stress partitioning in a vegetated flow. Water Resources Research 51(4), 2901–2922.

Le Bouteiller, C. and J. G. Venditti (2014). Vegetation-driven morphodynamic adjustments of a sand bed. Geophysical Research Letters 41(11), 3876–3883.

Levin, S. A. (1998). Ecosystems and the biosphere as complex adaptive systems. Ecosystems 1, 431–436.

Li, S. and R. Millar (2011). A two-dimensional morphodynamic model of gravel-bed river with floodplain vegetation. Earth Surface Processes and Landforms 36(2), 190–202.

Limburg, K. E., R. V. O'Neill, R. Costanza, and S. Farber (2002). Complex systems and valuation. Ecological economics 41(3), 409–420.

Lloyd, D., M. A. Aon, S. Cortassa, et al. (2001). Why homeodynamics, not homeostasis? The Scientific World Journal 1, 133–145.

Lorenz, E. (1972). Predictability: Does the flap of a butterfly's wing in brazil set off a tornado in texas?

Lorenz, E. N. (1963). Deterministic nonperiodic flow. Journal of atmospheric sciences 20(2), 130–141.

Mahoney, J. M. and S. B. Rood (1998, 12). Streamflow requirements for cottonwood seedling recruitment—an integrative model. Wetlands 18, 634–645.

Mandelbrot, B. B. (1982). The fractal geometry of nature, Volume 1. WH freeman New York.

Marani, M., A. D'Alpaos, S. Lanzoni, L. Carniello, and A. Rinaldo (2010). The importance of being coupled: Stable states and catastrophic shifts in tidal biomorphodynamics. Journal of Geophysical Research: Earth Surface 115(F4).

May, R. M. (1974). Biological populations with nonoverlapping generations: stable points, stable cycles, and chaos. Science 186(4164), 645–647.

May, R. M. (1977). Thresholds and breakpoints in ecosystems with a multiplicity of stable states. Nature 269(5628), 471–477.

Meron, E. (2015). Nonlinear physics of ecosystems. CRC Press.

Meron, E., Y. Mau, and Y. R. Zelnik (2019). Multistability in ecosystems: Concerns and opportunities for ecosystem function in variable environments. Mathematics of Planet Earth: Protecting Our Planet, Learning from the Past, Safeguarding for the Future, 177–202.

Meyer-Peter, E., and R. Müller (1948). Formulas for bed-load transport. In 2nd Meeting, Int. Assoc. of Hydraul. Eng. and Res. Stockholm.

Morgan Ernest, S. and J. H. Brown (2001). Homeostasis and compensation: the role of species and resources in ecosystem stability. Ecology 82(8), 2118–2132.

Munch, S. B., T. L. Rogers, B. J. Johnson, U. Bhat, and C.-H. Tsai (2022). Rethinking the prevalence and relevance of chaos in ecology. Annual Review of Ecology, Evolution, and Systematics 53, 227–249.

Murray, A. B. and C. Paola (2003). Modelling the effect of vegetation on channel pattern in bedload rivers. Earth Surface Processes and Landforms: The Journal of the British Geomorphological Research Group 28(2), 131–143.

Nepf, H. M. (2012). Flow and transport in regions with aquatic vegetation. Annual review of fluid mechanics 44, 123–142.

Newman, M. E. (2011). Complex systems: A survey. arXiv preprint arXiv:1112.1440.

Odum, E. P. (1959). Fundamentals of ecology. Technical report.

Palmer, M. and A. Ruhi (2019). Linkages between flow regime, biota, and ecosystem processes: Implications for river restoration. Science 365(6459), eaaw2087.

Paola, C. and M. Leeder (2011). Simplicity versus complexity. Nature 469(7328), 38–39.

Parker, G. (2004). The quasi-steady approximation, chap. 13. 1D Sediment Transport Morphodynamics with Applications to Rivers and Turbidity Currents.. `http://hydrolab.illinois.edu/people/parkerg/powerpoint_lectures.htm`.

Pasquale, N., P. Perona, R. Francis, and P. Burlando (2012). Effects of streamflow variability on the vertical root density distribution of willow cutting experiments. Ecological Engineering 40, 167–172.

Pasquale, N., P. Perona, R. Francis, and P. Burlando (2014). Above-ground and below-ground salix dynamics in response to river processes. Hydrological Processes 28(20), 5189–5203.

Perona, P. and B. Crouzy (2018). Resilience of riverbed vegetation to uprooting by flow. Proceedings of the Royal Society A: Mathematical, Physical and Engineering Sciences 474(2211), 20170547.

Perona, P., P. Molnar, M. Savina, and P. Burlando (2009). An observation-based stochastic model for sediment and vegetation dynamics in the floodplain of an alpine braided river. Water Resources Research 45(9).

Phillips, J. D. (2003). Sources of nonlinearity and complexity in geomorphic systems. Progress in physical geography 27(1), 1–23.

Politti, E., W. Bertoldi, A. Gurnell, and A. Henshaw (2018). Feedbacks between the riparian salicaceae and hydrogeomorphic processes: A quantitative review. Earth-Science Reviews 176, 147–165.

Reluga, T. C. (2004). Analysis of periodic growth–disturbance models. Theoretical population biology 66(2), 151–161.

Rietkerk, M., R. Bastiaansen, S. Banerjee, J. van de Koppel, M. Baudena, and A. Doelman (2021). Evasion of tipping in complex systems through spatial pattern formation. Science 374(6564), eabj0359.

Rietkerk, M., S. C. Dekker, P. C. De Ruiter, and J. van de Koppel (2004). Self-organized patchiness and catastrophic shifts in ecosystems. Science 305(5692), 1926–1929.

Rinaldi, S. and M. Scheffer (2000). Geometric analysis of ecological models with slow and fast processes. Ecosystems 3, 507–521.

Rinaldo, A. (2005). River basins: Water and complex adaptive systems. Water and the Environment 12, 157.

Rockström, J., W. Steffen, K. Noone, Å. Persson, F. S. Chapin III, E. Lambin, T. M. Lenton, M. Scheffer, C. Folke, H. J. Schellnhuber, et al. (2009). Planetary boundaries: exploring the safe operating space for humanity. Ecology and society 14(2).

Rogers, T. L., B. J. Johnson, and S. B. Munch (2022). Chaos is not rare in natural ecosystems. Nature ecology & evolution 6(8), 1105–1111.

Rohde, M. M., J. C. Stella, D. A. Roberts, and M. B. Singer (2021). Groundwater dependence of riparian woodlands and the disrupting effect of anthropogenically altered streamflow. Proceedings of the National Academy of Sciences 118(25), e2026453118.

Rosier, S. H., R. Reese, J. F. Donges, J. De Rydt, G. H. Gudmundsson, and R. Winkelmann (2020). The tipping points and early-warning indicators for pine island glacier, west antarctica. The Cryosphere Discussions 2020, 1–23.

Ruoff, P. and N. Nishiyama (2020). Frequency switching between oscillatory homeostats and the regulation of p53. Plos one 15(5), e0227786.

Rykiel Jr, E. J. (1985). Towards a definition of ecological disturbance. Australian Journal of Ecology 10(3), 361–365.

Salter, G., V. R. Voller, and C. Paola (2020). Chaos in a simple model of a delta network. Proceedings of the National Academy of Sciences 117(44), 27179–27187.

Scheffer, M., S. Carpenter, J. A. Foley, C. Folke, and B. Walker (2001). Catastrophic shifts in ecosystems. Nature 413(6856), 591–596.

Schielen, R., A. Doelman, and H. De Swart (1993). On the nonlinear dynamics of free bars in straight channels. Journal of Fluid Mechanics 252, 325–356.

Schwarz, C., O. Gourgue, J. Van Belzen, Z. Zhu, T. J. Bouma, J. Van De Koppel, G. Ruessink, N. Claude, and S. Temmerman (2018). Self-organization of a biogeomorphic landscape controlled by plant life-history traits. Nature Geoscience 11(9), 672–677.

Seminara, G. (2010). Fluvial sedimentary patterns. Annual Review of Fluid Mechanics 42, 43–66.

Seminara, G. and M. Tubino (2001). Sand bars in tidal channels. part 1. free bars. Journal of Fluid Mechanics 440, 49–74.

Shinbrot, T., C. Grebogi, J. Wisdom, and J. A. Yorke (1992). Chaos in a double pendulum. American Journal of Physics 60(6), 491–499.

Siteur, K., J. Mao, K. G. Nierop, M. Rietkerk, S. C. Dekker, and M. B. Eppinga (2016). Soil water repellency: a potential driver of vegetation dynamics in coastal dunes. Ecosystems 19, 1210–1224.

Siteur, K., E. Siero, M. B. Eppinga, J. D. Rademacher, A. Doelman, and M. Rietkerk (2014). Beyond turing: The response of patterned ecosystems to environmental change. Ecological Complexity 20, 81–96.

Slingo, J. and T. Palmer (2011). Uncertainty in weather and climate prediction. Philosophical Transactions of the Royal Society A: Mathematical, Physical and Engineering Sciences 369(1956), 4751–4767.

Smith, L. C. (2020). Rivers of power: how a natural force raised kingdoms, destroyed civilizations, and shapes our world. Penguin UK.

Solari, L., M. Van Oorschot, B. Belletti, D. Hendriks, M. Rinaldi, and A. Vargas-Luna (2016). Advances on modelling riparian vegetation—hydromorphology interactions. River Research and Applications 32(2), 164–178.

Stecca, G. and D. M. Hicks (2022). Numerical simulations of confined braided river morphodynamics: Display of deterministic chaos and characterization through turbulence theory. Journal of Geophysical Research: Earth Surface 127(3), e2021JF006409.

Stecca, G., R. J. Measures, and D. M. Hicks (2017). A framework for the analysis of non-cohesive bank erosion algorithms in morphodynamics modelling. Water Resources Research.

Steffen, W., W. Broadgate, L. Deutsch, O. Gaffney, and C. Ludwig (2015). The trajectory of the anthropocene: the great acceleration. The Anthropocene Review 2(1), 81–98.

Stone, M. A. (1989). Chaos, prediction and laplacean determinism. American philosophical quarterly 26(2), 123–131.

Strogatz, S. H. (2018). Nonlinear dynamics and chaos: With applications to physics, biology, chemistry, and engineering. CRC Press.

Surian, N., M. Barban, L. Ziliani, G. Monegato, W. Bertoldi, and F. Comiti (2015). Vegetation turnover in a braided river: frequency and effectiveness of floods of different magnitude. Earth Surface Processes and Landforms 40(4), 542–558.

Sussman, G. J. and J. Wisdom (1992). Chaotic evolution of the solar system. Science 257(5066), 56–62.

Tal, M. and C. Paola (2010). Effects of vegetation on channel morphodynamics: results and insights from laboratory experiments. Earth Surface Processes and Landforms 35(9), 1014–1028.

Toro, E. F. (2001). Shock-capturing methods for free-surface shallow flows. Wiley-Blackwell.

Tron, S., F. Laio, and L. Ridolfi (2014). Effect of water table fluctuations on phreatophytic root distribution. Journal of Theoretical Biology 360, 102–108.

Tron, S., P. Perona, L. Gorla, M. Schwarz, F. Laio, and L. Ridolfi (2015). The signature of randomness in riparian plant root distributions. Geophysical Research Letters 42(17), 7098–7106.

Turing, A. M. (1990). The chemical basis of morphogenesis. Bulletin of mathematical biology 52, 153–197.

Upadhyay, R. K. and V. Rai (1997). Why chaos is rarely observed in natural populations. Chaos, Solitons & Fractals 8(12), 1933–1939.

Van de Vijsel, R. C., J. van Belzen, T. J. Bouma, D. van der Wal, B. W. Borsje, S. Temmerman, L. Cornacchia, O. Gourgue, and J. van de Koppel (2023). Vegetation controls on channel network complexity in coastal wetlands. Nature communications 14(1), 7158.

Van der Kaaden, A.-S., D. Van Oevelen, M. Rietkerk, K. Soetaert, and J. Van de Koppel (2020). Spatial self-organization as a new perspective on cold-water coral mound development. Frontiers in Marine Science 7, 631.

Van Kampen, N. (1991). Determinism and predictability. Synthese 89, 273–281.

Van Oorschot, M. et al. (2017). Riparian vegetation interacting with river morphology: modelling long-term ecosystem responses to invasive species, climate change, dams and river restoration. Ph. D. thesis, University Utrecht.

Vargas-Luna, A., A. Crosato, and W. S. Uijttewaal (2015). Effects of vegetation on flow and sediment transport: comparative analyses and validation of predicting models. Earth Surface Processes and Landforms 40(2), 157–176.

Västilä, K. and J. Järvelä (2014). Modeling the flow resistance of woody vegetation using physically based properties of the foliage and stem. Water Resources Research 50(1), 229–245.

Wang, C., Q. Wang, D. Meire, W. Ma, C. Wu, Z. Meng, J. Van de Koppel, P. Troch, R. Verhoeven, T. De Mulder, et al. (2016). Biogeomorphic feedback between plant growth and flooding causes alternative stable states in an experimental floodplain. Advances in water resources 93, 223–235.

Wohl, E., S. N. Lane, and A. C. Wilcox (2015). The science and practice of river restoration. Water Resources Research 51(8), 5974–5997.

Yager, E. and M. Schmeeckle (2013). The influence of vegetation on turbulence and bed load transport. Journal of Geophysical Research: Earth Surface 118(3), 1585–1601.

Zhang, H., X. Cong, T. Huang, S. Ma, and G. Pan (2018). Neimark-sacker-turing instability and pattern formation in a spatiotemporal discrete predator-prey system with allee effect. Discrete Dynamics in Nature and Society 2018.

Zong, L. and H. Nepf (2010). Flow and deposition in and around a finite patch of vegetation. Geomorphology 116(3-4), 363–372.

Zong, L. and H. Nepf (2012). Vortex development behind a finite porous obstruction in a channel. Journal of Fluid Mechanics 691, 368–391.